SCUOLA SUPERIORE MERIDIONALE
*University of Naples Federico II*

DOCTORAL THESIS
*in Modeling and Engineering Risk and Complexity*

# Controlling the Collective Dynamics of Large-Scale Multi-Agent Systems

*Author:*
Gian Carlo Maffettone

*Supervisors:*
Prof. Mario di Bernardo
Prof. Maurizio Porfiri

*Submitted in fulfilment of the requirements for*
*the degree of Doctor of Philosophy in*
*Modeling and Engineering Risk and Complexity.*
*Coordinator: Prof. Mario di Bernardo.*

*December 12, 2024*

*Alle nonne, Beba e Fabrizia*

# Abstract

The understanding, modeling and control of large-scale multi-agent systems is crucial in uncountable open problems spanning from mathematics to physics and engineering. A deeper comprehension of these fascinating dynamical entities can enable the development of important steps towards new, more convenient solutions for many real world applications, from etho/swarm robotics to synthetic biology, and traffic/crowds control. In this Theses, we focus on how the multi-scale nature of large aggregates of interacting dynamical units plays an essential role when dealing with cutting-edges control problems. In particular, we face the problem of how to analytically ensure the fulfillment of macroscopic objectives regarding the emerging properties of a complex system, by only using microscopic actuation. Within the general context of density control, we both consider homogeneous and heterogeneous groups. In the former case, we apply control actions to all the individuals in the collective, in the latter, control is constrained to be exertable via a subset of special leader agents. Robustness of the proposed solution is assessed theoretically, numerically and experimentally. In particular, the experimental validation is performed through a mixed reality platform we developed for the agile testing of swarm robotics solutions.

# Acknowledgements

I would like to extend my deepest gratitude to my supervisors, Professor Mario di Bernardo and Professor Maurizio Porfiri. Their unique blend of similarities and differences fostered the ideal environment for my growth, both as a scientist and as a person. From instilling an exceptional work ethic and mathematical rigor, to providing invaluable guidance on becoming a well-rounded scholar, I owe much to them.

Over these years, I have had the privilege of working across two labs: the Sincro Group in Naples and the Dynamical Systems Laboratory (DSL) in New York. On both sides of the Atlantic, I found remarkable colleagues and friends with whom I share fantastic memories. In Naples, special thanks go to Dr. Andrea Giusti, my colleague since the start of our undergraduate journey, Dr. Davide Fiore, co-advisor of my master's thesis and later a good friend, Dr. Davide Salzano, a companion through countless breaks, and Professor Fabio della Rossa, my roommate just beyond the “attaccapanni".

In New York, despite the distance from home, I was lucky enough to find people who never let me feel nostalgic. Rayan Succar, Salvador Ramallo Ros, Tian Gan, Nicco Ulbricht, Fabiana Sofia Ricci, Lorenzo Liguori, Anna Sawulska and Roni Barak Ventura have become dear friends. Among those I met at the DSL, Professor Alain Boldini was both a friend and mentor, whose passion for science showed me why it is important and fun to do research.

In my first year as a Ph.D. student, even amidst the challenges of COVID-19, I had the chance to engage with the Scuola Superiore Meridionale student community. Francesco Flora, Domenico Giaquinto, Veronica Centorrino, Gianluca Fabiani, Ayman Bin Kamruddin, Dario Pisanti, and Marcello Miranda made that year intellectually stimulating and incredibly enjoyable.

Finally, I wish to thank my family for their unconditional love and support throughout this journey. And to Francesca, my heartfelt thanks for her love and grounding pragmatism, which have always kept me centered.

# Contents

# 1 Introduction

## 1.1 Controlling the collective dynamics of large-scale multi-agent systems

Many fascinating phenomena observed in nature arise from the interaction of highly interconnected, simple dynamical units. Specifically, through local information exchange, remarkable group behaviors can emerge. These behaviors, intriguingly, cannot be explained by merely aggregating those of the individuals in the group; rather, they are generated by the inherent feedback mechanisms implemented through local interactions [1]. Examples include collective animal behaviors such as fish schooling [2, 3, 4], bird flocking [5, 6], and the division of labor in ants [7, 8, 9]. Other examples involve engineered systems designed to produce useful emergent properties, such as social networks [10, 11], the Internet of Things [12], and power grids [13]. Collectives exhibiting these behaviors are typically referred to as *complex* and/or *multi-agent* systems [14].

Understanding and controlling these systems is key to solving numerous challenges from various perspectives. First, it is essential to manage the behavior of complex systems that directly impact daily life. For example, smoothing traffic waves can promote energy efficiency and reduce pollution [15]. In human crowds, it is vital to prevent crowd crushes (sometimes referred to as stampedes) [16]. Equally important is ensuring that desired collective behaviors emerge in groups of agents collaborating to achieve a task. Examples of such settings include biological systems (e.g., dogs shepherding sheep) [17], social systems (e.g., influencers guiding public opinion) [18, 19], and swarm robotics (e.g., search and rescue missions) [20].

This Thesis examines large-scale multi-agent systems and the control of their emergent properties. Specifically, we tackle the problem of creating a mathematical, computational, and experimental framework for agile analysis and control design. The

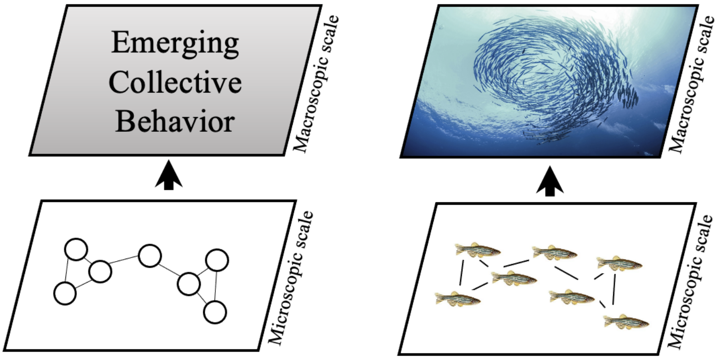

Figure 1.1: Conceptualization of a large-scale multi-agent system, emphasizing their multi-scale nature.

following sections offer a brief overview of large-scale complex systems, emphasizing their multi-scale nature, a critical factor when controlling these systems.

### 1.1.1 Large-Scale Complex Systems

Complex multi-agent systems consist of interacting dynamical units that, through feedback mechanisms from local interactions, exhibit emergent properties [1]. These systems can be described at different scales, making them *multi-scale* systems[1]. This Thesis focuses on two key levels:

- the *microscopic* scale, where individual behaviors are described and modeled;
- the *macroscopic* scale, where collective behavior emerges, often in ways not easily traced to individual actions.

Consider a school of fish. At the microscopic scale, we study how individual fish influence each other's movement, while at the macroscopic scale, the focus shifts to the behavior of the school as a whole. This transition often involves moving from the study of individual motions to the spatio-temporal dynamics of the group's density. See Fig. 1.1 for a schematic representation.

---

[1] In dynamical systems theory, multi-scale typically refers to systems evolving on different time/spatial scales (fast and slow). Here, we use the term to highlight the distinct levels of description in complex systems (microscopic and macroscopic)

At the microscopic scale, mathematical formulations typically use ordinary or stochastic differential equations (ODEs/SDEs), well suited for describing dynamical systems on potentially time-varying network topologies [1]. Conversely, the macroscopic scale is often best described by partial differential equations (PDEs), which efficiently capture emergent properties that vary across at least two dimensions, such as time and space, such as time and space. In some contexts, an intermediate *mesoscopic* scale is defined, but we do not include this additional level in our work[2].

When the number of interacting nodes or agents becomes very large, theoretically infinite, we refer to the system as a *large-scale* complex multi-agent system. While a precise definition is absent in the literature, we can say that when emergent properties no longer depend on group size, we are in a large-scale scenario [22]. In such cases, microscopic descriptions based on ODEs/SDEs are impractical due to the curse of dimensionality in agent-based models [23, 24]. Thus, macroscopic descriptions offer a more efficient and compact approach.

### 1.1.2 Control of complex systems across scales

This thesis focuses on the control of large-scale complex multi-agent systems, including robot swarms and heterogeneous populations of natural and artificial agents, such as animals and robots. Traditionally, control means taking measurements and applying actuation to a dynamical system to achieve a desired behavior (see Fig. 1.2a for a classical control loop).

In classical scenarios, the system to control, measurements, and actuation can be modeled at the same descriptive scale. When the process or plant to control is a complex multi-agent system, many critical choices need to be made. Specifically, we must determine: (*i*) at which scale the desired behavior is best defined; (*ii*) at which scale measurements can be performed; and (*iii*) at which scale actuation can be executed. Typically, for complex systems, the desired behavior is related to emerging properties and is thus macroscopic; however, actuation can be performed microscopically, as we are often constrained to actuate only some of the units comprising the group. Measurements can also be acquired macroscopically, or, at least, starting from microscopic sensing, we can estimate macroscopic observables of the system. For a schematic representation of how the classical feedback control loop can be adjusted in the context of large-scale complex systems, see Fig. 1.2b. Note that in many real applications, microscopic

---

[2] Some literature [14] defines the mesoscopic level as the point where clustering behavior begins. Others [21] describe the mesoscopic scale as capturing the spatio-temporal dynamics of a group's density, while the macroscopic scale addresses the time dynamics of the density's momenta.

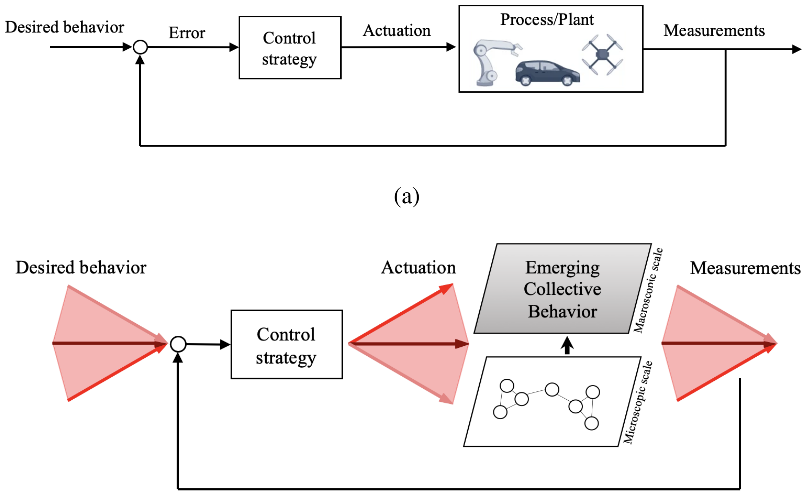

(a)

(b)

Figure 1.2: Control schemes for (a) a classical system (i.e., process, plant), and (b) a complex (multi-scale) system (red shaded arrows emphasize that each task can be performed on multiple description's scale).

control actions cannot be applied to all agents in the group. This limitation has led to the development of various pinning and leader-follower techniques for controlling such systems at the microscopic level [25].

## 1.2 Key research questions

This thesis focuses on understanding how to systematically close feedback control loops across different descriptive scales to effectively bridge the gap between the microscopic agent level and the macroscopic level of emerging behavior. In doing so, we aim to derive analytical guarantees of convergence toward the desired behavior. Moreover, we seek agile, resource-efficient methods for experimentally validating these control methodologies in large-scale complex systems.

## 1.3 Contributions of the Thesis

In this Thesis, we make contributions on three fundamental aspects in the broad area of modeling and control of large-scale complex systems.

We provide a general framework for the multi-scale control of complex systems accomplishing a macroscopic control goal through microscopic actuation and macroscopic sensing. We focus on spatial organization tasks and, in so doing, we utilize the *continuification control* paradigm [26]. Specifically, for a large swarm of mobile agents moving in domains of arbitrary size, we derive a continuum description of their dynamics in the limit of an infinite number of agents through mean-field theory [27, 28]. This process outputs a transport-diffusion equation describing the spatio-temporal dynamics of the group's density. Such a continuum/macroscopic description is used to perform a macroscopic control design ensuring convergence towards the desired behavior, and, it is finally discretized into deployable control inputs to microscopically actuate the agents in the collective. The robustness of this control pipeline can be analytically assessed in the continuum.

We expand this continuification-based framework to deal with leader-follower scenarios. In particular, to cope with the unrealistic assumption of being able to control every agent in the complex system of interest, we consider the case of actuating only a subset of the group. In the continuum limit, we are able to provide analytical conditions guaranteeing that a class of control problems is solvable. Such conditions leverage information about the leaders-to-followers ratio, the sensing capabilities of the leaders, and the stochasticity of the followers.

Finally, we consider the problem of the experimental testing of control methodologies for large-scale systems and swarm robotics. In particular, for exploiting the multi-scale nature of large-scale complex systems, many new control methodologies rely on the assumption of swarms of infinite agents. It is then understandable that the vast majority of such new techniques are solely tested in numerical simulations because of the inherent high cost and resources demand of full-scale experiments. In order to cope with these costs and still perform experiments, we provide an intermediate hybrid experimental platform. This set-up provides a mixed reality environment where real robots and virtual ones interact and cooperate, enabling the possibility of having a swarm of arbitrary size.

## 1.4 Relevance to risk and complexity

The work presented in this Thesis falls within the field of controlling and engineering complex systems. Specifically, it tackles the problem of controlling some dynamical units (or all of them) in a multi-agent system in order to let a desired macroscopic state emerge. We propose a systematic control pipeline to address the pressing open problem of how to close feedback loops across different description scales. We successfully bridge the gap between the agent/microscopic level, and the emergent/macroscopic one, while ensuring analytical guarantees of convergence towards desired states.

The mathematical framework we propose is suitable in many applications. For instance, it can be used for addressing swarm robotics problems, where large ensembles of mobile robotic agents need to accomplish some desired spatial organization. It can find application in search and rescue operations, where, a small set of controllable agents is in charge of driving other ones away from danger. Similarly, we can think of traffic control problems, where autonomous agents are in charge of smoothing traffic waves away, so to reduce the energetic consumption of the collective.

Our work also considers the open challenge of agile experimental testing of control techniques involving large-scale systems. Drawing inspiration from apparently uncorrelated fields, we propose a mixed reality platform which provides real robots and virtual ones. In such a context, we are able to create robotics groups of arbitrary size (by increasing the number of virtual agents), while effectively facing the cost of full-scale experiments.

## 1.5 Thesis structure and outline

This Thesis is organized as follows. In Chapter 2, we provide the reader with a Literature review concerning the main topics of the thesis. In Chapter 3 and 4, we collect the contribution given in [29, 30, 31, 32], regarding the continuification control of mobile agents moving in periodic domains of arbitrary size and its robustness properties. In Chapter 5, we show the work presented in [33], where we consider a macroscopic leader-follower scenario, in which, a group of leader agents is in charge of letting a group of followers agents displace according to a desired density. In Chapter 6, we expand such a leader-follower scenario for modeling switching leadership in large groups of agents. Specifically, we consider the case where a group of leaders and followers is collectively solving a spatial organization task, while online exchanging the leadership roles. In

Chapter 7, we discuss a mixed reality experimental platform we developed for the agile testing of control solutions for large-scale problems and swarm robotics. In Chapter 8, we discuss the conclusions and the direction for the future of this work.

## 1.6 Mathematical Preliminaries

In this Section we provide some useful notation and lemmas which are used throughout the thesis.

**Definition 1.1** (Periodic cube)**.** *We define* $\Omega := [-\pi, \pi]^d$ *as the periodic cube in* $\mathbb{R}^d$*. When* $d = 1$*,* $\Omega$ *coincides with the unit circle, and we equivalently refer to it by* $\mathcal{S}$*; when* $d = 2$*,* $\Omega$ *is the periodic square. If explicitly stated,* $\Omega$ *can also refer to different kind of spatial domains.*

**Definition 1.2** ($\mathcal{L}^p$ norms on $\Omega$ [34])**.** *Given a scalar function of* $\Omega$ *and time,* $h : \Omega \times \mathbb{R}_{\geq 0} \to \mathbb{R}$*, we define its* $\mathcal{L}^p$*-norm on* $\Omega$ *as*

$$\|h(\cdot, t)\|_p := \left( \int_\Omega |h(\mathbf{x}, t)|^p \, \mathrm{d}\mathbf{x} \right)^{1/p}. \tag{1.1}$$

*For* $p = \infty$*,*

$$\|h(\cdot, t)\|_\infty := \operatorname{ess\,sup}_{\mathcal{S}} |h(\mathbf{x}, t)|. \tag{1.2}$$

*For the sake of brevity, we also denote these norms as* $\|h\|_p$*, without explicitly indicating their space and time dependence.*

**Lemma 1.1** (Hölder's inequality [34])**.** *Given* $f_1, \dots, f_n \in \mathcal{L}^p(\mathcal{S})$*, we have*

$$\left\| \prod_{i=1}^n f_i \right\|_1 \leq \prod_{i=1}^n \|f_i\|_{p_i}, \quad \text{if} \quad \sum_{i=1}^n \frac{1}{p_i} = 1. \tag{1.3}$$

*For instance, if* $n = 2$*, we have* $\|f_1 f_2\|_1 \leq \|f_1\|_2 \|f_2\|_2$*, as well as* $\|f_1 f_2\|_1 \leq \|f_1\|_1 \|f_2\|_\infty$*.*

**Remark 1.1.** *The p-norm* $\|\cdot\|_p$ *can be also referred to vectors in* $\mathbb{R}^d$*. In this case, it needs to be interpreted as*

$$\|\mathbf{v}\|_p := \left( \sum_{i=1}^d |v_i|^p \right)^{1/p}, \tag{1.4}$$

*where* $\mathbf{v} = [v_1, \dots, v_d]$.

**Lemma 1.2** (Minkowsky inequality [34])**.** *Given two* $L^p$ *functions,* $f$ *and* $g$*, the following inequality holds:*

$$\|f+g\|_p \leq \|f\|_p + \|g\|_p, \tag{1.5}$$

*for* $1 \leq p \leq \infty$.

We denote by $\mathbb{n} = (n_1, \dots, n_d)$ the $d$-dimensional multi-index, consisting in the tuple of dimension $d$, with $n_i \in \mathbb{Z}$. Thus, $\mathbf{n} = [n_1, \dots, n_d]$ is the row vector associated with $\mathbb{n}$.

We denote with " $*$ " the convolution operator. When referring to periodic domains and functions, the operator needs to be interpreted as a circular convolution [35]. We denote by $C^p(\mathcal{S})$, with $p \in \mathbb{N}_{\geq 0}$, the space of functions that are differentiable $p$ times with a continuous $p$-th derivative on $\mathcal{S}$. We use $W^{k,p}(\mathcal{S})$ for the Sobolev space of functions defined on $\mathcal{S}$ (the weak derivatives up to order $k$ are in $\mathcal{L}^p(\mathcal{S})$). Furthermore, when $p = 2$, we use $H^k(\mathcal{S}) := W^{k,2}(\mathcal{S})$ [36]. When referring to the higher-dimensional case $\Omega$ with $d > 1$, $W^{k,p}(\Omega)$ denotes the space of functions with the following mixed partial derivative being well defined in a weak sense:

$$f^{(\mathbb{n})} = \frac{\partial^{\|\mathbf{n}\|_1} f}{\partial x_1^{n_1} \dots \partial x_d^{n_d}}, \tag{1.6}$$

for any multi-index $\mathbb{n}$ such that $\|\mathbf{n}\|_1 \leq k$.

We denote with subscripts $t$ and $x$ time and space partial derivatives. We indicate gradient as $\nabla(\cdot)$, divergence as $\nabla \cdot (\cdot)$, curl as $\nabla \times (\cdot)$, and Laplacian as $\nabla^2(\cdot)$.

**Lemma 1.3** (Young's convolution inequality [34])**.** *Given two functions,* $f \in L^p$ *and* $g \in L^q$*, we have*

$$\|f * g\|_r \leq \|f\|_p \, \|g\|_q, \quad \text{if} \quad \frac{1}{p} + \frac{1}{q} = \frac{1}{r} + 1, \tag{1.7}$$

*where* $1 \leq p, q, r \leq \infty$.

**Lemma 1.4** (Poincaré-Wirtinger inequality for $\mathcal{S}$ [37])**.** *Assuming* $1 \leq p \leq \infty$*, for any function* $u \in W^{1,p}(\mathcal{S})$ *with null integral mean (that is,* $1/2\pi \int_{\mathcal{S}} u \,\mathrm{d}x = 0$*), the following inequality holds:*

$$\|u\|_p^p \leq C(p) \, \|u_x\|_p^p, \tag{1.8}$$

*where* $C(p) > 0$ *is called the Poincaré constant. For* $p = 2$, $C = 1$ *[38, 39].*

**Remark 1.2.** *The inequality can be posed for more general bounded connected open domains* $\Omega \subset \mathbb{R}^d$ *with Lipschitz boundary [36, 40]. In this case, for any function* $u \in W^{1,p}$ *such that* $\int_\Omega u \, \mathrm{d}\mathbf{x} = 0$*, the inequality reads*

$$\|u\|_p^p \leq C(p, \Omega) \|\nabla u\|_p^p, \tag{1.9}$$

*where* $\nabla u$ *is the gradient of* $u$ *(notice that* $\|\nabla u\|_p^p = \sum_{i=1}^d \|u_{x_i}\|_p^p$*, with* $x_i$ *being the i-th coordinate in* $\Omega$*).*

**Remark 1.3.** *When* $p = 2$*, the optimal Poincaré constant for smooth bounded Lipschitz domains is* $C = \tilde{d}/\pi$*, where* $\tilde{d}$ *is least upper bound of the set of all distances between pairs of points in* $\Omega$ *[38].*

**Lemma 1.5** (Comparison lemma [41])**.** *Given a scalar non-autonomous ODE* $v_t = f(t, v)$*, with* $v(t_0) = v_0$*, where* $f$ *is continuous in* $t$ *and locally Lipschitz in* $v$*, if a scalar function* $u$ *fulfills the differential inequality*

$$u_t \leq f(t, u(t)), \quad u(t_0) \leq v_0, \tag{1.10}$$

*then*

$$u(t) \leq v(t), \quad \forall\, t \geq t_0. \tag{1.11}$$

**Lemma 1.6.** *If* $\gamma$*,* $\delta$ *and* $K$ *are positive constants with* $K \gg \gamma$*, the one-dimensional nonlinear dynamical system*

$$\eta_t(t) = -\gamma\, \eta(t) + \delta \exp(-Kt)\sqrt{\eta(t)}, \tag{1.12}$$

*with* $\eta \geq 0$*, globally and exponentially converges to 0. The rate of convergence is* $\gamma$*.*

*Proof.* Under the change of variable $\tilde{\eta} = \sqrt{\eta}$, we have

$$\tilde{\eta}_t(t) = -\frac{\gamma}{2}\tilde{\eta}(t) + \frac{\delta}{2}\exp(-Kt). \tag{1.13}$$

Equation (1.13) describes a linear one-dimensional non-autonomous dynamical system. Hence, its solution is

$$\tilde{\eta}(t) = \tilde{\eta}(0)\exp\left(-\frac{\gamma}{2}t\right) + \frac{\delta}{\gamma - 2K}\left(\exp\left(-Kt\right) - \exp\left(-\frac{\gamma}{2}t\right)\right). \tag{1.14}$$

The convergence of $\eta$ is implied by (1.14). Since $K \gg \gamma$, the rate of convergence of $\tilde{\eta}$ is $\gamma/2$, and that of $\eta$ is $\gamma$. ■

**Lemma 1.7** (Chapter 1.2 of [42])**.** *Given a scalar function $\psi$, and a vector field $\mathbf{A}$, the following identity holds:*

$$\nabla \cdot (\psi \mathbf{A}) = \psi \nabla \cdot \mathbf{A} + \nabla \psi \cdot \mathbf{A}. \tag{1.15}$$

**Lemma 1.8.** *For any function $h$ that is periodic on $\partial\Omega$, we have*

$$\int_{\partial\Omega} h(\mathbf{x}) \cdot \hat{\mathbf{n}} \, \mathrm{d}\mathbf{x} = 0, \tag{1.16}$$

*where $\hat{\mathbf{n}}$ is the is the outward pointing unit normal vector at each point on the boundary (by decomposing the integral on each side of the domain with the appropriate sign).*

# 2 Background

In this Chapter, we give an overview of the Literature for the topics which are more relevant and related to the work in this Thesis. Specifically, the Chapter is organized into three parts: the first part, consisting of Sections 2.1, 2.2, 2.3 and 2.4, is focused on describing the existing Literature on macroscopic modeling and control techniques for complex multi-agent systems (a schematic overview of this part of the Chapter is provided in Tab. 2.1); the second part (Section 2.5) discusses existing methods for applying macroscopic techniques to leader-follower scenarios; finally the third part (Section 2.6) describes experimental testing set-ups for the validation of control techniques for large-scale systems and swarm robotics.

## 2.1 Modeling and control of large-scale multi-agent systems

A pressing open challenge in control theory is to find methods to steer the collective behavior of large-scale multiagent systems consisting of many dynamical units (or agents) interacting with a given, and possibly time-varying, network topology. Examples of this problem include multirobot systems [22, 43, 44], cell populations [45, 46], and human networks [10, 47]. From a mathematical viewpoint, such systems are typically described as a set of $N$ stochastic differential equations, describing identical, undirectedly interacting dynamical systems [1], that is

$$\mathrm{d}\mathbf{x}_i = \sum_{j=1}^{N} a_{ij}(t)\mathbf{f}(\mathbf{x}_i, \mathbf{x}_j)\,\mathrm{d}t + b_i\mathbf{u}_i(\mathbf{x}_1, \dots, \mathbf{x}_N)\,\mathrm{d}t + \sqrt{2D}\,\mathrm{d}\mathbf{W}_i, \quad i = 1, \dots, N, \qquad (2.1)$$

where $\mathbf{x}_i \in \Omega \subseteq \mathbb{R}^n$ is the $n$-th dimensional state of agent $i$, $a_{ij}$ is the $ij$-th element of a time varying adjacency matrix $\mathbf{A}$ ($ij$-th entry of such a matrix is either 1 or 0 at time $t$ –

if agents $i$ and $j$ are able to communicate at time $t$ it is 1, 0 otherwise), $\mathbf{f} : \mathbb{R}^n \longrightarrow \mathbb{R}^n$ is a function describing the information that is exchanged between agent $i$ and $j$, $b_i \in \{0, 1\}$ is a flag which is 1 if agent $i$ is affected by the control input $\mathbf{u}_i$, 0 otherwise, $D$ is a constant diffusion coefficient, and $\mathbf{W}_i$ is a standard Weiner process in $\mathbb{R}^n$.

Modeling and control of large-scale complex multi-agent systems need to account for their multi-scale nature [14]. As highlighted in Chapter 1 (see Fig. 1.1, and Fig. 1.2), such systems can be described at two scales. At the microscopic level, it is possible to model the dynamics of each agent of the group, together with local interactions with the others and, eventually, control inputs. Such a framework, usually exploits large sets of ODEs or SDEs like (2.1), where, each equation is associated with the state of an individual in the collective. Then, macroscopically, the group exhibits a collective emerging behavior, which typically it is difficult to be linked with the individuals' capabilities of the agents. For this reason, macroscopic descriptions usually are based on small sets of PDEs, catching in a more compact way the emerging behavior of interest. These macroscopic descriptions also cope with the inherent curse of dimensionality of agent-based models, as they offer mathematical formulations which are more compact and amenable for analysis and control design [14]. An interesting drawback of macroscopic formulations is the so-called, *microscopic distraction* [48]. This consists in the natural loss of information about individuals when macroscopic descriptions are adopted. Such a problem is particularly relevant for scenarios in which control can only be performed via actuation at the microscopic level.

As a paradigmatic example, we can think of a large swarm of mobile robots, that is tasked to achieve some macroscopic spatial organization. In analogy with fluid-dynamics [50], a large set of interacting particles may be macroscopically described in terms of the spatio-temporal dynamics of the group's density [14]. Although such a model compactly describes the group's spatial organization, it loses information about individual agents' positions. This microscopic distraction is a problem to deal with in control applications, where macroscopic control actions needs to be discretized into control inputs deployable at the microscopic level. A conceptualization is provided in Fig. 2.1.

A possible way to exploit the nice scalability properties of macroscopic descriptions, while dealing with the microscopic distraction phenomenon, is represented by *continuification* (or *continuation*) methods[1]. Such a control paradigm has been recently introduced in [26] and it consists in the pipeline in Fig. 2.2; specifically, the control design goes

---

[1] Although such methodologies were introduced under the name of "*continuation*" methods, we prefer to refer to them using "*continuification*", in order to clearly state the difference with the field of parametric continuation and bifurcation theory.

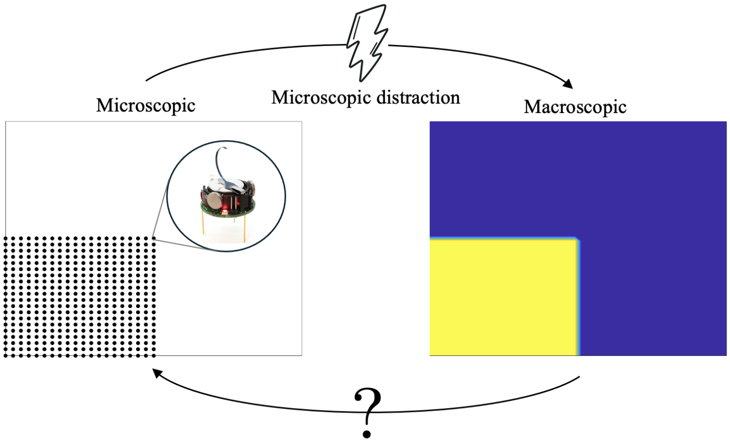

Figure 2.1: Microscopic vs macroscopic description for a swarm of kilobots [49] keeping a regular formation in the bottom-left corner of some domain: the passage from micro to macro allows not to account for the state of each kilobot (left box), in favour of a group description focusing on their density (right box); the passage from micro to macro is not easily reversible because of the lost information on the individuals' robot behavior (microscopic distraction).

through the following steps:

- **continuification:** derive a macroscopic description of the emerging behavior to control in the form of a small set of PDEs, starting from an agent-based description in the form of a set of ODEs or SDEs;
- **macroscopic control design:** use the macroscopic description of the emerging behavior to control to develop a macroscopic control action with guarantees of convergence;
- **discretization:** link the macroscopic control action with the microscopic control inputs for controllable units of the complex system.

The continuification paradigm offers a natural framework to design control across different description scales. In particular, the macroscopic description is derived starting from its microscopic counterpart, and it is used to design a macroscopic control action. The macroscopic scale gives a naturally scalable environment as it is independent from the number of agents involved, and looks at the group as a single entity. Such formulations can be utilized to derive analytical guarantees of convergence for the control strategies, because they are more amenable to analyze with respect to their microscopic

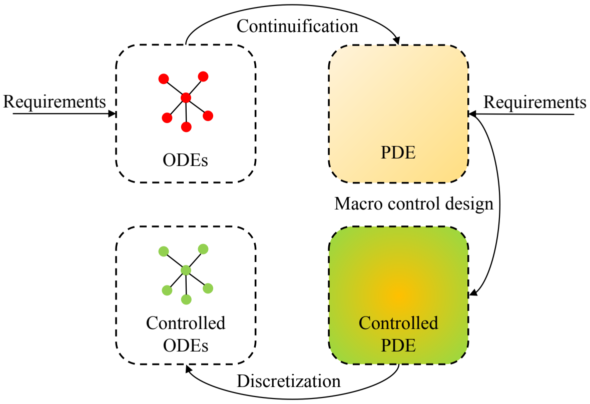

Figure 2.2: Continuification control pipeline: starting from an agent-based description, through continuification, a PDEs model of the emerging behavior to control is derived; such a model is used to develop a control strategy, that is then discretized onto the microscopic dynamics of the agents; control requirements may enter both at the microscopic and macroscopic scale.

counterparts. Macroscopic control strategies are then discretized into microscopic control inputs with ad-hoc methods to deal with the microscopic distraction phenomenon. The continuification paradigm has been recently used for the synchronization control of spin-torque oscillators [51] and for the stabilization of chains of coupled semiconductor lasers [52].

In this Chapter, we categorize the Literature for the modeling and control of complex systems using the continuification paradigm. In particular, we first present techniques for linking microscopic descriptions of complex systems with the macroscopic description of their emerging behaviors. Then, we go through the field of PDEs control, regarding the macroscopic control design. Finally, we consider some techniques for the discretization of macroscopic control inputs. A schematic overview of the Literature that is considered in this Chapter is provided in Tab. 2.1. We want to remark that, as highlighted in Tab. 2.1, in this Thesis, we refer to continuification control when dealing with approaches involving all the three steps schematized in Fig. 2.2. When referring to techniques to perform the micro to macro step, we will as well use the term continuification.

## 2.2 Continuification techniques

In this Section, we discuss the Literature on continuification techniques, consisting of methodologies for deriving macroscopic descriptions of emerging behaviors from microscopic agent-based models.

### 2.2.1 Mean-field approaches

The microscopic description of a set of $N$ undirectedly interacting dynamical systems is typically in the form of (2.1). Assuming agents to be connected through a time-invariant all-to-all topology ($a_{ij} = 1, \forall i \neq j$), $b_i = 1$ for each $i = 1, \dots, N$ (all the agents are controllable), and under suitable conditions on $\mathbf{f}$ (odd-symmetric and soft-core – see [53] for more details), it is possible to derive a macroscopic description of the group using mean-field theory [27, 28]. As in [53, 54], assuming $N \to \infty$, we can recast the microscopic dynamics into the transport-diffusion equation[2] for the density distribution of the state of the system $\rho : \Omega \subseteq \mathbb{R}^n \times \mathbb{R}_{\geq 0} \to \mathbb{R}_{\geq 0}$,

$$\rho_t(\mathbf{x}, t) + \nabla \cdot [\rho(\mathbf{x}, t) \, (\mathbf{V}(\mathbf{x}, t) + \mathbf{U}(\mathbf{x}, t))] = D\nabla^2\rho(\mathbf{x}, t), \tag{2.2}$$

where

$$\mathbf{V}(\mathbf{x}, t) = \int_\Omega \mathbf{f}(\mathbf{x} - \mathbf{y})\rho(\mathbf{y}, t) \, \mathrm{d}\mathbf{y} = (\mathbf{f} * \rho)(\mathbf{x}, y) \tag{2.3}$$

is the macroscopic counterpart of the vector field describing agents' all-to-all interactions, and $\mathbf{U}$ is a macroscopic control action, accounting for $\mathbf{u}_i$ in the continuum. Equation (2.2) needs to be complemented with initial conditions, and boundary conditions so as to guarantee some mass conservation principle, that is

$$\left( \int_\Omega \rho(\mathbf{x}, t) \, \mathrm{d}\mathbf{x} \right)_t = 0, \tag{2.4}$$

is satisfied. Although agents are assumed to interact through an all-to-all topology, usually, the function $\mathbf{f}$ is chosen such that it decays with $|\mathbf{x} - \mathbf{y}|$. For a group of swarming agents/robots, this means that interactions decays with the distance between them, hence approximating proximity interactions.

---

[2] Following [55], this PDE goes under the name of McKean-Vlasov equation; if the underlying microscopic agents are non-interacting and deterministic ($D = 0$), such a PDE takes the name of Liouville equation [56]; when agents are non-interacting and stochastic, the PDE is referred as Fokker-Plank equation.

[3] As pointed out in Sec. 2.4 PdEs recast a set of ODEs, hence a discretization step is not explicitly needed.

| **Literature overview on macroscopic modeling and control** | | | |
|---|---|---|---|
| Continuification control | Continuification techniques | Mean-field theory | [53, 54, 57, 58]<br>[59, 60, 61, 62]<br>[63, 64, 65] |
| | | Graphons theory | [66, 67, 68]<br>[69, 70] |
| | | Finite Differences approximations | [26, 51, 52] |
| | | PdEs | [71, 72, 73] |
| | | Data-driven methods | [74, 75, 76, 77] |
| | Macroscopic control design | Boundary | [48, 52, 78, 79]<br>[80, 81] |
| | | In domain: | |
| | | Mean-field optimal control | [61, 82, 83, 84]<br>[60, 85, 86, 87] |
| | | Moving bottlenecks | [88, 89] |
| | | Ensemble control | [56, 90, 91, 92] |
| | | Optimal transport | [93, 93, 94] |
| | | Graphons control | [67, 95, 96, 97] |
| | | PdEs control | [71, 72, 73] |
| | Discretization techniques | Finite difference discretization | [26, 51, 52] |
| | | PdEs discretization[3] | [71, 72, 73] |

Table 2.1: Overview of the Literature about macroscopic modeling and control that is considered in this Thesis. Notice that many techniques do not follow all the three steps of the continuification control pipeline (continuification, macroscopic control design and discretization).

This continuification technique is often utilized in the Literature, especially in those problems regarding agents performing spatial organization tasks, e.g. [57, 58, 59, 60, 61, 62]. For instance, in the context of locust swarming, such continuum models have been successfully used to derive analytical steady-state solutions for various kinds of interaction functions **f** [53, 63, 64, 65]. More recently, such mean-field approximations have been used to derive open-loop control protocols for large groups of swarming agents, inspired by the ants' collective behavior [98].

To summarize, mean-field approaches represents a viable option for performing the continuification of large-scale complex systems, as, in the limit of an infinite number of agents, they allow to recover tractable mass conservation laws as (2.2). The main drawback of such technique is related to the (sometimes) limiting assumption about having an all-to-all topology describing the scheme of interactions among the agents. However, depending on the context, such an assumption is mitigated by choosing kernels

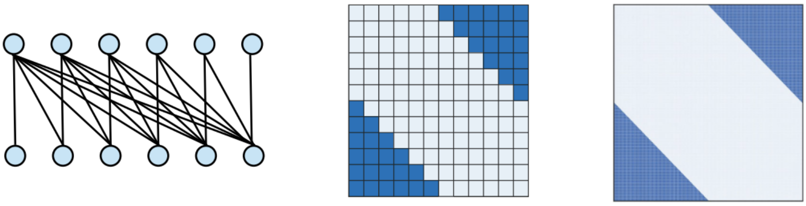

Figure 2.3: Graphical interpretation of a graphon: on the left a bipartite half graph, in the middle its representation through a pixel plot, on the right its associated graphon (this figure is reproduced from [66]).

of interaction decaying with the distance. For instance, in this Thesis, we adopt mean-field techniques for deriving macroscopic descriptions that are then used for control design. This represents a reasonable choice because it well approximates agents interacting through a proximity network, that is a common assumption when dealing with swarming agents performing spatial organization tasks, as those we deal with here.

### 2.2.2 Graphons theory

Another continuification technique, which has its foundations in mean-field theory, is the so-called graphon theory [99, 100]. In particular, within this context, it is possible to derive macroscopic descriptions similar to (2.2), for agents interacting on network topologies which are more complex than all-to-all ones. Specifically, a graphon is the limiting object of a dense graph when the number of nodes goes to infinity (preserving the topology). In particular, the nodes' space is mapped to $[0, 1]$ so that a weighted adjacency matrix can be represented as a symmetric measurable function $W : [0, 1]^2 \to [0, 1]$ (see Fig. 2.3 for a graphical interpretation). Notice that the existence of a graphon is not independent from the graph topology, thus the existence of a graphon $W$ is not ensured for any arbitrary network of infinite nodes[4].

If the topology in (2.1) is such that it can be expressed through a graphon, a macroscopic description for the system can be derived in the same form as (2.2). The only difference is that, the graphon $W$ affects the definition of (2.3), that is, for the one-

---

[4] The existence of a graphon is proved, for instance, for Erodos-Renyi random topologies and complete bipartite graphs (half graphs)

dimensional case,

$$V(x,t) = \int_0^1 \int_\Omega W(x,z) f(x-y) \rho(y,t) \, \mathrm{d}y \mathrm{d}z. \tag{2.5}$$

For linear systems on graphons, the dynamics consistently simplifies (we refer the reader to [66, 67] for more details).

Macroscopic graphons-based descriptions of dynamical systems have been used to study synchronization of power networks in [68]. Specifically, after modeling nodes in the power network as Kuramoto oscillators [69] on specific topologies, their macroscopic description is derived. Moreover, graphons have been used to perform sensitivity analysis of epidemics models [70], and model opinion dynamics [101]. The concept of graphons has been recently extended to the more general idea of graphops [102, 103], which look at graphs as operators.

Graphons represent a natural and elegant extension of mean-field approaches to account for topological effects. However, only a small subset of topologies can be accounted in such descriptions.

### 2.2.3 Finite difference approximations

Another possibility to perform the continuification of dynamical systems is the one proposed in [26], and applied in [51, 52]. Therein, the key idea is to look at sets of coupled linear dynamical systems as the discretization, through finite differences, of some PDE. As a motivating example, we consider an infinite set of one-dimensional agents with state $\rho_i \in \mathbb{R}$ displaced on the real line at a constant distance $\Delta x$. Their dynamics is set as

$$\dot{\rho}_i = \frac{1}{\Delta x} \left( \rho_{i+1} - \rho_i \right). \tag{2.6}$$

Notice that each agent is interacting with the one ahead of it. Equation (2.6) can be viewed as the discretization using forward finite differences of the transport PDE

$$\rho_t(x,t) = \rho_x(x,t). \tag{2.7}$$

This mechanism can be generalized to linear dynamical systems interacting on spatially-invariant network topologies. In such a set-up, and with additional assumptions, it can be proved that the continuified PDE converges, in spectrum, to the underlying system of ODEs (see Theorem 2 in [26]). Many useful heuristic extensions were proposed in [26] to deal with nonlinear systems interacting on more general network topologies. However, the micro-to-macro convergence is ensured only in the simple scenarios of linear agents interacting on spatially-invariant network topologies.

### 2.2.4 Partial difference equations (PdEs)

In a similar vein to the technique in Sec. 2.2.3, the framework of partial difference equations (PdEs) is introduced in [71, 72, 73], extending the results of [104]. In this field, sets of ODEs can be recast into PdEs, which represents an intermediate level of abstraction between ODEs and PDEs. Within this context, a class of complex multi-agents systems (linear, with an arbitrary topology, and with diffusive coupling) is analyzed and controlled with linear and non-linear techniques so as to achieve spatial organization.

As a paradigmatic example, systems in the form of (2.1) (fixing a time invariant topology $a_{ij}(t) = a_{ij}$, an homogeneous control action $b_i = 1$, $D = 0$, and diffusive coupling $\mathbf{f}(\mathbf{x}_i, \mathbf{x}_j) = \mathbf{x}_j - \mathbf{x}_i$) are recast as the PdE

$$\dot{\mathbf{x}}(i,t) = \Delta\mathbf{x}(i,t) + \mathbf{u}(i,t), \tag{2.8}$$

where $i \in \{1, \ldots N\}$, $\mathbf{x}(i,t) = \mathbf{x}_i(t)$, $\mathbf{u}(i,t) = \mathbf{u}_i(t)$, and

$$\Delta\mathbf{f}(\mathbf{x}) = \sum_{j=1}^{N} a_{ij}\left[\mathbf{f}(\mathbf{x}_j) - \mathbf{f}(\mathbf{x}_i)\right]$$

is the Laplacian operator for PdEs.

It can be noticed that the paradigmatic PdE in (2.8) recasts a set of ODEs in a compact form which mimics that of a PDE on a graph topology. What makes this framework useful is that, by means of functional analysis, many mathematical tools for PDEs can be generalized to PdEs, thereby enabling their rigourous and analytical study and intuitive physics-based conjecturing about the underlying microscopic formation (see [71, 72] for more details).

This mathematical set-up allows to perform the analysis and control of complex multi-agent systems within a continuum framework that can preserve topological information about the agents. However, assumptions about the linearity of the agents and the nature of their coupling limits its applicability in context different from that of the control of unmanned autonomous vehicles.

### 2.2.5 Data-driven methods

A consistent amount of Literature is devoted to data-driven continuification methods, also referred as PDEs *discovery*. In particular, starting from real or synthetic data, the aim is to recover macroscopic models of emerging behaviors of complex systems. In [74], a deep-learning method, namely PDE-READ, is developed to discover PDEs. The tool is based on two neural networks. The first one is in charge of learning the system's response, while the second one needs to extract the PDEs macroscopic formulation, which is then refined into a "human-readable" model via a parameter-free sparse regression. This technique proved to be successful on a number of benchmark problems. Similarly, sparse regression can be used to perform data-driven PDEs learning [75].

Manifold learning can also be used to understand which are the more relevant coordinates of data, so to more effectively perform PDEs learning via neural networks [105].

Currently, these data-driven methodologies have not been used in control applications other than that performing bifurcation analysis with respect to parameters variations [76, 77]. This is because the resulting macroscopic models cannot account for the presence of terms to be fixed with a real-time feedback fashion.

## 2.3 Macroscopic control design

Once a macroscopic description of a large-scale complex system is derived in the form of a small set of PDEs, it has to be controlled using methodologies developed in the context of PDEs' control [106]. Following the taxonomy in [106], the behavior of phenomena that are described by infinite-dimensional systems can be managed with two possible strategies

- **in domain** control, where actuation and sensing penetrate inside the domain of the PDE system,
- **boundary** control, where sensing and actuation can be performed only through the boundary conditions of the PDE.

Notice that boundary control is physically more realistic for phenomena that are intrinsically described by PDEs. For instance, in the framework of fluid dynamics, control and measurements are typically performed through the vessel walls. On the other hand, for PDEs that are derived as macroscopic descriptions of large-scale complex systems, it is reasonable to think about performing in domain control, as measurements and actuation will be finally realized through agents moving in the PDE's domain.

A general procedure for boundary control of linear PDEs in one-dimension is presented in [106]. It is based on *backstepping*, a framework which improves and generalizes that of feedback linearization [107]. The idea of PDEs backstepping consists of the following steps: $(i)$ identify undesirable terms in the PDE (that are those producing instabilities), $(ii)$ choose a target system where undesirable terms are eliminated by state transformations and feedback, $(iii)$ find the state transformation in the form of a Volterra operator (which naturally satisfies linear PDEs), $(iv)$ design the boundary feedback to eliminate instabilities (the state transformation brings the undesirable terms on the boundary so that they can be managed with boundary control). For instance, we can consider the unstable reaction-diffusion equation in $[0, 1]$ given by:

$$\begin{aligned} u_t(x,t) &= u_{xx}(x,t) + \lambda u(x,t) \\ u(0,t) &= 0 \\ u(1,t) &= U(t) \end{aligned} \tag{2.9}$$

where $\lambda$ is an arbitrary constant and $U(t)$ is the control input. The source of instability is $\lambda u(x,t)$, and the idea of backstepping is to use the coordinate transformation

$$w(x,t) = u(x,t) - \int_0^x k(x,y)u(y,t)dy \tag{2.10}$$

and the boundary control

$$U(t) = \int_0^1 k(1,y)u(y,t)dy \tag{2.11}$$

to transform (2.9) into the target system

$$\begin{aligned} w_t(x,t) &= w_{xx}(x,t) \\ w(0,t) &= 0 \\ w(1,t) &= 0 \end{aligned} \tag{2.12}$$

which is exponentially stable. The goal is then to find the “right" kernel $k(x,y)$ verifying (2.10) and (2.11) while satisfying a linear and easily solvable PDE (see [106] for further details).

Boundary control has been successfully used in the context of continuification control (micro-to-macro, macroscopic control design, and the macro-to-micro). For instance, in [52] the problem of stabilizing a chain of coupled semiconductor lasers is assessed, while in [48, 80, 81] formation control problems are considered (both in leader-less and leader-follower scenarios). Moreover, boundary control can be developed through reinforcement learning techniques, among the open source platform *controlgym* [78, 79].

Among in-domain strategies, mean-field optimal control recently gained a lot of momentum [82]. Within this framework, large sets of agents moving in some domain are considered and, transport-diffusion equations[5] are derived through mean-field theory (see Sec. 2.2.1). Then optimization problems can be formulated so as to look for optimal macroscopic control actions regarding some desired task to solve. Usually, the convergence of the microscopic optimization problem into the macroscopic one, and the existence of solutions of such optimal control problems can be proved, but nothing can be said about their functional form (it cannot be granted that the solution is in a feedback form, for example). Sometimes such optimal strategies are practically approximated by sub-optimal ones using model predictive control methods [83, 84].

Such a framework has been extended to enhance sparsity in the control action [61], explicitly accounting for additive noise in the agents dynamics [60], and assuming control can be exerted only through some microscopic agents [85]. Moreover, mean-field optimal control has been successfully used to tame crowd dynamics [86] and traffic control problems [87], although not explicitly accounting for any discretization procedure for the macroscopic control actions.

Similar optimal control problems arise in the context of *ensemble control* [56, 90, 91, 92]. Therein, PDE models are developed and controlled not to tame the curse of dimensionality of large-scale systems, but to model class of systems sharing the same structure but different parameters' values. Moreover, analogous set-ups appear in optimal transport of deterministic and stochastic agents [93, 94]. In this context, the optimal controlled velocity field is analytically recovered, and it can be granted to be in feedback form [93] (although in the case of non-interacting microscopic agents). Such a macroscopic control action is indeed a function of the co-state equation for a PDEs-constrained optimal control problem, which has not yet been solved in closed form.

Within the field of traffic control, mean-field macroscopic descriptions have been extended to account for *moving bottlenecks* [88, 89]. Therein, autonomous vehicles moving in the continuum traffic flow exert control actions as mobile constraints limiting the admissible traffic flow in specific regions.

---

[5] Diffusion is considered when noise affects the microscopic dynamics of the agents

Still in the context of mean-field approximations of the microscopic dynamics of large-scale complex systems performing a spatial organization task, in [98], a set of continuous obstacles is displaced in the domain of interest so to achieve a desired configuration. Therein, the stability of the proposed solution is not assessed.

When mean-field descriptions are improved with graphons to account for topological structures different from all-to-all ones, some specific control frameworks have been developed [67, 95, 96, 97]. In particular, assuming the microscopic agents' dynamics to be linear, traditional control strategies as linear quadratic (Gaussian) regulators can be designed and applied.

When partial difference equations (PdEs) are used to perform the continuification step, they can be combined with automatic control (both linear and nonlinear techniques) to perform spatial organization tasks [71, 72, 73, 108]. Specifically, in that framework, techniques such as Laplacian control and virtual forces are used to accomplish alignment, containment, and formation control problems.

The field of macroscopic control design falls within that of PDEs' control. For historical and technological reasons, the largest part of the Literature about control methodologies for PDEs involves the design of boundary control protocols. In-domain techniques, instead, became popular more recently, when the idea of macroscopic modeling and control of complex systems spread out. The main limitation of existing in-domain techniques is that they are developed without explicitly accounting for applicability constraints. For instance, in the mean-field optimal control community, the existence of optimal solution is usually assessed, but the problem of how to encode them in a discrete swarm of agents is not considered. We also remark that, in the Literature, optimal control problems constrained by mean-field dynamics gained a lot of momentum, but, indeed, less space has been given to other approaches, like the one which is considered in this Thesis (see Chapter 3) in the context of a continuification control pipeline (where control is developed with the idea of discretizing it into deployable control inputs).

## 2.4 Discretization

According to the continuification control scheme (see Fig. 2.2), once a macroscopic control action is found, with, for instance, one of the techniques discussed in Sec. 2.3, and ensures convergence, it needs to be discretized so as to compute deployable control inputs for the controllable agents in some large collective.

The vast majority of the Literature about continuification and macroscopic control design does not explicitly take into account the discretization step. However, it is fundamental to overcome the microscopic distraction phenomenon (see Fig. 2.1) and effectively close a feedback loop across the microscopic and macroscopic scale.

In [26, 51, 52], where agents are assumed to interact on lattice spatially-invariant topologies (see Sec. 2.2.3), the macroscopic control action is synthesized in the form of a differential operator of the system's state. Within this context, the continuum control action can be discretized with an arbitrary scheme of finite differences (depending on the specific spatially-invariant topology). For example, let us consider a large group of single integrators equally displaced on the unit circle $\mathcal{S}$, each of them displaced at constant distance $\Delta x$ at some fixed position $x_i \in \mathcal{S}$ with state $\rho_i \in \mathbb{R}$. Their macroscopic description can be derived using the technique described in Sec. 2.2.3 as

$$\rho_t(x,t) = u(x,t), \tag{2.13}$$

where $\rho$ is the macroscopic state and $u$ the macroscopic control action (to cope with the periodic domain, boundary conditions are set so to make $\rho$ periodic). If we consider the consensus problem of driving the agents' state to the same constant value, say $C$, it is easy to notice that, choosing the feedback action

$$u(x,t) = \rho_{xx}(x,t), \tag{2.14}$$

solves the problem (the error system $e = C - \rho$ takes the form of the heat equation $e_t = -e_{xx}$ which globally asymptotically converges to $0$[6]). The macroscopic control action (2.14) can be discretized with a central finite difference scheme, that is

$$u_i(t) = \frac{\rho_{i+1}(t) - 2\rho_i(t) + \rho_{i-1}(t)}{\Delta x}, \tag{2.15}$$

where $\rho_i(t) = \rho(x_i, t)$. This leads to choosing the control action for the $i$-th agent as a function of its state and that of its neighbors[7]. Different finite differences schemes can be chosen to adapt to different (spatially invariant) networks topologies. For large systems lying on non-spatially invariant networks (such as mobile robotic agents), the same procedure can be adapted (see Section VI of [26] for a practical example).

We remark that control techniques that are developed in the context of PdEs [71, 72,

---

[6] Substituting (2.14) in (2.13), we get the heat equation $\rho_t = \rho_{xx}$ with periodic boundary conditions. At steady-state, $\rho$ must be constant for periodicity reasons, and global stability can be proved fixing the Lyapunov functional $V = \|e\|_2^2$ (see for instance [106]). It can be also proven that the consensus value $C$ is the integral mean of the initial condition.

[7] Such a control action matches the microscopic counterpart of the problem, where, consensus for a group of single integrators can be achieved by diffusive coupling with the neighbors.

73] do not need to be explicitly discretized as they resemble the underlying microscopic dynamics by construction (see Sec. 2.2.4).

In this Thesis we always derive macroscopic descriptions of large-scale complex multi-agent systems by using mean-field arguments. This results in macroscopic models in spatial coordinates which can be resembled as (2.2), where control is exerted through the field $\mathbf{U}$. The discretization of such a control action will be perceived with an alternative procedure with respect to the ones shown in this Section. This consists in a spatial sampling of $\mathbf{U}$ at the spatio-temporal locations where controllable agents are. This methodology is also used in [98] for testing the proposed control solution in a discrete framework.

## 2.5 Leader-follower control solutions

Orchestrating the collective spatial organization of multi-agent systems is crucial in fields such as traffic control [109], collective additive manufacturing [110], synthetic biology [111], swarm robotics [112], and environmental management [113]. Leader-follower control strategies, where leader agents steer the behavior of a group of follower agents, are widely applied in these areas and other control applications [10, 11, 114, 115, 116, 117]. For example, the use of controlled autonomous vehicles has been proposed to improve traffic flows, avoiding stop-and-go waves and reducing emissions [15, 89]. In swarm robotics and synthetic biology, leader-follower dynamics can facilitate the management and regulation of large groups and cellular consortia [118, 119, 120, 121].

A key challenge is establishing analytical guarantees for achieving desired collective tasks. For instance, in the shepherding control problem, it is crucial to determine the optimal leader-to-follower ratios and sensing ranges to effectively manage group dynamics and corral and contain the followers towards desired regions in the state space [17, 122, 123, 124]. In complex multi-agent scenarios, microscopic models using ordinary (stochastic) differential equations are often replaced by macroscopic models using partial differential equations to simplify analysis and enhance control of spatial organization on a large scale, avoiding its inherent curse of dimensionality [29, 30, 31, 48, 51, 52, 57, 58, 67, 98, 125, 126, 127].

Within the domain of mean-field optimal control, significant advances have been made in addressing the well-posedness of macroscopic leader-follower formulations. In particular, the influence of a relatively small set of microscopic agents on an infinite population of followers is considered in [128] and [60], for deterministic and stochastic followers, respectively. This results in a coupled system composed of ordinary (or stochastic) and partial differential equations. In [129] and [130], the group dynamics is modeled via two coupled continuum equations for the densities of the two populations, for stochastic and deterministic followers, respectively. The existence of an optimal strategy is confirmed therein; however, explicit optimal solutions are not derived, nor it is studied if these solutions are implementable through feedback control – a gap our research aims to address.

The challenge of configuring followers into predefined structures, while varying the information available to leaders, is discussed in previous works such as [131, 132, 133]. In these scenarios, the followers' dynamics are typically represented by a heat equation, which macroscopically models a consensus protocol [71, 72]. The boundary conditions of this equation are controlled by leader agents. This setup examines the impact of different levels of leader information on the effectiveness in directing follower groups into desired formations.

The literature also highlights substantial contributions concerning networks of distributed parameter systems, often modeled by wave equations, as extensively discussed in [134, 135], and related references. These studies develop strategies aimed at steering these systems towards a consensus state.

In Chapter 5 and 6 of this Thesis, we present a macroscopic continuum model for leader-follower spatial organization tasks. In such a context, we are able to recover necessary and sufficient conditions regarding, for instance, the leaders-to-followers ratio making the problem solvable, and we recover control actions in closed form ensuring global (or local) guarantees of convergence.

## 2.6 Experimental validation of control solutions for large-scale multi-agent systems

Several new techniques for the analysis and control of large-scale multi-agent systems rely on the assumption that the interacting dynamical systems of the ensemble (*agents*) are numerous enough to be described in a continuuum framework [26, 29, 30, 66, 67].

Recasting complex multi-agent systems into continuum formulations offers new opportunities for the analysis and design of novel control approaches to tame collective dynamics. A pressing open challenge is to find agile methods to inform and experimentally validate the synthesis of control algorithms developed in a continuum framework [136], avoiding the inherent intense cost and hurdle of full-scale experiments with large-scale systems.

Full-scale experimental validation of control strategies for the control of large-scale multi-agent systems have been recently carried out [43, 137, 138, 139, 140]. For instance, in the seminal work [43], a swarm of over 1000 kilobots [49], has been behaviorally programmed to displace according to desired spatial configurations. Also, in [140], the same experimental set-up leveraging kilobots has been used to solve the task of collectively transporting complex objects. However, the majority of the existing control solutions have been tested only using computer simulations due to practical limitations.

In the apparently disjoint field of disability studies, researchers developed virtual reality environments to create digital twins of patients, and systematically test new techniques to assist them. Specifically in [141, 142], new assistive technologies for visually impaired persons were developed and tested on a sample of healthy subjects equipped with different kinds of virtual visual impairment. Similarly, in the field of animal behavior research [143, 144, 145, 146], virtual replicas or robots mimicking animals have been used to enhance the understanding of their behavior.

Bringing insights from these fields, it is possible to use virtual reality to perform experiments with robots. Interesting mixed reality settings have been presented in [147, 148, 149], where, real robots interact with simulated replicas in a shared environment. With a similar fashion, in the field of swarm robotics, augmented reality has been used to provide simple testbed agents, like kilobots, with augmented sensing capabilities [150, 151], in order to let them solve more complex tasks.

All these experimental set-ups leveraging virtual reality are not explicitly developed to reduce the intense cost of full, large-scale experiments. Hence, a current gap in the literature is to develop an experimental platform for avoiding the bottleneck of extreme time cost and resources of experiments of large-scale systems. Such a platform should be ($i$) flexible with respect to the kinematic/dynamical model of the virtual robots to integrate, and not be constrained to specific commercial robots, and ($ii$) easy to implement using existing open-source facilities, like the Robotarium at GeorgiaTech [152]. In Chapter 7 of this Thesis, we present a mixed reality platform tackling these open problems, providing also a hybrid experimental validation of the methodologies developed in Chapter 3 and 5.

## 2.7 Discussion

In this Chapter, we reviewed the relevant Literature regarding the broad area of modeling and control of large-scale complex systems. Specifically, we used the continuification control paradigm (see Fig. 2.2) to categorize solutions for multi-scale control problems. In particular, we divided the Literature using the three fundamental steps of continuification control [26], namely (*i*) continuification, i.e. the passage from the microscopic to the macroscopic scale, (*ii*) macroscopic control design, that is the design of control actions for PDEs describing large-scale complex systems in the continuum, and (*iii*) discretization, that consist in methodologies overcoming the microscopic distraction phenomenon, linking macroscopic control actions to microscopic, deployable control inputs.

We wish to highlight that continuification through mean-field provides a more general approach to perform the micro-to-macro step in spatial organization tasks. In particular, it ensures micro-to-macro convergence in the limit of an infinite number of agents, and although formally assuming microscopic all-to-all interactions, it can naturally approximate proximity nonlinear topologies via choosing interaction functions whose intensity decays with the distance (see for example, the Morse or Lennard-Jones potentials). In such a context, a lot of interest has been given to mean-field optimal control, although not explicitly accounting for the discretization step. Less effort has been made for developing macroscopic control solutions which are not based on the solution of optimization problems. For these reasons, in this Thesis, we focus on mean-field continuification to derive macroscopic descriptions, which we then use to derive control solutions that are not in the context of optimal control.

We further point out that the vast majority of the Literature (except for [26] and related works, and methods involving PdEs [71, 72]) does not explicitly account for the macro-to-micro step, hence not providing discretization tools for macroscopic control actions. This significantly limits the applicability of existing solutions in real-world applications. In this Thesis, we propose a simple novel discretization method based on spatial sampling.

We also carried out a Literature review on large-scale leader-follower solutions, accounting for scenarios in which control can only be exerted on a subset of agents in the complex system. In such a framework, Literature lacks analytical conditions to guide the control design process, for instance, what the right leaders-to-followers ratio could be, or what leaders' minimal sensing/actuation capabilities are required to achieve control.

Finally, we discussed related work on the experimental testing of control solutions for large-scale systems. Within this context, we highlighted the emerging and promising field of virtual/mixed reality to create hybrid experimental platforms. Within the context of swarm robotics problems, such platforms can leverage real robots and virtual ones, to deal with the increasing resources demand and cost of full-scale experiments.

In the next Chapter we introduce our continuification control framework. Such a mathematical set-up is developed in the context of a density control task for a large group of nonlinear agents. In order to tackle this problem, we derive a continuum description of the system dynamics in terms of a PDE, which we then use to perform our macroscopic control design. Such a continuum action can be proven to ensure convergence towards the desired behavior. This action is ultimately discretized following the paradigm that is depicted in Fig. 2.2.

# 3 Continuification Control of Large-Scale Multi-Agent Systems

In this Chapter, we discuss the continuification based control framework we developed in [29, 31]. Specifically, we propose a method to tackle multi-scale control problems involving large-scale multi-agent systems swarming in a periodic domains of arbitrary size. In particular, we use a continuification-based approach (see Fig. 2.2 for a schematic) that transforms the microscopic, agent-level description of the system dynamics into a macroscopic, continuum-level representation, which we employ to synthesize a control action towards a desired distribution of the agents. The continuum-level control action is then discretized at the agent-level in order to practically implement it. To confirm the effectiveness of the proposed approach, we complement theoretical derivations with numerical simulations.

## 3.1 Introduction

A pressing open challenge in control theory is to find methods to steer the collective behavior of large-scale multiagent systems consisting of many dynamical units (or agents) interacting with a given, and possibly time-varying, network topology. Examples of this problem include multirobot systems [22, 43, 44], cell populations, [45, 46], and human networks [10, 47]. Typically, in these applications, the goal is to control some macroscopic observables of the emerging collective behavior. However, control needs to be practically exerted at the microscopic, individual agent-level. Developing methods that translate macroscopic-level control goals into microscopic-level control actions is a critical challenge [153].

In Statistical Physics [27, 28], mean-field approaches are often used to describe large-scale systems. Through a mean-field approximation, one can obtain a macroscopic description of the emergent behavior of the system in terms of appropriate distributed parameter models, derived from the microscopic ODEs models describing the agents' dynamics. Such mean-field approaches have been used to control the collective behavior of multiagent systems [86, 154, 155, 156]. Also, in Applied Mathematics, problems related to the control of crowds, herding, and flocking agents were solved by finding a mean-field description of the agents of interest [60, 86]. Macroscopic descriptions were also used in some multiagent reinforcement learning scenarios [157, 158]. Other methodologies recently proposed in the literature are based on the use of *graphons* [95] and data and manifold learning [159, 160]. For a more detailed discussion about methods for lifting complex systems from microscopic to macroscopic descriptions, we refer the reader to Section 2.2 of this Thesis.

Inspired by the paradigm proposed in [26], here we adopt a *continuification* approach in which a macroscopic model, derived from the agents' dynamics, is used to design a control strategy at the macroscopic level. Such a macroscopic control action is then discretized in order to be deployed on the agents at the microscopic level – see Fig. 2.2 for a schematic of the proposed control solution. As a representative case of study, we address the problem of steering the dynamics of a group of interacting agents on a periodic domain. Our goal is to control the agents so that they achieve some desired configuration, independently of their interactions (repulsive, attractive, etc.) and their initial configuration. Such a problem has important ramifications in traffic dynamics [161, 162], swarming robots [154], and natural systems, including animals' collective motion [53, 64, 127, 163, 164, 165], and cell populations [46].

After presenting the microscopic description of the agents' behavior, we derive a macroscopic, PDE model for their emergent behavior and we solve the problem of designing a control strategy to achieve a desired agents' configuration. We propose a mathematical proof of convergence at the macroscopic level, and then we discretize the control action to obtain the required control inputs acting on the individual agents. In contrast with [26], the microscopic control inputs are obtained by spatially sampling the macroscopic control action at the agents' positions. Theoretical derivations are complemented by numerical simulations validating the effectiveness and robustness of the proposed strategy.

This Chapter is organized as follows. In Section 3.2 we present the microscopic model of interest; then, in Section 3.3 and 3.4, we give the problem statement and our solution exploiting continuification; finally, numerical results are presented and discussed in Section 3.5, and conclusions are drawn in Section 3.6.

## 3.2 The model

We consider $N$ dynamical systems moving in the periodic cube $\Omega$ ($d = 1, 2, 3$) (see Def. 1.1). The agents' dynamics is modeled using the *kinematic assumption* [53, 166] (i.e., neglecting acceleration and considering a drag force proportional to the velocity) and assuming agents are not subject to any non-holonomic constraint. Specifically, we set

$$\dot{\mathbf{x}}_i = \sum_{k=1}^{N} \mathbf{f}\left(\{\mathbf{x}_i, \mathbf{x}_k\}\right) + \mathbf{u}_i, \quad i = 1, \dots, N, \tag{3.1}$$

where $\mathbf{x}_i \in \Omega$ is the $i$-th agent's position, and $\{\mathbf{x}_i, \mathbf{x}_k\}$ is the relative position between agent $i$ and $k$, wrapped to have values in $\Omega$, $\mathbf{f} : \Omega \to \mathbb{R}^d$ is a periodic velocity interaction kernel modeling pairwise interactions between the agents, and $\mathbf{u}_i$ is a velocity control input designed as to fulfill some control problem. Furthermore, we assume $\mathbf{f}(\mathbf{z}) = -\nabla F(\mathbf{z})$, where $F : \mathbb{R}^d \to \mathbb{R}$ is a *soft-core* potential, meaning that $\mathbf{f}(\mathbf{0}) = \mathbf{0}$. The Morse potential, vastly used in the literature [53, 167], is a choice of this kind. We remark that, in the absence of control, agents subject to a repulsive kernel will spread in $\Omega$ until reaching an equilibrium configuration. Agents subject to a Morse-like kernel (long-range attraction and short-range repulsion), will reach an aggregated compact formation (see [53] for a comprehensive description of the uncontrolled problem with 1D examples).

Assuming the number of agents $N$ is sufficiently large, we describe the system's collective behavior in terms of the spatio-temporal evolution of the swarm's density. Hence, we define the density at time $t$ as the scalar function $\rho : \Omega \times \mathbb{R}_{\geq 0} \to \mathbb{R}_{\geq 0}$, such that $\int_\Omega \rho(\mathbf{x}, t)\, \mathrm{d}\mathbf{x} = N$ and the integral over a subset of $\Omega$ returns the number of agents in it.

## 3.3 Problem statement

The problem is to select a set of distributed control inputs $\mathbf{u}_i$ acting at the microscopic, agent-level allowing the agents to organize themselves into a desired macroscopic configuration on $\Omega$. Specifically, given some desired periodic smooth density profile, $\rho^{\mathrm{d}}(\mathbf{x}, t)$, associated with the target agents' configuration, the problem can be reformulated as that of finding a set of distributed control inputs $\mathbf{u}_i,\ i = 1, 2, \dots, N$ in (3.1) such that

$$\lim_{t\to\infty} \|\rho^{\mathrm{d}}(\cdot, t) - \rho(\cdot, t)\|_2 = 0, \tag{3.2}$$

for agents starting from any initial configuration $\mathbf{x}_i(0) = \mathbf{x}_{i0},\ i = 1, 2, \dots, N$.

## 3.4 Control design

We describe next how each of the steps depicted in Fig. 2.2 can be implemented to solve the problem of interest.

### 3.4.1 Continuification

In the limit case of an infinite number of agents, we recast the microscopic dynamics of the agents (3.1) as the mass balance equation (see Sec. 2.2.1 for more details about the micro-to-macro lifting)

$$\rho_t(\mathbf{x}, t) + \nabla \cdot [\rho(\mathbf{x}, t)\mathbf{V}(\mathbf{x}, t)] = q(\mathbf{x}, t), \tag{3.3}$$

where

$$\mathbf{V}(\mathbf{x}, t) = \int_\Omega \mathbf{f}\left(\{\mathbf{x}, \mathbf{z}\}\right) \rho(\mathbf{z}, t)\, \mathrm{d}\mathbf{z} = (\mathbf{f} * \rho)(\mathbf{x}, t). \tag{3.4}$$

represents the characteristic velocity field encapsulating the interactions between the agents in the continuum. The scalar function $q$, represents the macroscopic control action. It is written as a mass source/sink for simplifying derivations, but it will be, in the end, recast as an additional velocity field, in accordance to the microscopic dynamics (3.1).

For (3.3) to be well posed, we require the periodicity of $\rho(\mathbf{x}, t)$ on $\partial\Omega\ \forall t \in \mathbb{R}_{\geq 0}$ and that $\rho(\mathbf{x}, 0) = \rho_0(\mathbf{x})$. We remark that $\mathbf{V}$ is periodic by construction, as it comes from a circular convolution. Thus, the periodicity of the density is enough to ensure mass is conserved when $q = 0$, i.e., $\left(\int_\Omega \rho(\mathbf{x}, t)\, \mathrm{d}\mathbf{x}\right)_t = 0$ (using the divergence theorem and exploiting the periodicity of the flux).

**Remark 3.1.** *We do not assume the agents' dynamics to be linear and interactions to take place on a spatially-invariant lattice as done in [26], where some useful heuristics extensions to nonlinear systems and different topologies are presented.*

### 3.4.2 Macroscopic control design

We assume the desired density profile obeys the mass conservation law

$$\rho_t^{\mathrm{d}}(\mathbf{x},t) + \nabla \cdot \left[\rho^{\mathrm{d}}(\mathbf{x},t)\mathbf{V}^{\mathrm{d}}(\mathbf{x},t)\right] = 0, \tag{3.5}$$

where

$$\mathbf{V}^{\mathrm{d}}(\mathbf{x},t) = \int_{\Omega} \mathbf{f}\left(\{\mathbf{x},\mathbf{z}\}\right)\rho^{\mathrm{d}}(\mathbf{z},t)\,\mathrm{d}\mathbf{z} = (\mathbf{f} * \rho^{\mathrm{d}})(\mathbf{x},t). \tag{3.6}$$

Periodic boundary conditions and initial condition for (3.5) are set similarly to those of (3.3). Furthermore, we define the error function $e(\mathbf{x},t) := \rho^{\mathrm{d}}(\mathbf{x},t) - \rho(\mathbf{x},t)$.

**Theorem 3.1** (Macroscopic convergence)**.** *Choosing*

$$q(\mathbf{x},t) = K_{\mathrm{p}} e(\mathbf{x},t) - \nabla \cdot \left[e(\mathbf{x},t)\mathbf{V}^{\mathrm{d}}(\mathbf{x},t)\right] - \nabla \cdot \left[\rho(\mathbf{x},t)\mathbf{V}^{\mathrm{e}}(\mathbf{x},t)\right], \tag{3.7}$$

*where $K_{\mathrm{p}}$ is a positive control gain and $\mathbf{V}^{\mathrm{e}}(\mathbf{x},t) = (\mathbf{f} * e)(\mathbf{x},t)$, the error dynamics globally exponentially converges to 0*

$$e(\mathbf{x},t) = e(\mathbf{x},0)\exp\{-K_{\mathrm{p}}t\} \tag{3.8}$$

*Proof.* We can compute the error dynamics by subtracting (3.3) from (3.5), resulting in

$$e_t(\mathbf{x},t) + \nabla \cdot \left[\rho^{\mathrm{d}}(\mathbf{x},t)\mathbf{V}^{\mathrm{d}}(\mathbf{x},t)\right] - \nabla \cdot \left[\rho(\mathbf{x},t)\mathbf{V}(\mathbf{x},t)\right] = -q(\mathbf{x},t). \tag{3.9}$$

The error function $e(\mathbf{x},t)$ is periodic on $\partial\Omega$ $\forall t \in \mathbb{R}_{\geq 0}$ and $e(\mathbf{x},0) = \rho^{\mathrm{d}}(\mathbf{x},0) - \rho(\mathbf{x},0)$. Then, taking into account that $\rho = \rho^{\mathrm{d}} - e$, and $\mathbf{V} = \mathbf{V}^{\mathrm{d}} - \mathbf{V}^{\mathrm{e}}$, we rewrite (3.9) as

$$e_t(\mathbf{x},t) + \nabla \cdot \left[e(\mathbf{x},t)\mathbf{V}^{\mathrm{d}}(\mathbf{x},t)\right] + \nabla \cdot \left[\rho(\mathbf{x},t)\mathbf{V}^{\mathrm{e}}(\mathbf{x},t)\right] = -q(\mathbf{x},t). \tag{3.10}$$

Plugging in (3.7), we get

$$e_t(\mathbf{x},t) = -K_{\mathrm{p}} e(\mathbf{x},t), \tag{3.11}$$

whose analytical solution lets (3.8) holds. ■

**Remark 3.2.** *The control action $q$ transforms the error dynamics in the form in (3.11) via appropriate cancellations of the macroscopic system dynamics. Moreover, $q$ is characterized by the non-local term $\mathbf{V}^{\mathrm{e}}$, whose definition involves the convolution with the* *interaction kernel* $\mathbf{f}$ *and the error* $e$*. The presence of such a term implies that the control action exerted at the position* $\mathbf{x}$ *depends on the error everywhere else in the domain, implicitly pointing at the necessities for unlimited sensing capabilities for the agents. This non-locality is practically smoothed by the vanishing nature of the interaction kernel, and robustness with respect to limited sensing capabilities is considered in Chapter 4.*

### 3.4.3 Discretization and microscopic control

In order to discretize the macroscopic control action $q$, we first recast the macroscopic controlled model as

$$\rho_t(\mathbf{x},t) + \nabla \cdot [\rho(\mathbf{x},t)\,(\mathbf{V}(\mathbf{x},t) + \mathbf{U}(\mathbf{x},t))] = 0, \tag{3.12}$$

where $\mathbf{U}$ is a controlled velocity field, in which we want to incorporate the control action. Equation (3.12) is equivalent to (3.3), if

$$\nabla \cdot [\rho(\mathbf{x},t)\mathbf{U}(\mathbf{x},t)] = -q(\mathbf{x},t). \tag{3.13}$$

When $d = 1$, this relation simplifies to $(\rho U)_x = -q$ ($U$ being the one dimensional version of $\mathbf{U}$), which can be spatially integrated to recover $U$. When $d > 1$, equation (3.13) is insufficient to uniquely determine $\mathbf{U}$ from $q$ since it represents only a scalar relationship (as the divergence returns a scalar function). Hence, we define the flux $\mathbf{w}(\mathbf{x},t) := \rho(\mathbf{x},t)\mathbf{U}(\mathbf{x},t)$, and close the problem by adding an extra differential constraint on the curl of $\mathbf{w}$. Namely, we consider the set of equations

$$\begin{cases} \nabla \cdot \mathbf{w}(\mathbf{x},t) = -q(\mathbf{x},t) \\ \nabla \times \mathbf{w}(\mathbf{x},t) = 0 \end{cases} \tag{3.14}$$

For problem (3.14) to be well posed, we require $\mathbf{w}(\mathbf{x},t)$ to be periodic on $\partial\Omega$. Notice that (3.14) is a purely spatial problem, as no time derivatives are involved. We also remark that the choice of closing the problem using the irrotationality condition is arbitrary, and other closures can be considered. This specific one allows not to introduce vorticity into the velocity field we are looking for. Since $\Omega$ is simply connected, and $\nabla \times \mathbf{w} = 0$, we can express $\mathbf{w}$ using the scalar potential $\varphi$. Specifically, we pose $\mathbf{w}(\mathbf{x},t) = -\nabla\varphi(\mathbf{x},t)$, making the zero-curl condition always fulfilled. Then, substituting this into the divergence relation in (3.14), we can recast (3.14) as the Poisson equation

$$\nabla^2 \varphi(\mathbf{x}, t) = q(\mathbf{x}, t). \tag{3.15}$$

Problem (3.15) is characterized by the periodicity of $\nabla\varphi(\mathbf{x}, t)$ on $\partial\Omega$. We wish to remark the analogy with the derivation of the Poisson equation in the context of the electrostatic field [42]. Equation (3.15), together with its boundary conditions, defines $\varphi$ up to a constant $C$. Since we are interested in computing $\mathbf{w} = -\nabla\varphi$, the value of $C$ is irrelevant. We solve the Poisson problem (3.15) in $\Omega$ using Fourier series expansion. Then, writing the Fourier series of $\varphi$ in $\Omega$, we get

$$\varphi(\mathbf{x}) = \sum_{\mathbb{m}\in\mathbb{Z}^d} \gamma_{\mathbb{m}}\, \mathrm{e}^{j\mathbf{m}\cdot\mathbf{x}} + C, \tag{3.16}$$

where $\mathbb{m}$ is a multi-index, $\mathbf{m}$ is the row vector associated to this multi-index, $\gamma_{\mathbf{m}}$ is the $\mathbb{m}$-th Fourier coefficient, $j$ is the imaginary unit, and $\mathbf{x}$ is assumed to be a column. Given this expression for the potential, we write its Laplacian as

$$\nabla^2 \varphi(\mathbf{x}) = \sum_{\mathbb{m}\in\mathbb{Z}^d} \gamma_{\mathbb{m}} \|\mathbf{m}\|_2^2 \mathrm{e}^{j\mathbf{m}\cdot\mathbf{x}}. \tag{3.17}$$

Next, we can apply Fourier series to the known function $q$, resulting in

$$q(\mathbf{x}) = \sum_{\mathbb{m}\in\mathbb{Z}^d} c_{\mathbb{m}}\, \mathrm{e}^{j\mathbf{m}\cdot\mathbf{x}}, \tag{3.18}$$

where, since at time $t$ the function $q$ is known, we can also express the coefficients as

$$c_{\mathbb{m}} = \frac{1}{(2\pi)^d} \int_{\Omega} q(\mathbf{x}) \mathrm{e}^{-j\mathbf{m}\cdot\mathbf{x}}\, \mathrm{d}\mathbf{x}. \tag{3.19}$$

Then, recalling (3.15), we can express the coefficients of the Fourier series of the potential $\varphi$ as

$$\gamma_{\mathbb{m}} = -\frac{c_{\mathbb{m}}}{\|\mathbf{m}\|^2}. \tag{3.20}$$

Hence $\mathbf{w} = -\nabla\varphi$ and, consequently, $\mathbf{U} = \mathbf{w}/\rho$. Such derivations need to take place at each $t$. From the implementation viewpoint, when computing $\varphi$, and consequently $\mathbf{w}$, we approximate it only considering the first $M$ (with $M$ sufficiently large) terms of the infinite summations in (3.16).

Then, we can compute the microscopic control inputs for the discrete set of agents by spatially sampling $\mathbf{U}(\mathbf{x}, t)$, that is

$$\mathbf{u}_i(t) = \mathbf{U}(\mathbf{x}_i, t), \quad i = 1, 2, \ldots, N. \tag{3.21}$$

Notice that our discretization procedure is different from the one that is proposed in [26].

**Remark 3.3.** *The macroscopic control action $q$ is based on non-local terms like $\mathbf{V}^{\mathrm{d}}$ and $\mathbf{V}^{\mathrm{e}}$, making the control action exerted at $\mathbf{x}$ depending on the error everywhere else in $\Omega$. The input $\mathbf{u}_i$ can be approximated in terms of local information, since the assumption of unlimited sensing is practically mitigated by assuming a vanishing interaction kernel. We refer to Chapter 4 for analytical results about stability with limited sensing.*

**Remark 3.4.** *The macroscopic velocity field $\mathbf{U}$ is well-defined only when $\rho \neq 0$. This is indeed a fair assumption, as finally we will estimate the density by the agents position with an estimation kernel of our choice. Moreover, as $\mathbf{U}$ will be sampled at the agents locations, i.e. where the density is different from 0, we know $\mathbf{U}$ is well defined where it is needed.*

## 3.5 Numerical validation

In this Section we perform the numerical validation of the proposed control methodology. We consider two possible scenarios: the case that agents move on the ring ($d = 1$), and the case that agents move on the periodic square ($d = 2$). In both scenarios, we consider agents to start from a constant density profile, that is $\rho(\mathbf{x}, 0) = N/(2\pi)^d$.

For each simulation trial, we consider two different set-ups. First, we consider a continuum framework, consisting of the numerical integration of (3.12) (see Appendix D for more details about the numerical integration), thus letting the hypothesis of an infinite number of agents hold. Notice that, in this case, the discretization procedure described in Section 3.4.3 is not needed. Then, we consider the discrete scenario, where problem (3.1) is numerically integrated. In this discrete framework, we discretize the spatial domain into $n$ grid points. Agents are not constrained to move on such grid points, so that we use a linear interpolation of $\mathbf{U}$ when computing $\mathbf{u}_i$. For estimating densities from the agents' positions, we use a Gaussian *msn* (minimum of standard deviation and interquantile range) kernel estimation, adapted to the circular domain, as in [168]. Looking at both the continuum and discrete case allows to understand how using the continuum hypothesis for the control design perform when finally considering finite size swarms.

The performance of each trial is assessed in terms of the percentage error

$$\bar{E}(t) = \frac{\|e(\cdot,t)\|_2^2}{\max_t \|e(\cdot,t)\|_2^2} 100. \tag{3.22}$$

The value of $\bar{E}$ at the end of the trial is the remaining percentage $\mathcal{L}^2$ error. Trials are also characterized using the Kullback-Leibler (KL) divergence or relative entropy [169], as often done for density control problems [170]. Specifically, we consider the KL divergence between the desired and effective density of the swarm (re-normalized to sum to 1). Given, $\hat{\rho}$ and $\hat{\rho}^{\mathrm{d}}$, that are analogous to the actual and desired density but normalized to 1, the KL divergence is defined as

$$D_{\mathrm{KL}}(t) = \int_{\Omega} \hat{\rho}^{\mathrm{d}}(\mathbf{x},t) \log\left(\frac{\hat{\rho}^{\mathrm{d}}(\mathbf{x},t)}{\hat{\rho}(\mathbf{x},t)}\right) \mathrm{d}\mathbf{x}. \tag{3.23}$$

This is a non-negative quantity with the case $D_{\mathrm{KL}} = 0$ meaning that the information embedded in both the densities is identical.

### 3.5.1 Simulations on the ring

We consider a group of $N = 100$ agents interacting on the ring through a periodic repulsive interaction kernel

$$f(z) = \frac{\operatorname{sgn}(z)}{\mathrm{e}^{\frac{2\pi}{L}} - 1}\left[\mathrm{e}^{\frac{2\pi - |z|}{L}} - \mathrm{e}^{\frac{|z|}{L}}\right], \tag{3.24}$$

where $L$ is the characteristic length scale[1]. For all the simulation trials we consider $L = 1$. We also fix $K_{\mathrm{p}} = 10$.

As desired density we consider the von Mises distribution

$$\rho^{\mathrm{d}}(x,t) = \frac{N \mathrm{e}^{k\cos(x-\mu(t))}}{2\pi I_0(k)}, \tag{3.25}$$

where $\mu$ is the mean, $k$ is the concentration coefficient, $N$ is used to let the desired density sum to the total number of agents and $I_0$ is the modified Bessel function of the first kind of order 0 [171].

---

[1] This periodic kernel can be derived via periodization of the non-periodic repulsive kernel $\hat{f}(z) = \operatorname{sgn}(z)\mathrm{e}^{-\frac{|z|}{L}}$ (see Appendix A for more details).

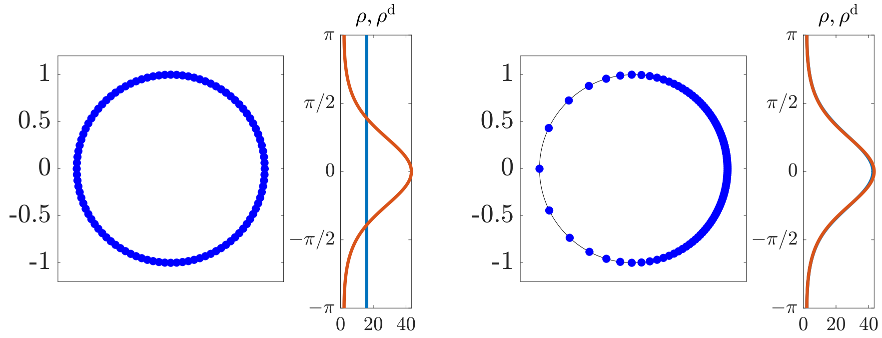

(a) $t = 0$

(b) $t = 2$

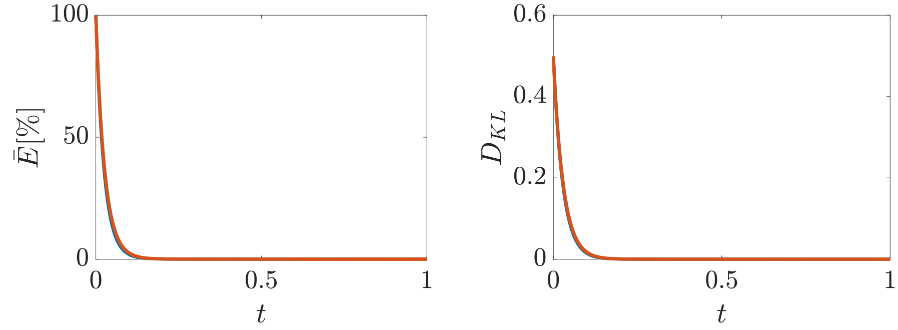

(c)

(d)

Figure 3.1: Monomodal regulation ($d = 1$): (a-b) initial and final configuration of the swarm (on the left, agents' displacement; on the right, estimated density in blue and desired density in orange); (c) time evolution of the percentage error (blue for the continuum trial, orange for the discrete one); (d) time evolution of the KL divergence (blue for the continuum trial, orange for the discrete one).

**Monomodal regulation** As a first simulation trial, we consider a rendez-vous problem, where agents need to meet and stay at a fixed location in the domain. This consists of fixing the desired density to be that in (3.25) with $\mu = 0$ and $k = 1.5$. Results of this trial, are reported in Fig. 3.1. In particular, the initial and final swarm's configuration are reported in Fig. 3.1a and 3.1b, both in terms of agents' displacement in $\mathcal{S}$ and estimated density. The performance of the trial is reported in Fig. 3.1d and 3.1c, showing both the percentage error and KL divergence are brought to 0, in the continuum (blue line) and discretized (orange line) framework. For this specific case, it is impossible to catch any difference between the continuum and discrete framework, highlighting the suitability of the continuum hypothesis.

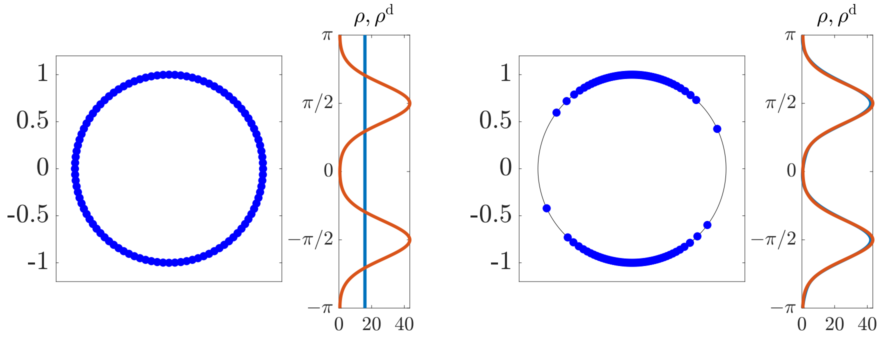

(a) $t = 0$ (b) $t = 2$

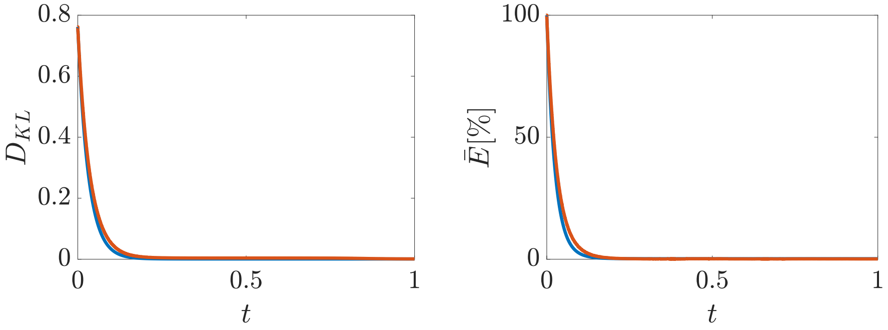

(c) (d)

Figure 3.2: Multimodal regulation ($d = 1$): (a-b) initial and final configuration of the swarm (on the left, agents' displacement; on the right, estimated density in blue and desired density in orange); (c) time evolution of the percentage error (blue for the continuum trial, orange for the discrete one); (d) time evolution of the KL divergence (blue for the continuum trial, orange for the discrete one).

**Multimodal regulation** Still in the vein of a rendez-vous problem, we consider a bimodal regulation task, consisting tasking agents to meet at two different locations in $\mathcal{S}$. We fix the desired density to be the composition of two von Mises distributions as (3.25), the first one characterized by $\mu_1 = -\pi/2$ and $k_1 = 5$, the second one by $\mu_2 = \pi/2$ and $k_2 = 5$.

Results of this trial, are reported in Fig. 3.2. In particular, the initial and final swarm's configuration are reported in Fig. 3.2a and 3.2b, both in terms of agents' displacement in $\mathcal{S}$ and estimated density. The performance of the trial is reported in Fig. 3.2d and 3.2c, showing both the percentage error and KL divergence are brought to 0. For this numerical trial, we observe that in the discrete scenario, convergence is achieved slower

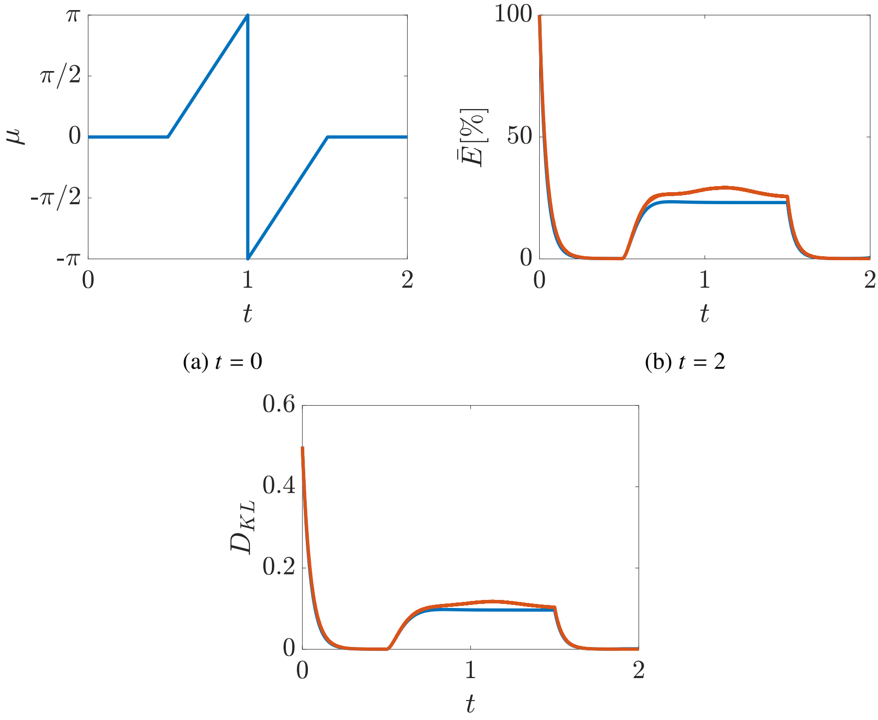

(a) $t = 0$

(b) $t = 2$

(c)

Figure 3.3: Monomodal tracking ($d = 1$): (a) time evolution of $\mu$; (b) time evolution of the percentage error (blue for the continuum trial, orange for the discrete one); (c) time evolution of the KL divergence (blue for the continuum trial, orange for the discrete one).

than in the continuum case.

**Monomodal tracking** Here we consider a macroscopic version of a formation control problem. In particular, we fix the desired density to be that in (3.25), with $k = 1.5$ and a time varying mean $\mu$, whose time evolution is reported in Fig. 3.3a. In particular, it is fixed to 0 for the first quarter of the trial, then it linearly increase in time, to finally settle about 0.

The performance of the trial is characterized in Fig. 3.3b and 3.3c, both in terms of percentage error and KL divergence. We remark that, although at the end of the trial it is impossible to spot differences between the continuum and the discrete case, during the transient, we observe a degradation in the performance for the discrete set-up.

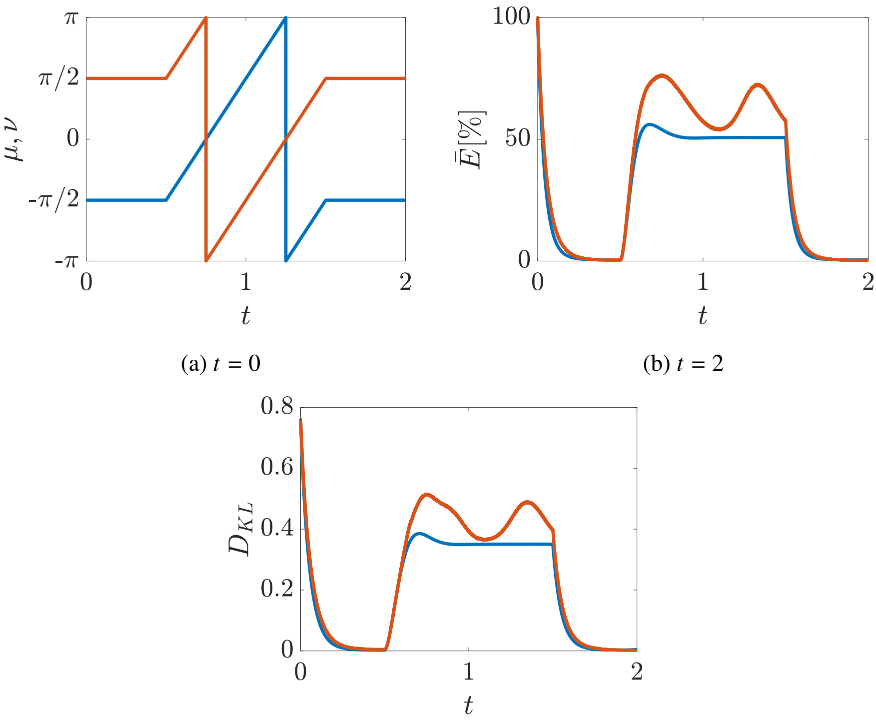

(a) $t = 0$

(b) $t = 2$

(c)

Figure 3.4: Multimodal tracking ($d = 1$): (a) time evolution of $\mu$; (b) time evolution of the percentage error (blue for the continuum trial, orange for the discrete one); (c) time evolution of the KL divergence (blue for the continuum trial, orange for the discrete one).

**Multimodal tracking** Finally we consider a multimodal tracking problem, consisting in fixing the desired density as the combination of two time-varying von Mises distributions as (3.25). Specifically, we fix the concentration coefficients of the two distributions to be $k_1 = k_2 = 5$, while we choose their means, namely $\mu$ and $\nu$, to behave as in Fig. 3.4a. This means the two modes start centered at $-\pi/2$ and $\pi/2$, and then start orbiting at fixed velocity on $\mathcal{S}$ until they go back to their initial location.

Results of this trial are reported in Fig. 3.4 and they are qualitatively similar to those of the monomodal tracking case. In particular, convergence is achieved both in the continuum and discrete case, but the transient performance and convergence time are better in the continuum framework.

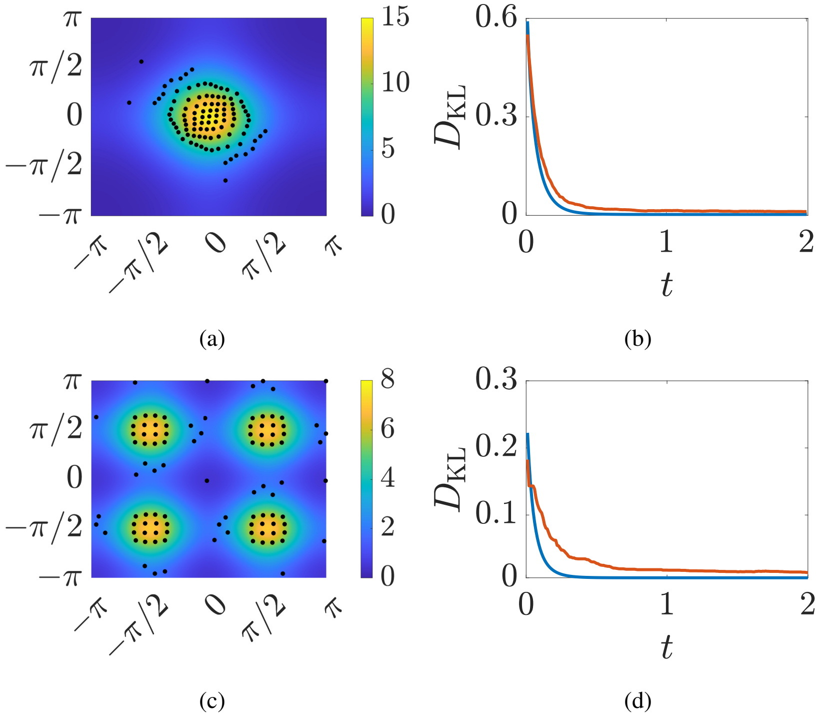

(a) (b)

(c) (d)

Figure 3.5: Monomodal and multimodal regulation ($d = 2$): (a, c) Final displacement of the swarm against the desired density; (b, d) time evolution of the KL divergence for the continuum (blue line) and discrete (orange line) set-up.

### 3.5.2 Simulation on the periodic square

In this section we consider agents move on the periodic square, that is $\Omega = [-\pi, \pi]^2$. We assume a group of 100 agents, whose interaction are governed by a repulsive kernel with characteristic length scale $L = 1$. Notice that, contrary to the one dimensional case, a closed form of the periodic repulsive kernel was not found[2], so that it needs to be approximated as described in Appendix A.

As for the desired density to achieve, we choose the 2D von Mises function

$$\rho^{\mathrm{d}}(\mathbf{x}) = Z \exp\{\mathbf{k}^T \mathbf{c}_1(\mathbf{x}, \mu, \nu) + \mathbf{c}_2(\mathbf{x}, \mu, \mu)\, \mathbf{c}_2^T(\mathbf{x}, \nu, \nu)\} \tag{3.26}$$

---

[2] we tried to seek for the periodization of

$$\mathbf{f}(\mathbf{x}) = \begin{cases} \frac{\mathbf{x}}{\|\mathbf{x}\|} \mathrm{e}^{-\frac{\|\mathbf{x}\|}{L}} & \text{if } \|\mathbf{x}\| \neq 0 \\ 0 & \text{otherwise.} \end{cases}$$

where $\mathbf{k} = [k_1, k_2]^T$ is the vector of the concentration coefficients, $\mu$ and $\nu$ are the means along the two directions, $\mathbf{c_1}(\mathbf{x}, a, b) = [\cos(x_1 - a), \cos(x_2 - b)]$ and $\mathbf{c_2}(\mathbf{x}, a, b) = [\cos(x_1 - a), \sin(x_2 - b)]$ (with $a, b \in \Omega$), where $x_1$ and $x_2$ are the components of $\mathbf{x}$ in the Cartesian coordinate system. $Z$ is a normalization coefficient, to allow $\rho^{\mathrm{d}}$ to sum to the total number of agents $N$.

As for the one-dimensional numerical validation, we consider both the continuum and discrete framework underlying the problem of interest. Here, for brevity, trials are characterized using the KL divergence only.

**Monomodal regulation** For this trial we fix the desire density as (3.26) with $\mu = \nu = 0$ and $\kappa_1 = \kappa_2 = 1.5$, mimicking a two-dimensional rendez-vous task.

The final configuration of the group is displaced in Fig. 3.5a, while the time evolution of the KL divergence for the continuum (blue line) and discrete (orange line) framework is shown in Fig. 3.5b. While for the continuum case the KL divergence is brought to 0 in almost 1 time unit, we observe a steady-state mismatch for the discrete trial.

**Multimodal regulation** Here we choose desire density the combination of four distributions as that in (3.26). The concentration coefficients of all the modes is set to 2, and the mean values are $\mu_1 = \mu_2 = -\pi/2$, $\mu_3 = \mu_4 = \pi/2$, $\nu_1 = \nu_2 = \pi/2$, and $\nu_3 = \nu_4 = \pi/2$. This desired density consists of four clusters of agents symmetrically displaced around the origin. The final formation is reported in Fig. 3.5c, while the time evolution of the KL divergence is shown in Fig. 3.5d.

As for the monomodal regulation case, we report a steady-state mismatch between the continuum and discrete numerical trial.

**Monomodal tracking** We consider a monomodal tracking scenario, where the desired density is a 2D von Mises function, whose means are time varying, see (3.26). Specifically, we consider $\mu(t)$ and $\nu(t)$ behaving as in Fig. 3.6a, while the concentration coefficients are kept constant and equal to 1. Such a desired density is centered at the origin for $t \leq 1$. Then, it starts moving at constant velocity towards a side of the domain and then on the circle of radius $\pi/2$. We report the results of the trial in Fig. 3.6b, where the KL divergence in time is shown.

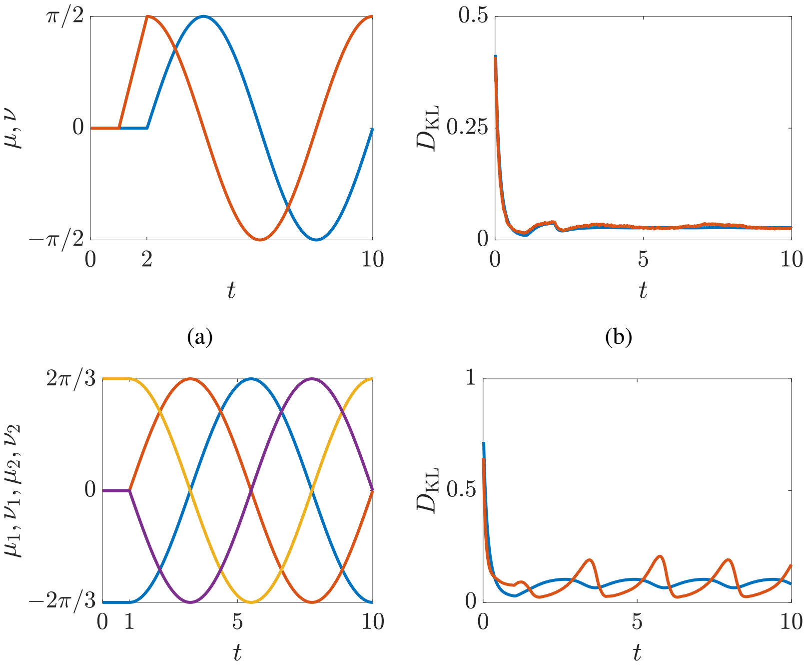

(a) (b)

(c) (d)

Figure 3.6: Tracking experiments. (a, c) Time evolution of the means of the monomodal and multimodal trial, (b, d) KL divergence in time during the monomodal and multimodal tracking trial (blue line for the continuum framework, orange line for the discrete one).

**Multimodal tracking** We consider a multimodal tracking case, where two von Mises functions with constant concentration coefficients of 2.2 orbitate on the circle of radius $2\pi/3$, after remaining still at two sides of the domain for $t \leq 1$. Specifically, $\mu_1(t)$, $\nu_1(t)$ and $\mu_2(t)$, $\nu_2(t)$, the means of the two von Mises functions, evolve as in Fig. 3.6c. Such a desired behavior consists of two clusters of agents orbitating on a circle. Results are reported in Fig. 3.6d, where the time evolution of the KL divergence is also shown.

### 3.5.3 Results

We performed an extensive numerical validation consisting of two main scenarios, the one-dimensional one where agents move on the ring, and the two-dimensional one where agents move on the periodic square. For each scenario, we considered four different experimental conditions, that are $(i)$ monomodal regulation, $(ii)$ multimodal regulation, $(iii)$ monomodal tracking, and $(iv)$ multimodal tracking. In each condition, we considered two different numerical set-ups: the continuum one, where the continuified problem is numerically integrated, so that the hypothesis of infinite agents holds; the discrete one, where swarms of finite size are considere.

In the continuum framework we are almost always able to fulfill the control problem, that is, we bring the error to 0 asymptotically. We only observe a degradation of the performance for tracking trials, where, the numerical diffusion introduced by our numerical integration scheme plays a more relevant role.

In the discrete framework, we consistently observe performance degradation, in the form of transient degradation, slower convergence, or a steady-state error (as, for example, the one depicted in two-dimensional regulation problems – see Fig. 3.5). This is due to the discretization process discussed in Section 3.4.3, which is indeed needed to cope with finite size swarms.

## 3.6 Discussion

We developed a continuification-based control strategy for a swarm of agents moving on a periodic bounded domain. We started by deriving a macroscopic model of agents' distribution and designed a control action able to steer it to a desired configuration, proving its convergence. The microscopic control strategy was then obtained by spatially sampling the macroscopic control function at the agents' positions. Numerical simulations confirmed the effectiveness and robustness of the proposed approach.

The approach does not come without limitations. In particular, convergence towards desired behaviors has been proved only at the macroscopic scale, that is in the limit of an infinite number of agents. How the macroscopic convergence maps into the microscopic dynamics is the subject of ongoing work. Also, a fully distributed and localized framework needs to be developed to reduce the gap with typical constraints of real applications.

In the next Chapter we analytically study the robustness properties of the continuification control solution that is discussed here. In particular, by using the continuum formulation of the problem, we derive stability guarantees when the system is pushed out of its nominal conditions. In particular, we consider agents being affected by limited sensing capabilities and the presence of structural perturbations.

# 4 Robustness Analysis of Continuification Control Methodologies

In this Chapter we discuss the results of [30, 32]. Specifically, we investigate the stability and robustness properties of the continuification-based strategy for the control of large-scale multiagent systems presented in Chapter 3. Within this framework, one transforms the microscopic, agent-level description of the system dynamics into a macroscopic continuum-level, for which a control action can be synthesized to steer the macroscopic dynamics towards a desired distribution. Such an action is ultimately discretized to obtain a set of deployable control inputs for the agents to achieve the goal. The mathematical proof of convergence toward the desired distribution typically relies on the assumptions that no disturbance is present and that each agent possesses global knowledge of all the others' positions. Here, we analytically and numerically address the possibility of relaxing these assumptions for the case of a system of agents moving in periodic domains. We offer compelling evidence in favor of the use of a continuification-based strategy when agents only possess a finite sensing capabilities and spatio-temporal perturbations affect the macroscopic dynamics of the ensemble.

## 4.1 Introduction

The key idea of continuification consists of three fundamental steps: (i) finding a macroscopic description (typically a partial differential equation, PDE) for the collective dynamics of the multiagent system of interest; (ii) designing a macroscopic control action to attain the desired collective response; (iii) discretize the macroscopic control action to obtain feasible control inputs for the agents at the microscopic level. See Fig. 2.2 for a sketch.

This methodology tackles problems in which the control goal is formulated at the macroscopic dynamics level, but control actions can be exerted only at the microscopic agent scale [153]. Applications of the approach are related, but not limited to, multi-robot systems [80, 125, 126, 172], cell populations [45, 46, 173], neuroscience [174, 175], and human networks [10, 11].

Such an approach was used in [29, 31] to control the distribution of a multiagent system swarming in a ring, leading to an effective control scheme for the multiagent system to achieve a desired distribution. Crucially, to prove convergence of the macroscopic collective dynamics towards the desired distribution, two key assumptions were made. Firstly, we assume that agents possess unlimited sensing capabilities so as to know the positions of all other agents in the swarm. Secondly, we assume that no disturbance or perturbation is affecting the dynamics.

Here we remove these often unrealistic assumptions and study the performance, stability, and robustness of the continuification approach in the presence of limited sensing capabilities or spatio-temporal disturbances. In particular, we prove that semiglobal asymptotic or bounded convergence can still be achieved under these circumstances. As we undertake this task, we offer insights into the role of the control parameters in changing the size and shape of the region of asymptotic stability of the desired distribution.

The rest of the Chapter is organized as follows. We introduce the robustness analysis we perform in Section 4.2. Such an analysis consists in the consideration of two different scenarios: limited sensing capabilities, which are discussed in Section 4.3, and perturbations, which are studied in Section 4.4. Each finding is complemented by numerical simulations on different domains.

## 4.2 Robustness analysis

We consider the model and problem statement described in Chapter 3. Specifically, we consider the dynamics in (3.1), and the density control problem in (3.2). Under the assumption of Theorem 3.1, we know that, in the limit of infinite agents, global convergence towards the desired density profile is achieved. In what follows, we relax the assumptions of agents possessing unlimited sensing and absence of perturbations to prove semi-global and bounded convergence can still be ensured.

## 4.3 Limited sensing capabilities

The macroscopic control law in (3.7) is based on the non-local convolution term $\mathbf{V}^{\mathrm{e}}$. For computing such a control action, agents need to know $e$ everywhere in $\Omega$, meaning that they need to possess sensing capabilities to cover the whole set $\Omega$.

Here, we relax this unrealistic assumption, considering agents only possess a limited sensing radius $\Delta$, i.e., they can only measure $e$ in a neighborhood of radius $\Delta$ located about their positions. We model such a case by considering a modified interaction kernel defined as

$$\hat{\mathbf{f}}(\mathbf{z}) = \begin{cases} \mathbf{f}(\mathbf{z}) & \text{if } \|\mathbf{z}\|_2 \leq \Delta \\ \mathbf{0} & \text{otherwise} \end{cases}. \tag{4.1}$$

In this scenario, the macroscopic control law takes the form

$$\hat{q}(\mathbf{x},t) = K_{\mathrm{p}} e(\mathbf{x},t) - \nabla \cdot \left[ e(\mathbf{x},t) \mathbf{V}^{\mathrm{d}}(\mathbf{x},t) \right] - \nabla \cdot \left[ \rho(\mathbf{x},t) \hat{\mathbf{V}}^{\mathrm{e}}(\mathbf{x},t) \right], \tag{4.2}$$

where $\hat{\mathbf{V}}^{\mathrm{e}} = (\hat{\mathbf{f}} * e)$. Under control action (4.2), the error system dynamics may be written as

$$e_t(\mathbf{x},t) = -K_{\mathrm{p}} e(\mathbf{x},t) + \nabla \cdot \left[ \rho^{\mathrm{d}}(\mathbf{x},t) \tilde{\mathbf{V}}(\mathbf{x},t) \right] - \nabla \cdot \left[ e(\mathbf{x},t) \tilde{\mathbf{V}}(\mathbf{x},t) \right], \tag{4.3}$$

where $\tilde{\mathbf{V}} = (\mathbf{g} * e)$ and $\mathbf{g} = \hat{\mathbf{f}} - \mathbf{f}$.

Now, we provide some lemmas, that will be used for studying the stability properties of the perturbed error system (4.3).

**Lemma 4.1.** *The following inequality holds:*

$$\|\nabla \cdot \tilde{\mathbf{V}}\|_\infty \leq \|e\|_2 \sum_{i=1}^{d} \|g_{i,x_i}\|_2,$$

*where $g_{i,x_i}$ is the derivative of the $i$-th component of* **g** *with respect to $x_i$.*

*Proof.* Expanding $\nabla \cdot \hat{\mathbf{V}}$ into its components (recalling the definition of convolution derivative in Section 1.6), and using the Minkowsky inequality (see Lemma 1.2), we can write

$$\|\nabla \cdot \tilde{\mathbf{V}}\|_\infty = \left\| \sum_{i=1}^{d} (g_{i,x_i} * e) \right\|_\infty \leq \sum_{i=1}^{d} \left\| (g_{i,x_i} * e) \right\|_\infty, \tag{4.4}$$

Using Young's convolution inequality, we construct the bound

$$\|\nabla \cdot \tilde{\mathbf{V}}\|_\infty \leq \|e\|_2 \sum_{i=1}^{d} \|g_{i,x_i}\|_2, \tag{4.5}$$

proving the lemma. ■

**Lemma 4.2.** *If $\nabla \rho^{\mathrm{d}} \in \mathcal{L}^2$, i.e. $\|\rho^{\mathrm{d}}_{x_i}\|_2 \leq M_i$, for some constants $M_i$ and $i = 1, 2, 3$, then*

$$\|e \nabla \rho^{\mathrm{d}} \cdot \hat{\mathbf{V}}\|_1 \leq \|e\|_2^2 \sum_{i=1}^{d} M_i \|g_i\|_2,$$

*where $g_i$ is the $i$-th component of* **g**.

*Proof.* By expanding $\nabla \rho^{\mathrm{d}} \cdot \hat{\mathbf{V}}$, we get

$$\|e \nabla \rho^{\mathrm{d}} \cdot \hat{\mathbf{V}}\|_1 = \left\| e \sum_{i=1}^{d} \rho^{\mathrm{d}}_{x_i} \tilde{V}_i \right\|_1 = \left\| e \sum_{i=1}^{d} \rho^{\mathrm{d}}_{x_i} (g_i * e) \right\|_1 . \tag{4.6}$$

Then, applying Minkowsky (see Lemma 1.2) and the Hölder (see Lemma 1.1) inequalities, we establish

$$\left\| e \sum_{i=1}^{d} \rho^{\mathrm{d}}_{x_i} (g_i * e) \right\|_1 \leq \sum_{i=1}^{d} \left\| e \rho^{\mathrm{d}}_{x_i} (g_i * e) \right\|_1 \leq \sum_{i=1}^{d} \|e\|_2 \|\rho^{\mathrm{d}}_{x_i}\|_2 \|(g_i * e)\|_\infty. \tag{4.7}$$

Finally, applying the Young's covolution inequality, we have

$$\sum_{i=1}^{d} \|e\|_2 \|\rho^{\mathrm{d}}_{x_i}\|_2 \|(g_i * e)\|_\infty \leq \sum_{i=1}^{d} \|e\|_2^2 \|\rho^{\mathrm{d}}_{x_i}\|_2 \|g_i\|_2, \tag{4.8}$$

which, thanks to the $\mathcal{L}^2$-boundedness of $\nabla\rho^{\mathrm{d}}$ is equivalent to

$$\sum_{i=1}^{d} \|e\|_2^2 \|\rho^{\mathrm{d}}_{x_i}\|_2 \|g_i\|_2 \leq \|e\|_2^2 \sum_{i=1}^{d} M_i \|g_i\|_2 \tag{4.9}$$

Comparing (4.6) and (4.9) yields the claim. ■

**Theorem 4.1** (Semi-global stability under limited sensing)**.** *If $\rho_{\mathrm{d}}$ and $\nabla\rho_{\mathrm{d}} \in \mathcal{L}^2$, control strategy* (4.2) *achieves semiglobal stabilization of error dynamics* (4.3)*, so that, for any initial condition in the compact set $\|e(\cdot,0)\| < \gamma$, choosing $K_{\mathrm{p}}$ sufficiently large ensures the error to converge asymptotically to 0.*

*Proof.* We choose $\|e\|_2^2$ as a candidate Lyapunov function. Then, taking into account (4.3), we write (omitting explicit dependencies for simplicity)

$$(\|e\|_2^2)_t = \int_\Omega 2ee_t \,\mathrm{d}\mathbf{x} = -2K_{\mathrm{p}}\|e\|_2^2 + 2\int_\Omega e\nabla\cdot(\rho^{\mathrm{d}}\tilde{\mathbf{V}})\,\mathrm{d}\mathbf{x} - 2\int_\Omega e\nabla\cdot(e\tilde{\mathbf{V}})\,\mathrm{d}\mathbf{x}. \tag{4.10}$$

This relation may be rewritten as

$$(\|e\|_2^2)_t = \int_\Omega 2ee_t \,\mathrm{d}\mathbf{x} = -2K_{\mathrm{p}}\|e\|_2^2 + 2\int_\Omega e\nabla\cdot(\rho^{\mathrm{d}}\tilde{\mathbf{V}})\,\mathrm{d}\mathbf{x} - \int_\Omega e^2\nabla\cdot\tilde{\mathbf{V}}\,\mathrm{d}\mathbf{x}, \tag{4.11}$$

where, applying Lemma 1.7, the divergence theorem, and Lemma 1.8, we establish

$$\begin{aligned}
2\int_\Omega e\nabla\cdot(e\tilde{\mathbf{V}})\,\mathrm{d}\mathbf{x} &= 2\int_\Omega \nabla\cdot(e^2\tilde{\mathbf{V}})\,\mathrm{d}\mathbf{x} - 2\int_\Omega \nabla e\cdot(e\tilde{\mathbf{V}})\,\mathrm{d}\mathbf{x} \\
&= 2\int_{\partial\Omega} e^2\tilde{\mathbf{V}}\cdot\hat{\mathbf{n}}\,\mathrm{d}\mathbf{x} - 2\int_\Omega \nabla e\cdot(e\tilde{\mathbf{V}})\,\mathrm{d}\mathbf{x} = -2\int_\Omega \nabla e\cdot(e\tilde{\mathbf{V}})\,\mathrm{d}\mathbf{x} \\
&= -\int_\Omega \nabla(e^2)\cdot\tilde{\mathbf{V}}\,\mathrm{d}\mathbf{x} = -\int_\Omega \nabla\cdot(e^2\tilde{\mathbf{V}})\,\mathrm{d}\mathbf{x} + \int_\Omega e^2\nabla\cdot\tilde{\mathbf{V}}\,\mathrm{d}\mathbf{x} \\
&= -\int_{\partial\Omega} e^2\tilde{\mathbf{V}}\cdot\hat{\mathbf{n}}\,\mathrm{d}\mathbf{x} + \int_\Omega e^2\nabla\cdot\tilde{\mathbf{V}}\,\mathrm{d}\mathbf{x} = \int_\Omega e^2\nabla\cdot\tilde{\mathbf{V}}\,\mathrm{d}\mathbf{x}.
\end{aligned} \tag{4.12}$$

We can provide bounds for the last two terms of (4.11), namely

$$\begin{aligned}\left|\int_{\Omega} e\nabla\cdot(\rho^{\mathrm{d}}\tilde{\mathbf{V}})\,\mathrm{d}\mathbf{x}\right| &\leq \int_{\Omega}\left|e\nabla\cdot(\rho^{\mathrm{d}}\tilde{\mathbf{V}})\right|\,\mathrm{d}\mathbf{x}\\ &= \|e\nabla\cdot(\rho^{\mathrm{d}}\tilde{\mathbf{V}})\|_1 = \|e\rho^{\mathrm{d}}\nabla\cdot\tilde{\mathbf{V}} + e\nabla\rho^{\mathrm{d}}\cdot\tilde{\mathbf{V}}\|_1 \leq\\ &\leq \|e\rho^{\mathrm{d}}\nabla\cdot\tilde{\mathbf{V}}\|_1 + \|e\nabla\rho^{\mathrm{d}}\cdot\tilde{\mathbf{V}}\|_1 \leq \|e\|_2\|\rho^{\mathrm{d}}\|_2\|\nabla\cdot\tilde{\mathbf{V}}\|_\infty\\ &+ \|e\|_2^2\sum_{i=1}^{d} M_i\|g_i\|_2 \leq \|e\|_2^2\left(\sum_{i=1}^{d} l\|g_{i,x_i}\|_2 + M_i\|g_i\|_2\right),\end{aligned} \tag{4.13}$$

$$\left|\int_{\Omega} e^2\nabla\cdot\tilde{\mathbf{V}}\,\mathrm{d}\mathbf{x}\right| \leq \int_{\Omega}\left|e^2\nabla\cdot\tilde{\mathbf{V}}\right|\,\mathrm{d}\mathbf{x} = \|e^2\nabla\cdot\tilde{\mathbf{V}}\|_1 \leq \|e\|_2^2\|\nabla\cdot\tilde{\mathbf{V}}\|_\infty \leq \|e\|_2^3\sum_{i=1}^{d}\|g_{i,x_i}\|_2, \tag{4.14}$$

where $l$ is a positive constant bounding $\|\rho^{\mathrm{d}}\|_2$, and we used Lemma 4.1 and 4.2, as well as the Hölder's inequality. Ultimately, we establish that

$$(\|e\|_2^2)_t \leq (-2K_{\mathrm{p}} + F + G\|e\|_2)\|e\|_2^2, \tag{4.15}$$

where

$$F = 2\sum_{i=1}^{d} l\|g_{i,x_i}\|_2 + M_i\|g_i\|_2, \tag{4.16}$$

$$G = \sum_{i=1}^{d}\|g_{i,x_i}\|_2. \tag{4.17}$$

Choosing $K_{\mathrm{p}} > (F + G\gamma)/2$, the error asymptotically converges to 0, as it ensures $\gamma$ is in the basin of attraction of the origin. ■

**Remark 4.1.** *Theorem 4.1 represents a semi-global stability result [41] (section 12.1). This means that, if an initial estimate of the error is available, the control parameters in the control action can be appropriately chosen to ensure convergence of the error to 0. The greater the initial error, the greater the control effort is needed to ensure convergence.*

**Remark 4.2.** *We remark that (i) as* $\Delta$ *becomes smaller,* $\|g\|_2$ *and* $\|g_{i,x_i}\|_2$ *increase, requiring a larger value of* $K_{\mathrm{p}}$ *to ensure convergence, and (ii) in the limit of local dynamics about the origin, where we neglect cubic terms in e, one can choose* $K_{\mathrm{p}} = F/2$.

**Remark 4.3.** *In [30], we explicitly study the case* $d = 1$*, which is included in Theorem*

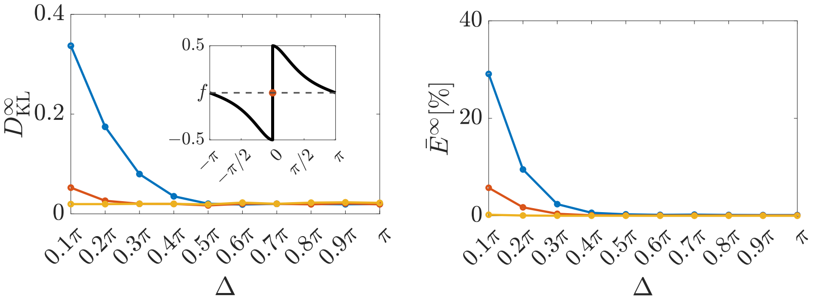

(a) (b)

Figure 4.1: Limited sensing ($d = 1$): steady-state value of (a) the KL divergence, $D_{\mathrm{KL}}^{\infty}$, and (b) percentage error, $\bar{E}^{\infty}$, at the end of a monomodal regulation trial, for different values of $\Delta$ and $K_{\mathrm{p}}$ ($K_{\mathrm{p}} = 10$ in blue, $K_{\mathrm{p}} = 100$ in orange and $K_{\mathrm{p}} = 1000$ in yellow). In the inset of the left panel, we show the repulsive interaction kernel  used in the simulations.

*4.1*.

**Numerical validation ($d = 1$)** We consider the same framework, control discretization and numerical set-up as in Section 3.5 of Chapter 3. In particular, we refer to a monomodal regulation scenario, where a repulsive swarm of $N = 100$ agents, starting evenly displaced in $\mathcal{S}$, is required to achieve a desired density profile given by a von Mises function, with mean $\mu = 0$ and concentration coefficient $k = 4$ – see (3.25). The pairwise interactions between agents are modeled via a repulsive kernel, depicted in the inset of Fig. 4.1a.

We run several trials of duration $t_{\mathrm{f}} = 6$. In each trial, we consider a different sensing radius $\Delta$, spanning from $0.1\pi$ to $\pi$. At the end of each trial, we record the steady-state Kullback-Leibler (KL) divergence , $D_{\mathrm{KL}}^{\infty} = D_{\mathrm{KL}}(t_{\mathrm{f}})$, between $\hat{\rho}$ and $\hat{\rho}^{\mathrm{d}}$ (equivalent to $\rho$ and $\rho^{\mathrm{d}}$, but normalized to sum to 1 – see (3.23) in Section 3.5), and the steady-state residual percentage error, $\bar{E}^{\infty} = \bar{E}(t_{\mathrm{f}})$ (see (3.22) in Section 3.5). The results of such a numerical investigation are reported in Fig. 4.1a, for different values of $K_{\mathrm{p}}$. They show that: (i) for large values of $K_{\mathrm{p}}$, performance is independent from the specific sensing radius that is given to the agents, and (ii) for smaller values of $K_{\mathrm{p}}$, a limited knowledge of the domain can still guarantee a performance level that is comparable to the case of $\Delta = \pi$. For example, when considering $K_{\mathrm{p}} = 10$, choosing $\Delta = 0.4\pi$ makes $D_{\mathrm{KL}}^{\infty}$ comparable to the value obtained for unlimited sensing capabilities. We also report in Fig. 4.2 the final configuration of the swarm for different values of the sensing radius, when $K_{\mathrm{p}} = 10$. We

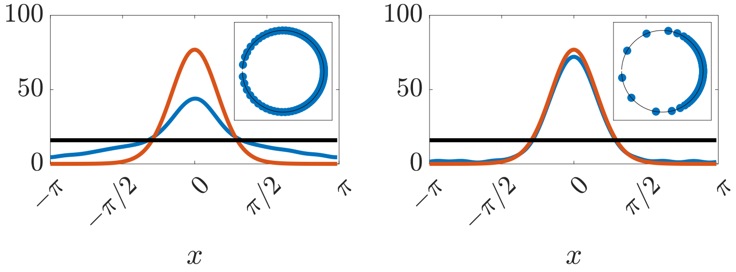

(a) $\Delta = 0.1\pi$ (b) $\Delta = 0.4\pi$

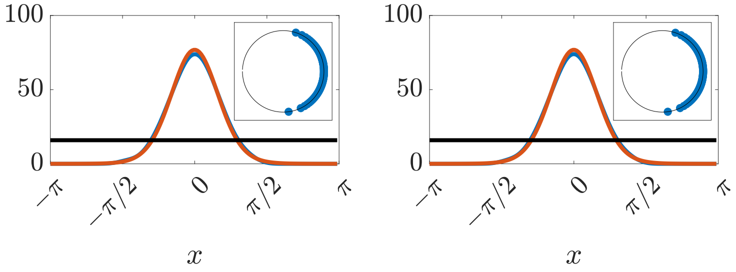

(c) $\Delta = 0.7\pi$ (d) $\Delta = \pi$

Figure 4.2: Steady-state ($t = t_{\mathrm{f}}$) comparison between the agents distribution (blue line) and the desired one (orange line) when the agents are started from the initial distribution shown as a black line, for increasing sensing abilities of the agents when $K_{\mathrm{p}} = 10$. Panel (d) shows the case when sensing is unlimited. In the inset of each panel, we display the discrete formation of the agents at the end of the trial.

remark that the non-zero $D^{\infty}_{\mathrm{KL}}$ comes from the discretization process, and it approaches 0 in the limit of an infinite number of agents.

**Numerical validation** ($d = 2$) We consider a sample of 100 agents starting from a constant density profile, and, we run both a discrete and a continuous simulation. This means we numerically integrate both (3.1) and its continuified version (3.3), allowing us to understand how well the continuum approximation holds. As a desired density, we consider the bivariate von Mises distribution in (3.26) with $\mu = \nu = 0$ and $k_1 = k_2 = 1.5$

To validate the stability result of Theorem 4.1, we fix $K_{\mathrm{p}} = 100$. When running a trial of 200 time steps, we obtain the results in Fig. 4.3a, 4.3b choosing $\Delta = 0.1\pi$ (i.e., agents have a sensing radius of 10% of the domain), and those in Fig. 4.3c, 4.3d with $\Delta = \pi$ (i.e., unlimited sensing). This choice of $K_{\mathrm{p}}$ ensures the performance is independent of the sensing capabilities of the agents. In the discrete trials, we observe a non-zero

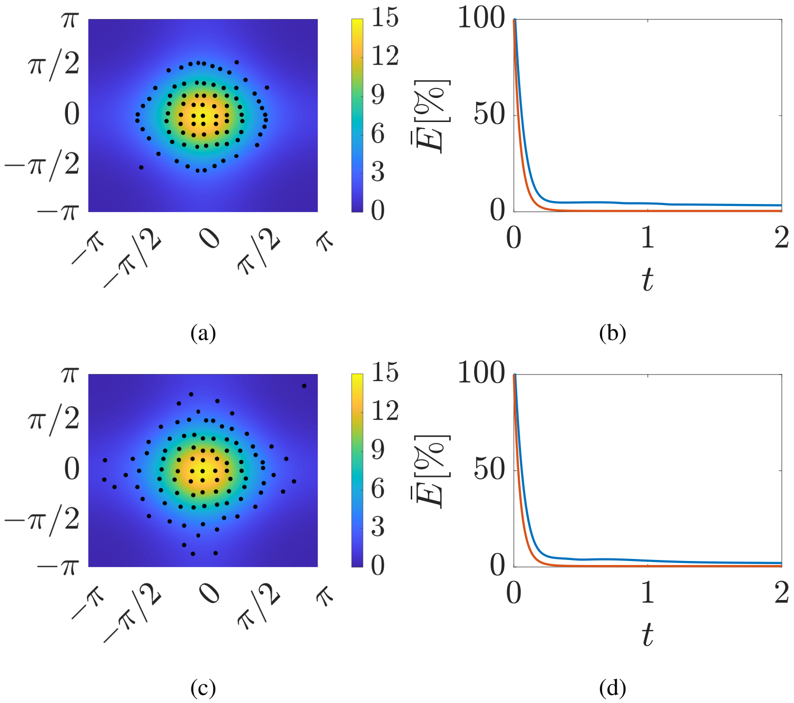

(a) (b)

(c) (d)

Figure 4.3: Robustness to limited sensing when $d = 2$ ($K_\mathrm{p} = 100$, (a, b) $\Delta = 0.1\pi$, (c, d) $\Delta = \pi$). (a, c) Final displacement of the system on top of the desired density; (b, d) time evolution of the percentage error for the discrete (blue) and continuous case (orange).

steady-state error. This is due to the finite-size effect of assuming a swarm of 100 agents. This residual error is slightly worse in the case of limited sensing.

## 4.4 Spatio-temporal perturbations of the velocity field

Next, we assess the robustness of the approach to perturbations acting additively on the macroscopic velocity field and the second on the interaction kernel.

We consider the modified problem

$$\rho_t(\mathbf{x},t) + \nabla \cdot [\rho(\mathbf{x},t)\,(\mathbf{V}(\mathbf{x},t) + \mathbf{W}(\mathbf{x},t))] = q(\mathbf{x},t), \tag{4.18}$$

where $\mathbf{W}$ is a perturbing velocity field. Further, we hypothesize ($i$) $\mathbf{W}$ to be periodic on $\partial\Omega$, ($ii$) components of $\mathbf{W}$ to be $L^\infty$ bounded by some positive constants $\bar{W}_i$ ($i = 1, 2, 3$),

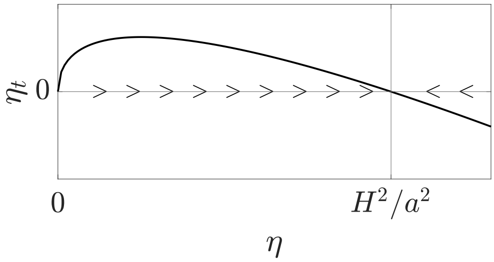

Figure 4.4: Phase portrait of system (4.25), bounding $\|e\|_2^2$ in the presence of spatio-temporal disturbances.

and $(iii)$ $\|\nabla \cdot \mathbf{W}\|_\infty \leq \widehat{W}$ . In such a scenario, the error dynamics become

$$e_t(\mathbf{x}, t) = -K_{\mathrm{p}} e(\mathbf{x}, t) + \nabla \cdot [\rho^{\mathrm{d}}(\mathbf{x}, t)\mathbf{W}(\mathbf{x}, t)] - \nabla \cdot [e(\mathbf{x}, t)\mathbf{W}(\mathbf{x}, t)]. \tag{4.19}$$

**Theorem 4.2** (Bounded stability with perturbations)**.** *In the presence of a bounded spatio-temporal disturbance* $\mathbf{W}$*, and if* $\|\rho^{\mathrm{d}}\|_2 \leq L$ *and* $\|\rho^{\mathrm{d}}_{x_i}\| \leq M_i$ *(*$i = 1, \dots, d$*), there exists a threshold value* $\kappa > 0$*, such that for* $K_{\mathrm{p}} > \kappa$*, the dynamics of* $\|e\|_2^2$ *remains bounded. Specifically,*

$$\lim_{t\to\infty} \sup \|e(\cdot, t)\|_2 \leq \frac{H}{2K_{\mathrm{p}} - \widehat{W}}, \tag{4.20}$$

*with* $H = 2\left(L\widehat{W} + \sum_{i=1}^{d} M_i \bar{W}_i\right)$.

*Proof.* We write the dynamics of $\|e\|_2^2$ as

$$(\|e\|_2^2)_t = 2\int_\Omega e e_t \, \mathrm{d}\mathbf{x} = -2K_{\mathrm{p}}\|e\|_2^2 + 2\int_\Omega e\nabla \cdot (\rho^{\mathrm{d}}\mathbf{W}) \, \mathrm{d}\mathbf{x} - 2\int_\Omega e\nabla \cdot (e\mathbf{W}) \, \mathrm{d}\mathbf{x}. \tag{4.21}$$

Similarly to the proof of Theorem 4.1 (specifically (4.11) and (4.12)), we can rewrite (4.21) as

$$(\|e\|_2^2)_t = 2\int_\Omega e e_t \, \mathrm{d}\mathbf{x} = -2K_{\mathrm{p}}\|e\|_2^2 + 2\int_\Omega e\nabla \cdot (\rho^{\mathrm{d}}\mathbf{W}) \, \mathrm{d}\mathbf{x} - \int_\Omega e^2\nabla \cdot \mathbf{W} \, \mathrm{d}\mathbf{x}. \tag{4.22}$$

Similarly to (4.13) and (4.14) in the proof of Theorem 4.1, we can give the bounds

$$\left|\int_\Omega e\nabla \cdot (\rho^{\mathrm{d}}\mathbf{W}) \, \mathrm{d}\mathbf{x}\right| \leq \int_\Omega \left|e\nabla \cdot (\rho^{\mathrm{d}}\mathbf{W})\right| \, \mathrm{d}\mathbf{x} = \|e\nabla \cdot (\rho^{\mathrm{d}}\mathbf{W})\|_1 = \|e\rho^{\mathrm{d}}\nabla \cdot \mathbf{W} + e\nabla\rho^{\mathrm{d}} \cdot \mathbf{W}\|_1 \leq$$

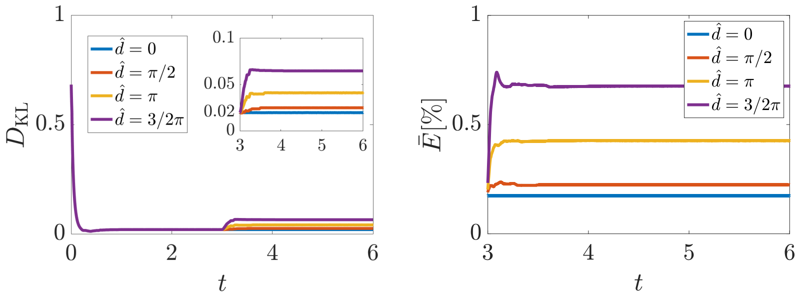

(a) (b)

Figure 4.5: Robustness to perturbations ($d=1$, $K_{\mathrm{p}}=10$): (a) time evolution of the KL divergence when a constant disturbance of amplitude $\hat{d}$ switches on at $t=3$ (in the inset, a zoom of the second half of the trial is given); (b) time evolution of the percentage error during the second half of the trial.

$$\le \|e\rho^{\mathrm{d}}\nabla\cdot\mathbf{W}\|_1+\|e\nabla\rho^{\mathrm{d}}\cdot\mathbf{W}\|_1 \le \|e\|_2\|\rho^{\mathrm{d}}\|_2\|\nabla\cdot\mathbf{W}\|_\infty+\|e\|_2\sum_{i=1}^{d}\|\rho^{\mathrm{d}}_{x_i}\|_2\|W_i\|_\infty \le \frac{H}{2}\|e\|_2, \tag{4.23}$$

$$\left|\int_\Omega e^2\nabla\cdot\mathbf{W}\,\mathrm{d}\mathbf{x}\right| \le \int_\Omega \left|e^2\nabla\cdot\mathbf{W}\,\mathrm{d}\mathbf{x}\right| = \left\|e^2\nabla\cdot\mathbf{W}\right\|_1 \le \|e\|_2\|e\|_2\|\nabla\cdot\mathbf{W}\|_\infty \le \widehat{W}\|e\|_2^2 \tag{4.24}$$

Then, setting $\eta=\|e\|_2^2$, we establish

$$\eta_t \le -A\eta + H\sqrt{\eta}, \tag{4.25}$$

where $H$ is given in the theorem statement, and $A=2K_{\mathrm{p}}-\widehat{W}$. If we assume $A$ to be positive, i.e., $2K_{\mathrm{p}}>\widehat{W}$, the bounding field is exhibiting a global asymptotically stable equilibrium point at $H^2/A^2$ (see Fig. 4.4 for a sketch of the phase portrait). Then, thanks to the Lemma 1.5, (4.20) is recovered. Hence, if $K_{\mathrm{p}}>\kappa>\widehat{W}/2$, $\|e\|_2$ remains bounded by $H/A$. ■

**Remark 4.4.** *Theorem 4.2 provides a bounded stability result in the presence of exogenous perturbations. By increasing the control gain $K_{\mathrm{p}}$, and consequently increasing the control effort, we can make the steady-state error arbitrarily small.*

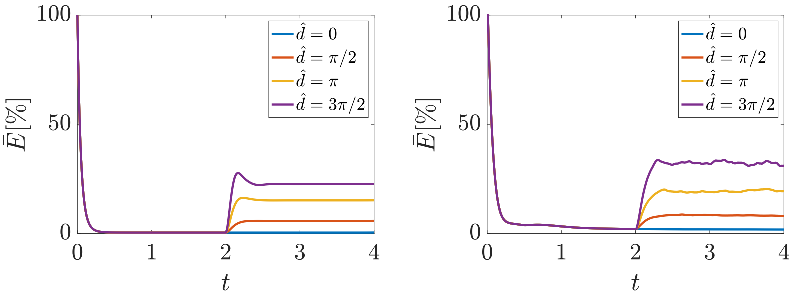

(a) (b)

Figure 4.6: Robustness to perturbations ($d = 1$, $K_\mathrm{p} = 100$): percentage error in time for (a) a continuous trial, (b) a discrete trial.

**Numerical validation** ($d = 1$) We consider the scenario presented in the previous section but assuming that a disturbance $W(x,t) = \hat{d}\,\mathrm{step}(t - t_\mathrm{f}/2)$ is acting on the macroscopic dynamics. Setting $K_\mathrm{p} = 10$ and considering different values of $\hat{d}$, we obtain the results reported in Fig. 4.5. In particular, results are characterized both in terms of KL divergence and percentage error, respectively in Fig. 4.5a and 4.5b. As expected, in the presence of the disturbance, the KL divergence and the percentage error remain bounded and decreases as the control gain $K_\mathrm{p}$ increases. For example, the steady-state value of the KL divergence decreases from 0.06 when $K_\mathrm{p} = 10$ to less than 0.02 when $K_\mathrm{p} \geq 100$ (for brevity, the result of this analysis varying $K_\mathrm{p}$ is omitted from the Thesis).

**Numerical validation** ($d = 2$) To numerically assess robustness to perturbations when agents move on the periodic square, we consider a step disturbance of amplitude $\hat{d}$ on both the $x$ and $y$ direction coming at half of the trial, that is $\mathbf{W}(x,t) = \hat{d}\,[\mathrm{step}(t - tf/2), \mathrm{step}(t - tf/2)]^T$. In this case, for a trial of 400 time steps, we observe the results in Fig. 4.6a for the continuous case and Fig. 4.6b for the discrete one. For both scenarios, we observe that, when the perturbation is active, the error settles to a bounded value, confirming findings in Theorem 4.2. We also remark that the error settles well below the theoretical estimation of Theorem 4.2, for example, when $\hat{d} = 3\pi/2$, $H/A \approx 0.8$, while $\|e(\cdot,t_\mathrm{f})\|_2 \approx 0.1$.

## 4.5 Discussion

We investigated the stability and robustness properties of a continuification control strategy for a set of agents in periodic domains. We quantified the extent to which the approach presented in Chapter 3 is robust when affected by (i) limited sensing capabilities of the agents, and (ii) spatio-temporal disturbances. In all cases, we establish the mathematical proofs of semiglobal asymptotic or bounded convergence – the latter in the form of a residual steady-state mismatch that can be made arbitrarily small by increasing the control gain.

In the next Chapter, we introduce a continuum framework for density control problems in leader-followers scenarios. In particular, the control strategy that is discussed in Chapter 3 (and whose robustness properties are discussed in this Chapter) suffers from the limitation that control needs to be applied to all the agents in the group to control. In what follows, we relax this assumption, assuming some control task needs to be solved by controlling only a subset of the agents in the group, namely the leaders. In so doing, we derive necessary and sufficient conditions about the feasibility of the problem, and, subsequently, we propose two different control strategies ensuring global convergence properties.

# 5 Leader-Follower Density Control in Large-Scale Multi-Agent Systems

In this Chapter we present the work in [33]. We address the problem of controlling the density of a large ensemble of follower agents by acting on a group of leader agents that interact with them. We formulate the problem as a system of coupled partial integro-differential equations describing the dynamics of the leaders' and followers' densities. We define feasibility conditions and propose two control architectures for exponential global stability. The first architecture is a feed-forward scheme for the followers. It adjusts the leaders' density via a feedback loop, which leverages information about leaders and a fixed reference density, to direct followers towards a target distribution. The second, dual feedback strategy employs a reference-governor to dynamically adapt the leaders' reference density based on measurements on both leaders and followers. Initially analyzed in one dimension, our methods are expanded to multi-dimensional applications. Numerical validations and an application in continuification-based control of leader-follower multiagent systems confirm the effectiveness of our approaches.

## 5.1 Introduction

Orchestrating the collective spatial organization of multi-agent systems is crucial in fields such as traffic control [109], collective additive manufacturing [110], synthetic biology [111], swarm robotics [112], and environmental management [113]. Leader-follower control strategies, where leader agents steer the behavior of a group of follower agents, are widely applied in these areas and other control applications [10, 11, 114, 115, 116, 117].

For example, the use of controlled autonomous vehicles has been proposed to improve traffic flows, avoiding stop-and-go waves and reducing emissions [15, 89]. In swarm robotics and synthetic biology, leader-follower dynamics can facilitate the management and regulation of large groups and cellular consortia [118, 119, 120, 121]. A key challenge is establishing analytical guarantees for achieving desired collective tasks. For instance, in the shepherding control problem, it is crucial to determine the optimal leader-to-follower ratios and sensing ranges to effectively manage group dynamics and corral and contain the followers towards desired regions in the state space [17, 122, 123, 124]. In complex multi-agent scenarios, microscopic models using ordinary (stochastic) differential equations are often replaced by macroscopic models using partial integro-differential equations to simplify analysis and enhance control of spatial organization on a large scale, avoiding its inherent curse of dimensionality [29, 30, 31, 48, 51, 52, 57, 58, 67, 98, 125, 126, 127].

In this Chapter, we address the challenge of applying macroscopic control techniques in leader-follower dynamics. Drawing from principles of mixture theory [176] and building on the state of the art, we represent the spatial interactions between two distinct populations of agents – leaders and followers – through two one-way coupled partial integro-differential equations, akin to mass conservation laws for different phases in a mixture. We synthesize a macroscopic control action to steer the density of the leaders so as to indirectly control that of the followers. First, we develop a feed-forward control scheme where the follower dynamics is tamed by making the leaders density converge towards a predetermined reference. Next, using a reference-governor approach, we make such a density a function of the actual followers' density and, hence, develop a dual-feedback control strategy comprising an inner loop on the leaders' density and an outer loop on the followers'. All our findings are corroborated by compelling numerical examples.

The main contributions of this Chapter are as follows:

- We introduce a simple, yet effective, model for the macroscopic spatial organization of two interacting populations of leaders and followers.
- We derive analytical conditions that determine the feasibility of solving the problem, considering factors such as the leaders/followers ratio, noisiness and sensing radius of the followers, and desired density to be achieved.
- We propose two control schemes that effectively solve the problem, formally proving that they ensure global exponential stability towards the desired behavior.
- We implement our macroscopic control solution on a population of finite size,

> thereby connecting it with the latest advances in continuification-based control schemes [26, 29, 30, 31]. This application demonstrates how large-scale control strategies can be effectively integrated with the detailed dynamics of individual agents, bridging macroscopic and microscopic methodologies.

The rest of the Chapter is organized as follows. Section 5.2 elaborates on the continuous leader-follower model. The feasibility of the problem is thoroughly examined in Section 5.4, which also leads to the development of two distinct control strategies, detailed in Sections 5.5 and 5.6 within a one-dimensional framework. Sections 5.7 and 5.8 presents the numerical validation of our proposed methodologies in macroscopic and microscopic scenarios, respectively. Finally, the higher-dimensional extension of the proposed approach is presented in Section 5.9, demonstrating its adaptability and scope.

## 5.2 The model

We study a continuous formulation of the leader-follower control problem, where a population of leader agents (or controllers) is assigned the task of taming the behavior of a population of follower agents (or targets). In this framework, also adopted differently in [130], two coupled equations are used to describe the spatio-temporal dynamics of the densities of the leaders and the followers. For simplicity, differently from [130] we do not consider interactions taking place between agents of the same population. In particular, a convection-diffusion equation is used to capture the dynamics of the followers assuming that they are random walkers at the microscopic level, see e.g. [17, 133]; their interaction with the leaders being captured by a cross convection term. Conversely, the leaders' dynamics is described by a mass conservation equation influenced by some control field, say $u$, resulting in

$$\rho_t^L(x,t) + \left[\rho^L(x,t)u(x,t)\right]_x = 0, \tag{5.1a}$$

$$\rho_t^F(x,t) + \left[\rho^F(x,t)v^{FL}(x,t)\right]_x = D\rho_{xx}^F(x,t), \tag{5.1b}$$

where $x \in \mathcal{S}$ and $t \in \mathbb{R}_{\geq 0}$ represent the space and time coordinates, $\rho^L, \rho^F : \mathcal{S} \times \mathbb{R}_{\geq 0} \to \mathbb{R}_{\geq 0}$ are the leaders' and followers' densities, $D \in \mathbb{R}_{\geq 0}$ weights the strength of the diffusion of the followers, and $u : \mathcal{S} \times \mathbb{R}_{\geq 0} \to \mathbb{R}$ is a velocity field to be designed in order to control the leaders' dynamics. No diffusion term is present in the leader equation, as we assume their microscopic counterpart to be deterministic. Also,

$$v^{FL}(x,t) = \int_{\mathcal{S}} f(\{x,y\})\rho^L(y,t)\,\mathrm{d}y = (f * \rho^L)(x,t) \tag{5.2}$$

is a velocity field modeling the influence of the leaders on the dynamics of the followers, where $\{x,y\} = (x-y+\pi)\bmod(2\pi)-\pi$ is the relative position between $x$ and $y$ wrapped on $\mathcal{S}$, and $f : \mathcal{S} \to \mathbb{R}$ is a soft-core (that is, returning bounded values when the argument is 0), odd interaction kernel [53]. To cope with the domain periodicity, we further assume $f$ to be periodic. Although the formulation is general, and any choice can be made for the kernel $f$, we fix it to be repulsive, that is, we choose

$$f(x) = \frac{1}{\mathrm{e}^{\frac{2\pi}{L}}-1}\,\mathrm{sgn}(x)\left[\mathrm{e}^{\frac{2\pi-|x|}{L}} - \mathrm{e}^{\frac{|x|}{L}}\right], \tag{5.3}$$

where $L$ is the characteristic interaction length.

**Remark 5.1.** *Notice that* (5.3) *is the periodic version of the more standard non-periodic repulsive kernel* $\hat{f}(x) = \mathrm{sgn}(x)\mathrm{e}^{-\frac{|x|}{L}}$, *which is typically considered in the literature [53, 64, 122], (see Appendix A). Also, note that our approach can easily be applied to the case of an attractive kernel by simply changing the sign in* (5.3).

By selecting $u$ in (5.1a) as a periodic function, such that $u(-\pi,t) = u(\pi,t)$ for all $t \in \mathbb{R}_{\geq 0}$, and imposing the periodic boundary condition

$$\rho^L(-\pi,t) = \rho^L(\pi,t), \quad \forall t \in \mathbb{R}_{\geq 0}, \tag{5.4}$$

we ensure conservation of the leaders' mass $M^L$, that is, $\left(\int_{\mathcal{S}} \rho^L(x,t)\,\mathrm{d}x\right)_t = 0$. Equation (5.1a) is also complemented with its initial condition, that is

$$\rho^L(x,0) = \rho_0^L(x), \tag{5.5}$$

where $\rho_0^L(x)$ is periodic and such that $\int_{\mathcal{S}} \rho_0^L\,\mathrm{d}x = M^L$.

As $v^{FL}$ in (5.1b) is periodic by construction (as it is defined as a circular convolution), the periodic boundary condition

$$\rho^F(-\pi,t) = \rho^F(\pi,t), \;\; \forall\, t \in \mathbb{R}_{\geq 0} \tag{5.6}$$

ensures the followers' mass, $M^F$, is conserved, that is $\left(\int_{\mathcal{S}} \rho^F\,\mathrm{d}x\right)_t = 0$ (recalling that the derivative of a periodic function is periodic itself). Equation (5.1b) is complemented with its initial condition, that is

$$\rho^F(x,0) = \rho_0^F(x), \tag{5.7}$$

where $\rho_0^F(x)$ is periodic and such that $\int_{\mathcal{S}} \rho_0^F \, \mathrm{d}x = M^F$.

**Remark 5.2.** *We consider $\rho_0^L, \rho_0^F \in H^2(\mathcal{S})$ (notice that, in principle, less regularity can be considered for $\rho_0^L$). Moreover, we remark that, requiring the periodicity of $\rho^i$, with $i = L, F$, ensures that the spatial derivatives of $\rho^i$ are periodic as well.*

We further assume that the overall mass of leaders and followers is normalized to 1, that is

$$M^L + M^F = 1. \tag{5.8}$$

Notice that, the mathematical set-up in (5.1) offers a macroscopic continuum description of the so-called shepherding control problem [17, 20]. Within this context, some controllable leader agents (or herders) are tasked to corral a large set of follower agents (or targets) into a pre-defined goal region. Many applications can be framed within this area, such as managing environmental pollutants via robotic systems [113], and search and rescue operations [177]. Moreover, our choice of stating the problem for periodic domains, not only simplify derivations, but also well adapts to describe phenomena that have been traditionally studied within this scope, like traffic and animal behavior problems [15, 164]. We also remark that our set-up can be easily adapted to deal with general, non-periodic domains, as done in [31] for a swarm robotics setting.

## 5.3 Problem statement

We seek to find a spatially periodic control input $u$ in (5.1a) such that, starting from $\rho_0^F$, the leaders will displace so that the followers distribution achieves a desired configuration, that is,

$$\lim_{t\to\infty} \|\bar{\rho}^F(\cdot) - \rho^F(\cdot,t)\|_2 = 0, \tag{5.9}$$

where $\bar{\rho}^F : \mathcal{S} \to \mathbb{R}_{>0}$ is the desired stationary periodic density profile for the followers. We note that, by designing $u$, we are indirectly controlling the dynamics of the followers' population by driving the density of the leaders, $\rho^L$, which, in turn, influences the followers' population through the interaction kernel $f$.

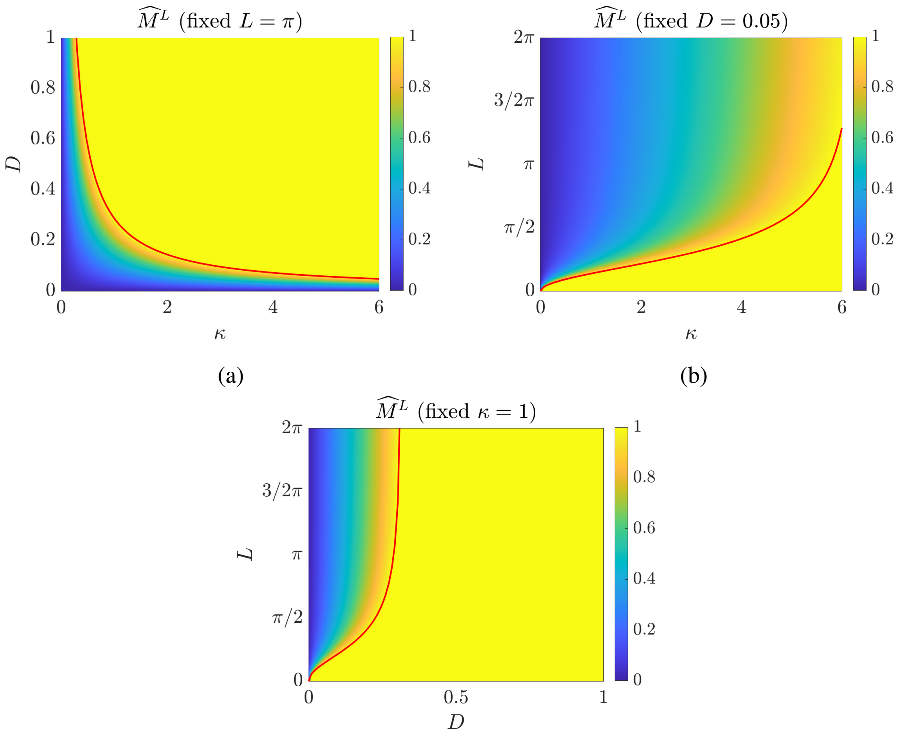

(a)

(b)

(c)

Figure 5.1: Feasibility plots: minimum amount of leaders' mass, $\widehat{M}^L$ for (a) fixed $L$ and varying $\kappa$ and $D$, (b) fixed $D$ and varying $\kappa$ and $L$, and (c) fixed $\kappa$ and varying $D$ and $L$. In red we show the curve indicating when $\widehat{M}^L$ becomes greater than 1. $\widehat{M}^L$ has been saturated to 1 for visualization purposes.

**Remark 5.3.** *Notice that, in the absence of leaders,* (5.1b) *describes Brownian motion of the followers at the macroscopic level. Such a behavior represents an effective evasive strategy, as shown in [133], within the context of a shepherding problem (see [20] for further details).*

## 5.4 Feasibility analysis

**Definition 5.1.** *We say that problem* (5.1)-(5.9) *admits a feasible steady-state solution (or, equivalently, that it is feasible) if, given a followers' mass* $0 < M^F < 1$*, there exists* *a leaders' density* $\bar{\rho}^L(x)$*, fulfilling the following two conditions:*

$$1.\ \ \bar{\rho}^L(x) \geq 0, \quad \forall\, x \in \mathcal{S}, \tag{D1.1}$$

$$2.\ \ \int_{\mathcal{S}} \bar{\rho}^L(x)\,\mathrm{d}x = M^L = 1 - M^F, \tag{D1.2}$$

*and such that the desired followers' density* $\bar{\rho}^F$ *is a steady-state solution of* (5.1b)*, upon setting* $v^{FL}(x,t) = \bar{v}^{FL}(x) := (f * \bar{\rho}^L)(x)$*.*

**Remark 5.4.** *Notice that we do not explicitly require* $\bar{\rho}^L$ *to be a solution of* (5.1a)*, as we can enforce it via an appropriate choice of the control input u, as it is shown in Sec. 5.5.1.*

Hence, for the problem to be feasible, a necessary condition is for $\bar{\rho}^F$ to be a steady-state solution of (5.1b)

$$\left[\bar{\rho}^F(x)\bar{v}^{FL}(x)\right]_x = D\bar{\rho}^F_{xx}(x). \tag{5.10}$$

By spatial integration, recalling $\bar{\rho}^F(x) \neq 0\ \forall\, x \in \mathcal{S}$ (see Section 5.3), we can recover the expression of the velocity field $\bar{v}^{FL}$ such that, being the problem set in $H^2(\mathcal{S})$, (5.10) is fulfilled almost everywhere,

$$\bar{v}^{FL}(x) = D\frac{\bar{\rho}^F_x(x)}{\bar{\rho}^F(x)} + \frac{A}{\bar{\rho}^F(x)}, \tag{5.11}$$

where $A$ is an arbitrary integration constant. Note that, by reformulating the problem in $C^2(\mathcal{S})$ and not in $H^2(\mathcal{S})$, (5.11) would hold point wise.

To find $A$, we notice that, as $f$ is odd, from Fubini's theorem for convolutions [178], we must have

$$\int_{\mathcal{S}} \bar{v}^{FL}(x)\,\mathrm{d}x = \int_{\mathcal{S}} (f * \bar{\rho}^L)(x)\,\mathrm{d}x = \int_{\mathcal{S}} f(x)\,\mathrm{d}x \int_{\mathcal{S}} \bar{\rho}^L(x)\,\mathrm{d}x = 0. \tag{5.12}$$

Then, using (5.12), from (5.11) we can derive

$$A = -\frac{D\int_{\mathcal{S}} \bar{\rho}^F_x(x)/\bar{\rho}^F(x)\,\mathrm{d}x}{\int_{\mathcal{S}} 1/\bar{\rho}^F(x)\,\mathrm{d}x} = -\frac{D\left[\log(\bar{\rho}^F(x))\right]_{-\pi}^{\pi}}{\int_{\mathcal{S}} 1/\bar{\rho}^F(x)\,\mathrm{d}x} = 0, \tag{5.13}$$

because of the periodicity of $\bar{\rho}^F$. Thus, setting $A = 0$ in (5.11) we find

$$\bar{v}^{FL}(x) = D\frac{\bar{\rho}^F_x(x)}{\bar{\rho}^F(x)}. \tag{5.14}$$

Given the expression of $\bar{v}^{FL}$ in (5.14), knowing that $\bar{v}^{FL} = f * \bar{\rho}^L$, and assuming the expression of the repulsive kernel in (3.24), we can recover the reference leaders' density $\bar{\rho}^L$ by deconvolution [179] (see Appendix B for more details), yielding

$$\bar{\rho}^L(x) = \frac{\bar{v}^{FL}_x(x)}{2} - \frac{1}{2L^2}\int \bar{v}^{FL}(x)\,\mathrm{d}x + B, \tag{5.15}$$

where $B$ is an arbitrary constant. Note that the deconvolution operation does not automatically guarantee that the resulting leaders' density $\bar{\rho}^L$ is feasible according to Definition 5.1. Then, problem (5.1)-(5.9) is feasible if there exists a constant $B$ in (5.15) such that conditions (D1.1) and (D1.2) in Definition 5.1 hold.

Using (5.15), (D1.1), and (D1.2), we can derive a lower bound on the mass of leaders needed to make the problem feasible as a function of the kernel parameters, the diffusivity of the followers, and the desired density profile. In what follows, we normalize the desired followers' density as

$$\bar{\rho}^F(x) = M^F\hat{\rho}^F(x), \tag{5.16}$$

with

$$\int_S \hat{\rho}^F(x)\,\mathrm{d}x = 1. \tag{5.17}$$

**Theorem 5.1.** *Problem (5.1)-(5.9) with $f$ chosen as in (3.24) is feasible according to Definition 5.1 if and only if, given $\hat{\rho}^F$ as in (5.16), the leaders' mass $M^L$ is such that*

$$\widehat{M}^L \le M^L < 1 \tag{5.18}$$

*with*

$$\widehat{M}^L = \max_x \{h(x)\},$$

*where*

$$h(x) = -\pi D g_1(x) + \frac{\pi D}{L^2}g_2(x) - \frac{DC}{2L^2}, \tag{5.19}$$

*and*

$$g_1(x) = \left[\log(\hat{\rho}^F(x))\right]_{xx} = \left(\frac{\hat{\rho}^F_x(x)}{\hat{\rho}^F(x)}\right)_x, \tag{5.20}$$

$$g_2(x) = \log(\hat{\rho}^F(x)), \tag{5.21}$$

$$C = \int_{\mathcal{S}} \log(\hat{\rho}^F(x))\,\mathrm{d}x. \tag{5.22}$$

*Proof.* We first prove sufficiency (⇒). Substituting (5.16) into (5.14) we rewrite $\bar{v}^{FL}$ as

$$\bar{v}^{FL}(x) = D\frac{\hat{\rho}^F_x(x)}{\hat{\rho}^F(x)}. \tag{5.23}$$

Using this expression for $\bar{v}^{FL}$ in (5.15), we obtain

$$\int_{\mathcal{S}} \bar{\rho}^L(x)\,\mathrm{d}x = -\frac{DC}{2L^2} + 2\pi B, \tag{5.24}$$

where we used the periodicity of $\bar{v}^{FL}$ and choose $C$ as in (5.22). Now, to fulfill (D1.2) in Definition 5.1, we select the arbitrary constant $B$ in (5.15) as

$$B = \frac{1}{2\pi}\left(1 - M^F + \frac{DC}{2L^2}\right). \tag{5.25}$$

Substituting this expression of $B$ into (5.15), and computing $\bar{v}^{FL}_x$, from (D1.1) we have

$$\bar{\rho}^L(x) = \frac{D}{2}g_1(x) - \frac{D}{2L^2}g_2(x) + \frac{1}{2\pi}\left(1 - M^F + \frac{DC}{2L^2}\right) \geq 0, \tag{5.26}$$

with $g_1$ and $g_2$ given by (5.20) and (5.21), respectively.

Hence, problem (5.9) admits a feasible solution if (5.26) is fulfilled. From (5.26), knowing that $M^L = 1 - M^F$, it follows

$$M^L \geq -\pi D g_1(x) + \frac{\pi D}{L^2}g_2(x) - \frac{DC}{2L^2} = h(x), \quad \forall x \in \mathcal{S}, \tag{5.27}$$

which is always fulfilled under (5.18), thus proving sufficiency.

To prove necessity (⇐), we assume feasibility, that is, we know there exists some non-negative $\bar{\rho}^L$ summing to $M^L \in (0, 1)$, making $\bar{\rho}^F$ a steady-state solution of (5.1b). Hence, the steps from (5.23) to (5.27) hold by assumption. Being $M^L$ constant, it must be $M^L \geq \widehat{M}^L$ for (5.27) to hold. ■

**Remark 5.5.** *The use of Theorem 5.1 (specifically, condition (5.18)) is twofold. (i) Given the normalized desired followers' density to achieve, one can derive a condition on the minimum amount of leaders' mass $M^L$ that makes the problem feasible. (ii) Given the available mass of leaders, one can identify what desired densities of followers can be effectively achieved.*

**Remark 5.6.** *The whole feasibility analysis can be carried out also assuming some more complex followers' density dynamics. Specifically, in Appendix C.1, we give some details about the case of followers showing followers-followers interactions in the convective term, that here were omitted from the analysis for simplicity.*

### 5.4.1 An example

Let us assume that the normalized desired followers' density is the von Mises distribution

$$\hat{\rho}^F(x) = \frac{\mathrm{e}^{\kappa\cos(x-\mu)}}{2\pi I_0(\kappa)}, \tag{5.28}$$

where $\kappa$ is the concentration coefficient, $\mu$ is the mean and $I_0$ is the modified Bessel function of the first kind of order 0. Without any loss of generality, we fix $\mu = 0$ and use (5.20), (5.21), (5.22) to compute

$$g_1(x) = -\kappa\cos(x), \tag{5.29a}$$

$$g_2(x) = \kappa\cos(x) - \log[2\pi I_0(\kappa)], \tag{5.29b}$$

$$C = -2\pi\log[2\pi I_0(\kappa)]. \tag{5.29c}$$

Substituting into (5.19), we obtain

$$h(x) = \pi D\left(1 + \frac{1}{L^2}\right)\kappa\cos(x), \tag{5.30}$$

whose maximum in $\mathcal{S}$ is

$$\widehat{M}^L = \max_{x\in\mathcal{S}} h(x) = \pi D\left(1 + \frac{1}{L^2}\right)\kappa. \tag{5.31}$$

Therefore, from Theorem 5.1 the problem is feasible if

$$\pi D\left(1 + \frac{1}{L^2}\right)\kappa < M^L < 1 \tag{5.32}$$

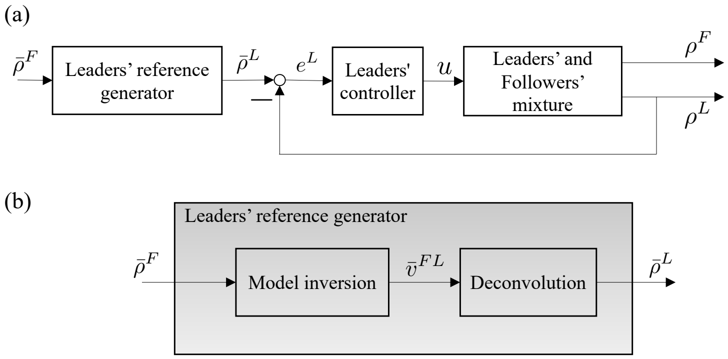

Figure 5.2: (a) Feed-forward control scheme. (b) Detail of the leaders' reference generator block (where the feasibility analysis is performed).

In Fig. 5.1, we report $\widehat{M}^L$ as a function of $D$, $L$ and $\kappa$ in three different scenarios. Specifically, in Fig. 5.1a, we consider $L = \pi$ and we let $\kappa$ and $D$ vary; in Fig. 5.1b, we fix $D = 0.05$ and we let $\kappa$ and $L$ vary; in Fig. 5.1c, we fix $\kappa = 1$ and let $D$ and $L$ vary. From Fig. 5.1 we notice that a larger leaders' mass is needed for larger values of $D$ and $\kappa$, and for smaller values of $L$. This suggests that highly diffusive followers (large $D$) require more leaders for effective control, supporting the use of random walks as an evasive strategy [133]. Moreover, achieving more concentrated desired density profiles (large $\kappa$) demands a greater mass of leaders. Additionally, as expected, a broader area of influence (large $L$) simplifies the leaders' task.

For completeness, we also report the resulting expression of the reference leaders' density as computed from (5.15) with $B$ from (5.25), that is,

$$\bar{\rho}^L(x) = -\frac{D\,\kappa}{2}\left(1 + \frac{1}{L^2}\right)\cos(x) + \frac{M^L}{2\pi}. \tag{5.33}$$

## 5.5 Feed-forward control

Assuming the problem is feasible according to Definition 5.1, we shall seek to find an expression for $u$ in (5.1a) that drives the leaders' density from $\rho_0^L$ towards $\bar{\rho}^L$ (computed from (5.15), fixing $B$ as in (5.25)) and, under appropriate conditions, renders $\bar{\rho}^F$ an asymptotically stable solution of (5.1b). The overall control scheme is reported in Fig. 5.2. We wish to point out that the control solution we propose here does not use information about the followers' density $\rho^F$ when controlling the leaders, making it a feed-forward solution with respect to the followers' dynamics. To make the solution more robust, including information about $\rho^F$, we propose a reference-governor scheme in Section 5.6.

### 5.5.1 Leaders' control design

Given a desired density profile, $\bar{\rho}^L$, fulfilling (D1.1) and (D1.2) in Definition 5.1, we want to choose $u$ in (5.1a) so as to drive $\rho^L$ to it. We recall that a spatially periodic $u$ ensures leaders' mass conservation (see Section 5.2).

We define the leaders' density error as

$$e^L(x,t) = \bar{\rho}^L(x) - \rho^L(x,t). \tag{5.34}$$

Notice that the following integral condition is fulfilled:

$$\int_{\mathcal{S}} e^L(x,t)\,\mathrm{d}x = \int_{\mathcal{S}} \left(\bar{\rho}^L(x) - \rho^L(x,t)\right)\,\mathrm{d}x = M^L - M^L = 0, \quad \forall t \in \mathbb{R}_{\geq 0}. \tag{5.35}$$

**Theorem 5.2** (Leaders' global exponential convergence)**.** *Choosing $u$ from the spatial integration of*

$$\left[\rho^L(x,t)u(x,t)\right]_x = -K_L e^L(x,t), \tag{5.36}$$

*with $K_L > 0$, makes the leaders' error dynamics globally exponentially convergent to zero.*

*Proof.* From (5.34) and (5.1a), the leaders' error dynamics obeys

$$e^L_t(x,t) = -\rho^L_t(x,t) = \left[\rho^L(x,t)u(x,t)\right]_x, \tag{5.37}$$

with its initial and periodic boundary condition

$$e^L(x,0) = \bar{\rho}^L(x) - \rho^L_0(x) \ \ \forall x \in \mathcal{S} \tag{5.38a}$$

$$e^L(-\pi,t) = e^L(\pi,t) \ \ \forall t \in \mathbb{R}_{\geq 0}. \tag{5.38b}$$

Substituting (5.36) into (5.37) yields

$$e^L_t(x,t) = -K_L e^L(x,t), \tag{5.39}$$

which is a linear globally convergent PDE. Therefore,

$$e^L(x,t) = e^L(x,0)\exp\{-K_L t\}. \tag{5.40}$$

■

**Remark 5.7.** *The control action is obtained with the same fashion discussed in Chapter 2.2 (here we neglect interactions between the agents of the same population). Moreover, $u$ can be derived by a spatial integration of (5.36), that is*

$$u(x,t) = -\frac{K_L}{\bar{\rho}^L(x) - e^L(x,t)} \int e^L(x,t)\,\mathrm{d}x, \tag{5.41}$$

*where the integration constant was set to 0. Notice that $u$ is well defined only if $\rho^L(x,t) \neq 0$ (recalling $\rho^L = \bar{\rho}^L - e^L$), as no control is exertable otherwise.*

The periodicity of $u$, which is proved next, ensures that leaders' mass is conserved ( $\int_{\mathcal{S}} \rho^L_t(x,t)\,\mathrm{d}x = 0$).

**Corollary 5.1.** *The field $u$ obtained by spatially integrating (5.36) is periodic, that is $u(-\pi,t) = u(\pi,t)\ \forall\, t \in \mathbb{R}_{\geq 0}$.*

*Proof.* By spatially integrating (5.36) in $\mathcal{S}$, we get

$$\int_{\mathcal{S}} \left[\rho^L(x,t)u(x,t)\right]_x \mathrm{d}x = -\int_{\mathcal{S}} K_L e^L(x,t)\,\mathrm{d}x = 0, \tag{5.42}$$

where we used (5.35). Expanding the first member of (5.42) implies

$$\rho^L(-\pi,t)u(-\pi,t) = \rho^L(\pi,t)u(\pi,t). \tag{5.43}$$

As $\rho^L(\pi,t) = \rho^L(-\pi,t)$ from the boundary conditions of (5.1a), the thesis follows. ■

**Remark 5.8.** *Notice that the overall control strategy for the leaders' density can be easily adapted to tracking scenarios. Indeed, if $\tilde{\rho}^L(x,t)$ is a time varying periodic density fulfilling some mass conservation principle (that is, $\int_{\mathcal{S}} \tilde{\rho}^L_t(x,t)\,\mathrm{d}x = 0$), choosing*

$$\left[\rho^L(x,t)u(x,t)\right]_x = -\tilde{\rho}^L_t(x,t) - K_L e^L(x,t), \tag{5.44}$$

*still allows the error dynamics to be recast as in (5.39) (in this context the error is $e^L = \tilde{\rho}^L - \rho^L$). Such a choice is also associated with a periodic velocity field $u$ (ensuring* *well posedness is preserved) as*

$$\int_{\mathcal{S}} \left[-\tilde{\rho}_t^L(x,t) - K_L e^L(x,t)\right] \,\mathrm{d}x = 0, \quad \forall\, t \geq 0, \tag{5.45}$$

*letting* (5.43) *and, consequently, Corollary 5.1 still holds.*

### 5.5.2 Followers' stability analysis

Under the control action discussed in Section 5.5.1, we know leaders' density exponentially converges to $\bar{\rho}^L$. Here, we prove that, under suitable conditions, global exponential stability of the followers density towards $\bar{\rho}^F$ is also attained.

We define the followers' error as

$$e^F(x,t) = \bar{\rho}^F(x) - \rho^F(x,t). \tag{5.46}$$

Notice that, by construction, $\int_{\mathcal{S}} e^F(x,t)\,\mathrm{d}x = 0 \;\forall\, t \geq 0$. The error dynamics is given by

$$e_t^F(x,t) = \left[\left(\bar{\rho}^F(x) - e^F(x,t)\right) v^{FL}(x,t)\right]_x + D\left(e_{xx}^F(x,t) - \bar{\rho}_{xx}^F(x)\right), \tag{5.47}$$

subject to initial and periodic boundary conditions

$$e^F(x,0) = \bar{\rho}^F(x) - \rho^F(x,0) \;\; \forall\, x \in \mathcal{S} \tag{5.48a}$$

$$e^F(-\pi,t) = e^F(\pi,t) \;\; \forall\, t \in \mathbb{R}_{\geq 0}. \tag{5.48b}$$

**Theorem 5.3** (Followers' global exponential stability)**.** *In a feasible scenario according to Theorem 5.1, if*

$$K^{ff} = -2D + D\|g_1(\cdot)\|_\infty + \|h_1(\cdot)\|_\infty < 0, \tag{5.49}$$

*where*

$$h_1(x) = \left[(f * \rho_0^L)(x)\right]_x, \tag{5.50}$$

*and $g_1$ comes from* (5.20)*, the error dynamics* (5.47) *globally exponentially converges to 0 in $\mathcal{L}^2(\mathcal{S})$. If $K_L \gg |K^{ff}|$, the rate of convergence is $|K^{ff}|$.*

*Proof.* From (5.40), we know that

$$\rho^L(x,t) = \bar{\rho}^L(x) + \Phi(x,t), \tag{5.51}$$

where

$$\Phi(x,t) = -\left[\bar{\rho}^L(x) - \rho^L(x,0)\right]\exp(-K_L t) \tag{5.52}$$

represents the transient leaders' behavior. Recalling that $v^{FL} = f * \rho^L$, (5.47) can be rewritten as

$$\begin{aligned} e_t^F(x,t) = D\left(e_{xx}^F(x,t) - \bar{\rho}_{xx}^F(x)\right) + \left[\left(\bar{\rho}^F(x) - e^F(x,t)\right)(f * \bar{\rho}^L)(x)\right]_x \\ + \left[\left(\bar{\rho}^F(x) - e^F(x,t)\right)(f * \Phi)(x,t)\right]_x . \end{aligned} \tag{5.53}$$

By substituting (5.52) into (5.53), and recalling that, upon the fulfillment of the feasibility condition, $f * \bar{\rho}^L = \bar{v}^{FL}$, we recover

$$\begin{aligned} e_t^F(x,t) = De_{xx}^F(x,t) - D\left[1 - \exp(-K_L t)\right]\left[e^F(x,t)\frac{\bar{\rho}_x^F(x)}{\bar{\rho}^F(x)}\right]_x \\ + \exp(-K_L t)\left[(\bar{\rho}^F(x) - e^F(x,t))(f * \rho_0^L)(x) - D\bar{\rho}_x^F(x)\right]_x . \end{aligned} \tag{5.54}$$

Choosing $\|e^F\|_2^2$ as a Lyapunov functional, and recalling $\left(\|e^F\|_2^2\right)_t = \int_S e^F e_t^F \,\mathrm{d}x$, we obtain

$$\begin{aligned} \left(\|e^F(\cdot,t)\|_2^2\right)_t = 2D\int_S e^F(x,t)e_{xx}^F(x,t)\,\mathrm{d}x \\ - 2D\left[1 - \exp(-K_L t)\right]\int_S e^F(x,t)\left[e^F(x,t)\frac{\bar{\rho}_x^F(x,t)}{\bar{\rho}^F(x)}\right]_x \mathrm{d}x \\ + 2\exp(-K_L t)\int_S e^F(x,t)\left[(\bar{\rho}^F(x) - e^F(x,t))(f * \rho_0^L)(x) - D\bar{\rho}_x^F(x)\right]_x \mathrm{d}x, \end{aligned} \tag{5.55}$$

where we used (5.54). Integrating by parts the terms at the right hand-side of (5.55) (accounting for their periodicity), and recalling that $[(e^F)^2]_x = 2e^F e_x^F$, we can establish the following identities:

$$2D\int_S e^F(x,t)e_{xx}^F(x,t)\,\mathrm{d}x \;=\; -2D\int_S (e_x^F(x,t))^2\,\mathrm{d}x \;=\; -2D\|e_x^F(\cdot,t)\|_2^2, \tag{5.56a}$$

$$-2D\left[1 - \exp(-K_L t)\right]\int_S e^F(x,t)\left[e^F(x,t)\frac{\bar{\rho}_x^F(x,t)}{\bar{\rho}^F(x)}\right]_x \mathrm{d}x =$$

$$\begin{aligned}
&= D\left[1-\exp(-K_L t)\right]\int_{\mathcal{S}} 2e_x^F(x,t)e^F(x,t)\frac{\bar{\rho}_x^F(x,t)}{\bar{\rho}^F(x)}\,\mathrm{d}x = \\
&= D\left[1-\exp(-K_L t)\right]\int_{\mathcal{S}} \left[(e^F(x,t))^2\right]_x \frac{\bar{\rho}_x^F(x,t)}{\bar{\rho}^F(x)}\,\mathrm{d}x = \\
&= -D\left[1-\exp(-K_L t)\right]\int_{\mathcal{S}} (e^F(x,t))^2 g_1(x)\,\mathrm{d}x, \qquad (5.56\text{b})
\end{aligned}$$

$$\begin{aligned}
&-2\exp(-K_L t)\int_{\mathcal{S}} e^F(x,t)\left[e^F(x,t)(f*\rho_0^L)(x)\right]_x \mathrm{d}x = \\
&= \exp(-K_L t)\int_{\mathcal{S}} 2e^F(x,t)e_x^F(x,t)(f*\rho_0^L)(x)\,\mathrm{d}x = \\
&= \exp(-K_L t)\int_{\mathcal{S}} \left[(e^F(x,t))^2\right]_x (f*\rho_0^L)(x)\,\mathrm{d}x = \\
&= -\exp(-K_L t)\int_{\mathcal{S}} (e^F(x,t))^2 h_1(x)\,\mathrm{d}x, \qquad (5.56\text{c})
\end{aligned}$$

where $h_1$ is defined in (5.50). Accounting for the identities (5.56) into (5.55), yields to

$$\begin{aligned}
\left(\|e^F(\cdot,t)\|_2^2\right)_t &= -2D\|e_x^F(\cdot,t)\|_2^2 - D\left[1-\exp(-K_L t)\right]\int_{\mathcal{S}} (e^F(x,t))^2 g_1(x)\,\mathrm{d}x \\
&- \exp(-K_L t)\int_{\mathcal{S}} (e^F(x,t))^2 h_1(x)\,\mathrm{d}x + 2\exp(-K_L t)\int_{\mathcal{S}} e^F(x,t)h_2(x)\,\mathrm{d}x, \qquad (5.57)
\end{aligned}$$

where we posed $h_2 = [\bar{\rho}^F(f*\rho_0^L) - D\bar{\rho}_x^F]_x$. Using the Poincaré-Wirtinger inequality and the Hölder inequality (see Lemma 1.4 and 1.1), we can establish the following bounds:

$$-2D\|e_x^F(\cdot,t)\|_2 \le -2D\|e^F(\cdot,t)\|_2^2, \qquad (5.58\text{a})$$

$$\begin{aligned}
&-D\left[1-\exp(-K_L t)\right]\int_{\mathcal{S}} (e^F(x,t))^2 g_1(x)\,\mathrm{d}x \le \\
&\le D\left[1-\exp(-K_L t)\right]\left|\int_{\mathcal{S}} (e^F(x,t))^2 g_1(x)\,\mathrm{d}x\right| \le \\
&\le D\left[1-\exp(-K_L t)\right]\int_{\mathcal{S}} \left|(e^F(x,t))^2 g_1(x)\right|\,\mathrm{d}x = \\
&= D\left[1-\exp(-K_L t)\right]\|(e^F(\cdot,t))^2 g_1(\cdot)\|_1 \le \\
&\le D\|g_1(\cdot)\|_\infty\|e^F(\cdot,t)\|_2^2 \qquad (5.58\text{b})
\end{aligned}$$

$$-\exp(-K_L t)\int_S (e^F(x,t))^2 h_1(x)\,\mathrm{d}x \;\leq \|h_1(\cdot)\|_\infty \|e^F(\cdot,t)\|_2^2 \tag{5.58c}$$

$$\begin{aligned}2\exp(-K_L t)\int_S e^F(x,t)h_2(x)\,\mathrm{d}x \leq 2\exp(-K_L t)\left|\int_S e^F(x,t)h_2(x)\,\mathrm{d}x\right| \leq\\ \leq 2\exp(-K_L t)\int_S \left|e^F(x,t)h_2(x)\right|\,\mathrm{d}x = 2\exp(-K_L t)\|e^F(x,t)h_2(x)\|_1 \leq\\ \leq 2\exp(-K_L t)\|h_2(x)\|_2\|e^F(x,t)\|_2.\end{aligned} \tag{5.58d}$$

Note that, the derivation of (5.58c) follows the steps of (5.58b). Moreover, we exploited the fact that $1-\exp(-K_L t)$ and $\exp(-K_L t)$ are positive and bounded by 1.

Exploiting the bounds in (5.58) into (5.57), we obtain

$$\begin{aligned}\left(\|e^F(\cdot,t)\|_2^2\right)_t \leq (-2D + D\|g_1(\cdot)\|_\infty + \|h_1(\cdot)\|_\infty)\|e^F(\cdot,t)\|_2^2\\ + 2\|h_2(\cdot)\|_2\exp(-K_L t)\|e^F(\cdot,t)\|_2.\end{aligned} \tag{5.59}$$

The bounding system at the right hand-side of (5.59) converges to 0 globally and exponentially due to Lemma 1.6 (fixing $\eta = \|e^F\|_2^2$, $\gamma = -K^{ff}$, $\delta = 2\|h_2\|_2$ and $K = K^L$). Moreover its rate of convergence is given by $|K^{ff}|$. Hence, by comparison lemma (see Lemma 1.5), the theorem is proved. ■

**Remark 5.9.** *Notice that, for the paradigmatic example where* $\rho_0^L$ = const, $\|h_1\|_\infty = 0$. *Moreover, as the rate of convergence* $|K^{ff}|$ *is independent from the control parameters, it can be noticed that the proposed control strategy does not allow for choosing a desired rate of convergence for the followers.*

The control scheme proposed so far does not rely on any information sensed in real-time about the followers' displacement, rendering the solution not robust to perturbations, as detailed by the numerical simulations reported later in Section 5.7.1. This underscores the necessity for expanding the strategy in order to incorporate some feedback mechanism on the followers' dynamics, as discussed in Section 5.6.

**Remark 5.10.** *The proposed control scheme can be adapted to scenarios in which the feasibility analysis is not fulfilled. In such adaptation, bounded convergence can still be guaranteed (see Appendix C.2 for more details).*

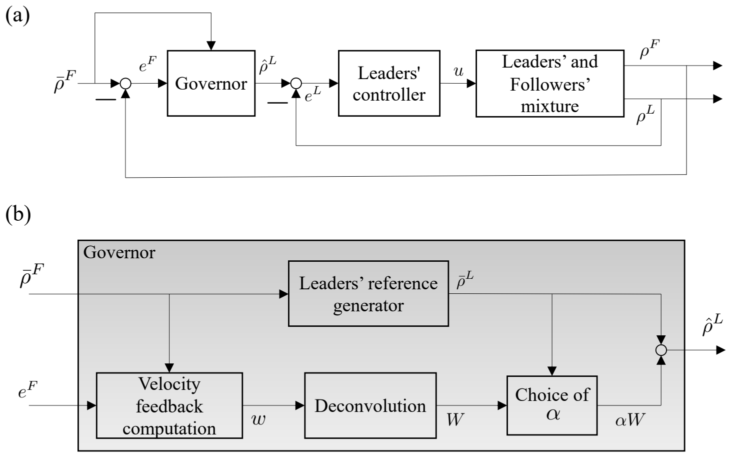

Figure 5.3: (a) Reference-governor control scheme. (b) Detail of the governor block.

## 5.6 Reference-governor control

The control strategy introduced in Section 5.5 does not include any feedback on the followers' density. To address the objective outlined in (5.9) and incorporate feedback related to the followers' density, we introduce a reference-governor approach, inspired by [180]. This method employs a dual-feedback loop structure: the outer loop, or the governor loop, dynamically adjusts the target density for the leaders, $\hat{\rho}^L$, aiming to minimize the error $e^F = \bar{\rho}^F - \rho^F$ by facilitating the required organization of the followers. The inner loop, or the leaders' control loop, then calculates the control input $u$ as per (5.1a), to guide the actual leaders' density, $\rho^L$, towards $\hat{\rho}^L$, thereby reducing the discrepancy $e^L = \hat{\rho}^L - \rho^L$ to zero and fulfilling the control objectives. An illustration of this strategy is depicted in Fig. 5.3. Note that for controlling the leaders' density we leverage the framework previously detailed in Section 5.5.1 (see Remark 5.8 specifically).

### 5.6.1 Governor design

Here, we discuss the design of the governor and explore its stability properties. Because of Theorem 5.2, and in particular Remark 5.8, we know that, given some leaders' desired time-varying density , choosing $u$ in (5.1a) as (5.44), it is

$$\rho^L(x,t) = \hat{\rho}^L(x,t) + \Phi(x,t), \tag{5.60}$$

where $\Phi$ represents the leaders' transient behavior, that is

$$\Phi(x,t) = -\left[\hat{\rho}^L(x,0) + \rho_0^L(x)\right] \exp(-K_L t). \tag{5.61}$$

Hence, recalling (5.2), and because of the linearity of the convolution operator, $v^{FL}$ in (5.1b) can be decomposed as

$$v^{FL}(x,t) = \hat{v}^{FL}(x,t) + (f * \Phi)(x,t), \tag{5.62}$$

where $\hat{v}^{FL} = f * \hat{\rho}$. In what follows, we recover an expression for $\hat{v}^{FL}$ that, by means of Lyapunov arguments, can be proved to ensure the convergence of the followers' error to 0. After that, we show how to deconvolve such a velocity field to obtain $\hat{\rho}^L$, for the leaders to track. Specifically, we choose $\hat{v}^{FL}$ to incorporate the feed-forward action that was discussed in Section 5.5, and a feedback correction whose weight can be chosen online to ensure physical constraints are met. In particular,

$$\hat{v}^{FL}(x,t) = (f * \hat{\rho}^L)(x,t) = \bar{v}^{FL}(x) + \alpha(t)\, w(x,t) \tag{5.63}$$

where $\bar{v}^{FL}$ is the feed-forward term chosen as in (5.14), $\alpha : \mathbb{R}_{\geq 0} \to [0,1]$ is a control function to be appropriately selected, and

$$w(x,t) = \frac{D\bar{\rho}_x^F(x) e^F(x,t)}{\bar{\rho}^F(x)\left(\bar{\rho}^F(x) - e^F(x,t)\right)}. \tag{5.64}$$

is a feedback correction term modulated by $\alpha(t)$.

**Remark 5.11.** *Equation (5.64) is well defined only if $\rho^F > 0$, as $\bar{\rho}^F \in \mathbb{R}_{>0}$ (see Section 5.3). This condition is reasonable whereby: (i) there is no need to exert a control action where the followers' density is null, and (ii) in practical scenarios, $\rho^F$ is estimated from the positions of a discrete set of agents using, for instance, a Gaussian kernel estimator [168], which ensures this assumption is always met.*

**Theorem 5.4** (Followers' global exponential stability)**.** *In a feasible scenario according to Theorem 5.1, the followers' density (whose dynamics is described in (5.1b), with $v^{FL}$ given in (5.62) and $\hat{v}^{FL}$ coming from (5.63)), globally exponentially converges to the desired density $\bar{\rho}^F$ in $\mathcal{L}^2(\mathcal{S})$, for any choice of $\alpha(t) \in [0,1]$, if*

$$K^{rg} = -2D + D\|g_1(\cdot)\|_\infty + \|h_1\|_\infty < 0. \tag{5.65}$$

*If $K_L \gg |K^{rg}|$, the rate of convergence is bounded by $K^{rg}$.*

*Proof.* The followers' error dynamics obeys to (5.47) with initial and periodic boundary conditions set as in (5.48). Substituting (5.62) into (5.47) yields

$$e_t^F(x,t) = D\left(e_{xx}^F(x,t) - \bar{\rho}_{xx}^F(x)\right) + \left[\left(\bar{\rho}^F(x) - e^F(x,t)\right)\hat{v}^{FL}(x,t)\right]_x \\ + \left[\left(\bar{\rho}^F(x) - e^F(x,t)\right)(f * \Phi)(x,t)\right]_x . \quad (5.66)$$

Substituting (5.63) (with $w$ coming from (5.64)), we obtain

$$e_t^F(x,t) = De_{xx}^F(x,t) - D\left[1 - \exp(-K_L t)\right]\left[e^F(x,t)\frac{\bar{\rho}_x^F(x)}{\bar{\rho}^F(x)}\right]_x \\ +D\alpha(t)\left[e^F(x,t)\frac{\bar{\rho}_x^F(x)}{\bar{\rho}^F(x)}\right]_x + \exp(-K_L t)\left[(\bar{\rho}^F(x) - e^F(x,t))(f * \rho_0^L)(x) - D\bar{\rho}_x^F(x)\right]_x . \\ (5.67)$$

Similarly to Theorem 5.3, we introduce the Lyapunov functional $\|e^F\|_2^2$, and we derive

$$\left(\|e^F(\cdot,t)\|_2^2\right)_t = 2D\int_S e^F(x,t)e_{xx}^F(x,t)\,\mathrm{d}x \\ - 2D\left[1 - \exp(-K_L t)\right]\int_S e^F(x,t)\left[e^F(x,t)\frac{\bar{\rho}_x^F(x,t)}{\bar{\rho}^F(x)}\right]_x \mathrm{d}x \\ + 2D\alpha(t)\int_S e^F(x,t)\left[e^F(x,t)\frac{\bar{\rho}_x^F(x,t)}{\bar{\rho}^F(x)}\right]_x \mathrm{d}x \\ + 2\exp(-K_L t)\int_S e^F(x,t)\left[(\bar{\rho}^F(x) - e^F(x,t))(f * \rho_0^L)(x) - D\bar{\rho}_x^F(x)\right]_x \mathrm{d}x. \quad (5.68)$$

By means of integration by parts and recalling $[(e^F)^2]_x = 2e^F e_x^F$, we can establish the identity

$$2D\alpha(t)\int_S e^F(x,t)\left[e^F(x,t)\frac{\bar{\rho}_x^F(x,t)}{\bar{\rho}^F(x)}\right]_x \mathrm{d}x = -D\alpha(t)\int_S 2e^F(x,t)e_x^F(x,t)\frac{\bar{\rho}_x^F(x,t)}{\bar{\rho}^F(x)}\,\mathrm{d}x = \\ = -D\alpha(t)\int_S \left[(e^F(x,t))^2\right]_x \frac{\bar{\rho}_x^F(x,t)}{\bar{\rho}^F(x)}\,\mathrm{d}x = D\alpha(t)\int_S (e^F(x,t))^2 g_1(x)\,\mathrm{d}x. \quad (5.69)$$

Using this identity along with those in (5.56), we obtain

$$\left(\|e^F(\cdot,t)\|_2^2\right)_t = -2D\|e_x^F(\cdot,t)\|_2^2 - D\left[1 - \exp(-K_L t) - \alpha(t)\right]\int_S (e^F(x,t))^2 g_1(x)\,\mathrm{d}x$$

$$- \exp(-K_L t) \int_S (e^F(x,t))^2 h_1(x)\, \mathrm{d}x + 2\exp(-K_L t) \int_S e^F(x,t) h_2(x)\, \mathrm{d}x. \quad (5.70)$$

With the same vein of (5.58b), we can establish the bound

$$-D\,[1 - \exp(-K_L t) - \alpha(t)] \int_S (e^F(x,t))^2 g_1(x)\, \mathrm{d}x \le D\|g_1(\cdot)\|_\infty \|e^F(\cdot,t)\|_2^2, \quad (5.71)$$

where we used the Hölder inequality and we noted that, for any choice of $\alpha(t) \in [0,1]$, $|1 - \exp(-K_L t) - \alpha(t)| < 1,\ \forall t$ Combining bound (5.71) with the bounds in (5.58), we can establish that

$$\left(\|e^F(\cdot,t)\|_2^2\right)_t \le (-2D + D\|g_1(\cdot)\|_\infty + \|h_1(\cdot)\|_\infty)\|e^F(\cdot,t)\|_2^2 + 2\|h_2(\cdot)\|_2 \exp(-K_L t)\|e^F(\cdot,t)\|_2. \quad (5.72)$$

Then, as in Th. 5.3, using Lemma 1.6, the claim is proved. ■

**Remark 5.12.** *The case* $\alpha = 0$ *coincides with the control technique studied in Section 5.5. The case* $\alpha = 1$, *when* $t \to \infty$, *puts the error system into the form of a heat equation with periodic boundary conditions.*

**Remark 5.13.** *As* $\alpha$ *is ultimately chosen to ensure that the deconvolution of* $v^{FL}$ *is physically meaningful in the sense of the constraints in Definition 5.1 (as detailed in the rest of this section), it cannot be used to improve the convergence condition in Theorem 5.4.*

Given (5.62) and (5.63), and recalling that $\hat{v}^{FL} = f * \hat{\rho}^L$, we recover the desired leaders' density $\hat{\rho}^L$ by online deconvolution [179] of $v^{FL}$ with the repulsive interaction kernel given by (5.3) (see Appendix B for more details). For the linearity of the convolution we can deconvolve the two terms of (5.63) separately, leading to

$$\hat{\rho}^L(x,t) = \bar{\rho}^L(x) + \alpha(t) W(x,t), \quad (5.73)$$

where $\bar{\rho}^L$ is the deconvolution of $\bar{v}^{FL}$ and $W$ is the deconvolution of $w$, that is,

$$W(x,t) = \frac{w_x(x,t)}{2} - \frac{1}{2L^2} \int w(x,t)\, \mathrm{d}x + \beta(t), \quad (5.74)$$

with $\beta$ being an arbitrary function of time (see Appendix B for more details). Being the problem feasible, we know that $\bar{\rho}^L$ is positive and sums to $M^L$. Then, for $\hat{\rho}^L$ to be physically meaningful, that is, positive and summing to $M^L$, $W$ needs to fulfill the following conditions:

$$\int_{\mathcal{S}} W(x,t)\,\mathrm{d}x = 0, \quad \forall t \geq 0, \tag{5.75a}$$

$$\bar{\rho}^L(x) + \alpha(t) W(x,t) \geq 0, \quad \forall t \geq 0, x \in \mathcal{S}. \tag{5.75b}$$

Condition (5.75a) can always be ensured by appropriately choosing $\beta$ in (5.74) and (5.75b) can be satisfied by selecting $\alpha$ so that it remains fulfilled, as will be shown next.

### Choice of $\alpha(t)$

A possible conservative choice is to set

$$\alpha(t) = \left[\frac{-\min_x \bar{\rho}^L(x)}{\min_x W(x,t)}\right]_0^1, \tag{5.76}$$

where subscripts and superscripts of square brackets indicate a saturation. With this choice of $\alpha(t)$, we can guarantee that

$$\min_x \bar{\rho}^L(x) + \alpha(t) \min_x W(x,t) \geq 0, \tag{5.77}$$

and therefore that (5.75b) is fulfilled. Note that in making the choice we exploited the fact that $\min_x W \leq 0$ by construction, since $\beta$ is chosen in (5.74) to ensure (5.75a). Also, notice that (5.77) (and consequently (5.75b)) remains satisfied when $\alpha$ is saturated to zero as $\bar{\rho}^L \geq 0$ by assumption, and when $\alpha$ is saturated to unity as $-\min_x \bar{\rho}^L / \min_x W > 1$ implies $|\min_x \bar{\rho}^L| > |\min_x W|$.

Other possible choices of $\alpha$, including optimal ones, are possible. A practical heuristic choice to approximate the optimal $\alpha$ and enhance robustness of the algorithm to persistent disturbances is adopted later in Section 5.7.1. A further investigation of the choice of how $\alpha$ could be optimized is beyond the scope of this paper and will be explored in future work.

**Remark 5.14.** *The reference-governor control scheme cannot be adapted to scenarios in which the feasibility analysis is not fulfilled as for the feed-forward scheme (see Appendix C.2 for more details).*

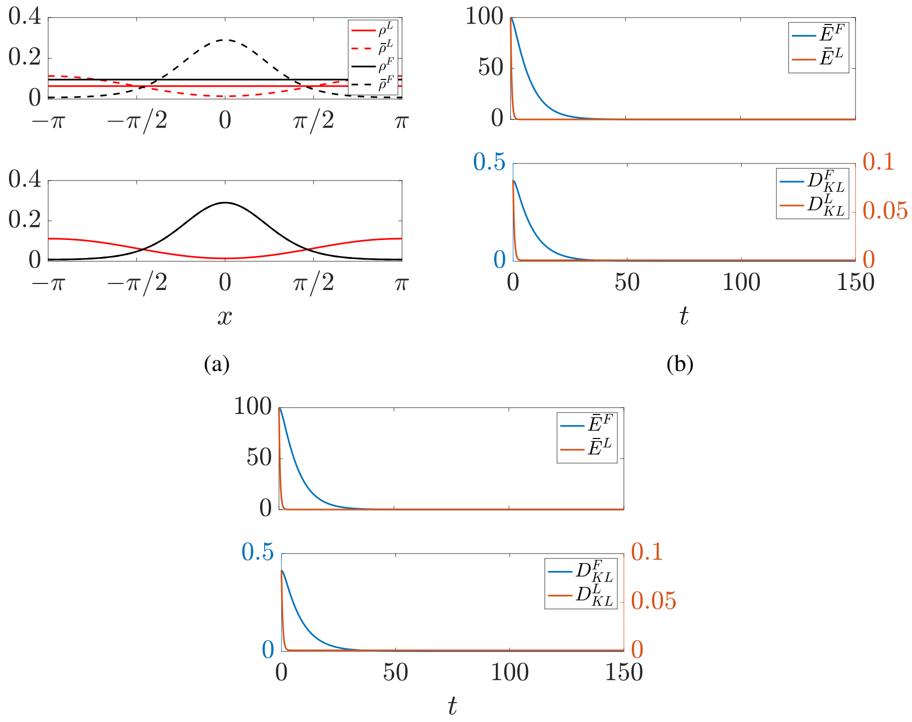

(a)

(b)

(c)

Figure 5.4: Monomodal trial: (a) initial and final densities; (b) time evolution of the percentage error and KL divergences using the feed-forward control scheme; and (c) time evolution of the percentage error, KL divergences, and $\alpha$ using the reference-governor scheme.

## 5.7 Numerical validation

In this section, we perform a numerical validation of the two proposed control strategies. For the numerical integration of (5.1a)-(5.1b), we use a central finite difference scheme with a mesh of 500 cells, and we approximate time derivatives with Forward Euler with a fixed time step $\mathrm{d}t = 0.001$.

For each trial, we consider $D = 0.05$, $L = \pi$, and a time horizon of 150,000 time iterations and recorded followers and leaders percentage error, that is,

$$\bar{E}^i(t) = \frac{\|e^i(\cdot,t)\|_2^2}{\max_t \|e^i(\cdot,t)\|_2^2}\,100, \quad i = F, L. \tag{5.78}$$

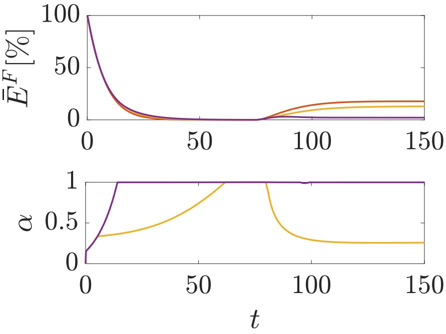

Figure 5.5: Robustness to external disturbance. Percentage error (top panel) and evolution of $\alpha$ (bottom panel) in time for the feedback control schemes (orange line for feed forwards, yellow line for reference-governor and purple line for reference-governor with an improved choice of $\alpha$).

As an extra performance index, we borrow from the optimal transport literature [93] the Kullback-Leibler (KL) divergence [169] (or relative entropy) between the desired followers' (leaders') density and the followers' (leaders) density, that is

$$D^i_{KL}(t) = \int_S \bar{\rho}^i(x) \log\left(\frac{\bar{\rho}^i(x)}{\rho^i(x,t)}\right) \mathrm{d}x, \quad i = F, L. \tag{5.79}$$

We study a monomodal regulation problem. Specifically, we set $M^L = 0.4$ and choose the von Mises distribution in (5.28) with $\kappa = 1.8$ and $\mu = 0$ for the desired followers' density. We report the results of the numerical example in Fig. 5.4. Specifically, we show the initial and final displacement of the leaders' and followers' densities, resulting in the same steady-state profile with both the control techniques. Then, in Fig. 5.4b and 5.4c (upper panel), we report the time evolution of the percentage errors and KL divergences using respectively the feed-forward and the reference-governor control schemes. In Fig. 5.4c (bottom panel), we show the time evolution of the control function $\alpha$ selected according to (5.76). Similar results were obtained for bi-modal regulation tasks but omitted here for brevity.

## 5.7.1 Robustness analysis

To underscore the benefits of the strategy incorporating the reference governor control over the simpler feed-forward control strategy, we proceed to examine the robustness of both strategies against disturbances and structural perturbations. Our findings demonstrate that, as anticipated, the strategy equipped with the reference governor control offers superior compensation for these disruptions.

### Perturbations

To begin, we consider the dynamics of the followers to be perturbed by an additive velocity field $d$, defined as

$$d(x,t) = \frac{\pi}{100}\,\mathrm{step}(t - t_\mathrm{f}/2). \tag{5.80}$$

This represents a positive constant drift which is suddenly introduced into the followers' dynamics halfway through a simulation trial.

Considering the same setting as the one depicted in Fig. 5.4 where the goal is for the followers to achieve a monomodal distribution, we applied both the feed-forward and the reference-governor schemes, observing enhanced performance with the latter (see Fig. 5.5). Specifically, as illustrated in the top panel of Fig. 5.5, the steady-state percentage residual error decreases from nearly 20% to approximately 10% with the introduction of feedback.

Performance improves more significantly, when we introduce a numerical procedure to improve the choice of $\alpha$. Specifically, as the optimal $\alpha$ (that is, the maximum value still fulfilling (5.75b)) can be formalized as

$$\alpha(t) = \lim_{\varepsilon \to 0+} \left[ \min_x \left( \frac{\bar{\rho}^L(x)}{\max[-W(x,t), \varepsilon]} \right) \right]_0^1, \tag{5.81}$$

we practically implement it by fixing $\varepsilon = 0.01$. Specifically, as $\alpha$ remains set to one for extended periods (as shown in the bottom panel of Fig. 5.5), the feedback correction intensifies, leading to a residual percentage error of only 2% despite the onset of the perturbation (as detailed in the top panel of Fig. 5.5).

### Robustness to Structural Perturbations

To evaluate robustness to structural perturbations, we assess the response to parametric uncertainties in the characteristic length scale $L$ of the interaction kernel $f$ (see (3.24)). This involves assuming a discrepancy between the nominal length scale used for control design and the actual scale influencing the followers' dynamics. Specifically, setting $D = 0.02$ and using the same monomodal configuration depicted in Fig. 5.4, we compute $u$ in (5.1a) using the nominal value $L = \pi$ for both the feed-forward and

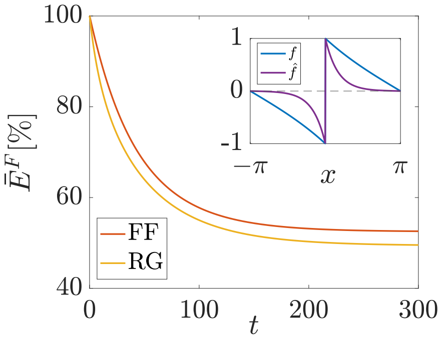

Figure 5.6: Robustness to uncertainties: time evolution of the percentage error with the feed-forward (FF) control scheme and the reference-governor (RG) control scheme. In the inset, the nominal and perturbed interaction kernel.

reference-governor schemes. Conversely, in the numerical simulations, the followers are assumed to react to the leaders' displacement through a perturbed kernel $\hat{f}$, defined as (3.24) with $L = \pi/6$. The results of this trial, along with graphical representations of both the nominal and perturbed kernels, are presented in Fig. 5.6. We find that that the reference-governor scheme enhances steady-state performance, reducing the steady-state percentage error to almost 45% as compared to 55% observed when the feed-forward scheme is adopted. We did not document the time evolution of $\alpha$ because, adhering to the conservative approach outlined in Section 5.6.1, we fixed it at 1 throughout the trial.

Note that, in the presence of parametric uncertainties on the diffusion coefficient $D$ (omitted here for brevity), the behavior of both the feed-forward and reference-governor schemes remains qualitatively similar. This similarity arises because the feedback action $w$ is not independent of $D$, as illustrated in (5.64).

## 5.8 An application to multi-agent leader-follower systems via continuification

Within the framework of continuification-based control approaches disucssed in Chapter 3 the goal is to design microscopic control inputs to influence the spatio-temporal dynamics of large-scale multi-agent systems.

To validate the macroscopic control solution proposed in this work, we consider a discrete set of stochastic differential equations that replicate the leader-follower scenario previously examined. In particular, we assume a population of $N^L$ leaders needs to steer

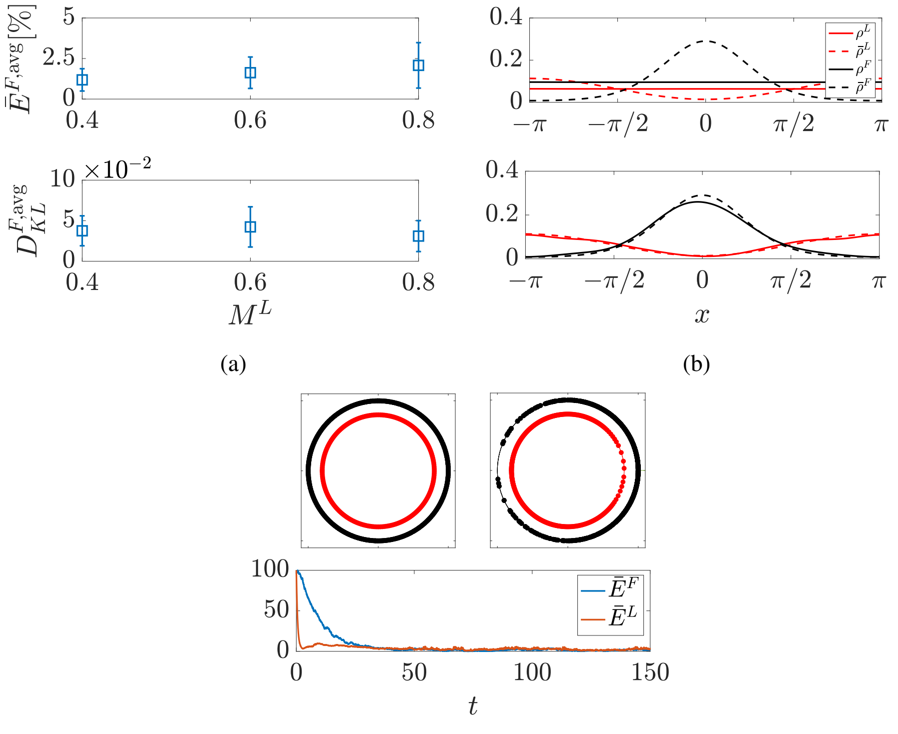

(a) (b)

(c)

Figure 5.7: Discrete trial: (a) average followers' percentage (± one standard deviation) error and KL divergence for different values of the leaders' mass; (b) initial and final densities for a single trial ($N^L = 400$); (c)-(upper panel) initial and final agents displacements in $\mathcal{S}$ for a single trial ($N^L = 400$); and (c)-(lower panel) percentage error of leaders and followers in time for a single trial ($N^L = 400$).

the dynamics of a population of $N^F$ followers. We consider the two populations move in $\mathcal{S}$ and, as often assumed in the literature [17], we set their dynamics according to

$$\dot{x}_i^L = u_i, \; i = 1, \dots, N^L \tag{5.82a}$$

$$\mathrm{d}x_k^F = \frac{N^L}{N^L + N^F} \sum_{j=1}^{N^L} f(\{x_k^F, x_j^L\})\, \mathrm{d}t + \sqrt{2D}\mathrm{d}B_k, \; k = 1, \dots, N^F, \tag{5.82b}$$

where $B_k$ is a standard Wiener process. Such a formulation represents the discrete counterpart of (5.1a)-(5.1b) [130]. Following our solution, and in the context of a continuification scheme, we can perform a discretization and fix the microscopic control inputs of the leaders $u_i$ in (5.82) as

$$u_i(t) = u(x_i, t), \quad i = 1, \ldots, N^L, \tag{5.83}$$

with $u$ coming from (5.44), and considering the reference governor scheme proposed in Section 5.6.

We consider the discrete counterpart of the numerical setup discussed in Section 5.7. Specifically, we set $D = 0.05$, $L = \pi$, $K_L = 1$, and simulate a total of $N^L + N^F = 1000$ agents. For the desired followers' density, we adopt the monomodal von Mises distribution utilized in the trial depicted in Fig. 5.4. Agent densities are estimated from their positions using an ad-hoc Gaussian kernel estimation method [168], and numerical integration is performed using the forward Euler method for leaders and the Euler-Maruyama method for followers, with a time step of $\Delta t = 0.001$.

We fix the initial densities of both populations to be constant and conduct $n = 128$ trials, each consisting of 150,000 time steps, while exploring different feasible ratios of leaders to followers. We characterize this numerical investigation by calculating the average over the $n$ trials of the steady-state percentage error and KL divergence. Specifically, results are depicted in Fig. 5.7a, where it is evident that we consistently reduce the percentage error to well below 5% – a performance level also corroborated by the KL divergence of the followers. For completeness, Fig. 5.7b and 5.7c also present the outcomes of a single trial with $N^L = 400$, in terms of densities, agents' displacements, and percentage error.

Contrary to the macroscopic simulations performed using the continuum formulation in Section 5.7, we register a small steady-state error in the discrete model. This error primarily arises from two factors: the finite size of the swarm, which challenges the validity of the continuum hypothesis, and the stochastic behavior of the followers.

## 5.9 Extension to higher dimensions

Our one-dimensional framework can be readily extended to higher dimensions. Specifically, assuming the spatial domain to be $\Omega := [-\pi, \pi]^d$ (with $d = 2, 3$), in $H^2(\Omega)$, the model becomes

$$\rho_t^L(\mathbf{x}, t) + \nabla \cdot \left[\rho^L(\mathbf{x}, t)\mathbf{u}(\mathbf{x}, t)\right] = 0, \tag{5.84a}$$

$$\rho_t^F(\mathbf{x}, t) + \nabla \cdot \left[\rho^F(\mathbf{x}, t)\mathbf{v}^{FL}(\mathbf{x}, t)\right] = D\nabla^2\rho^F(\mathbf{x}, t), \tag{5.84b}$$

where $\nabla \cdot (\cdot)$ and $\nabla^2(\cdot)$ are the divergence and Laplacian operators, respectively, $\mathbf{x} \in \Omega$, $\mathbf{u}$ is the control input to design, and

$$\mathbf{v}^{FL}(\mathbf{x},t) = \int_\Omega \mathbf{f}(\{\mathbf{x},\mathbf{y}\})\rho^L(\mathbf{y},t)\,\mathrm{d}\mathbf{y} = (\mathbf{f} * \rho^L)(\mathbf{x},t), \tag{5.85}$$

is the circular convolution of $\rho^L$ with $\mathbf{f}$, that is the $d$-dimensional repulsive interaction kernel.

**Remark 5.15.** *Notice that a closed form expression for* $\mathbf{f}$ *was not found. The periodized kernel can be expressed as an infinite series (see* (A.1) *for the one-dimensional counterpart), which can be truncated for implementation purposes.*

Similarly to the one-dimensional case, to ensure mass is conserved, $\rho^F$ and $\rho^L$ are assumed to be periodic on $\partial\Omega$, and initial conditions are set similarly to (5.5) and (5.7). Moreover, the total masses of leaders and followers are such that $M^F + M^L = 1$.

### 5.9.1 Feasibility analysis

Given the problem statement in Section 5.3, we seek the desired velocity field for the followers by assuming that $\bar{\rho}^F$ solves (5.84b) at steady-state

$$\nabla \cdot \left[\bar{\rho}^F(\mathbf{x})\bar{\mathbf{v}}^{FL}(\mathbf{x})\right] = D\nabla^2\bar{\rho}^F(\mathbf{x}). \tag{5.86}$$

Unlike the one-dimensional case, this scalar relation alone does not suffice to uniquely determine the vectorial field $\bar{\mathbf{v}}^{FL}$. Thus, following the approach in Sec. 3.4.3 of Chapter 3, we define $\mathbf{w} = \bar{\rho}^F\bar{\mathbf{v}}^{FL}$ and impose an irrotationality condition, leading to

$$\begin{cases} \nabla \cdot \mathbf{w}(\mathbf{x}) = D\nabla^2\bar{\rho}^F(\mathbf{x}), \\ \nabla \times \mathbf{w}(\mathbf{x}) = 0, \end{cases} \tag{5.87}$$

with periodic boundary conditions applied to $\mathbf{w}$ (we refer to [42] – Sec. 1.2.5, example 1.5 – for details about how the curl is computed in two-dimensions). Being $\mathbf{w}$ irrotational and $\Omega$ simply connected, we conclude that $\mathbf{w} = -\nabla\varphi$, where $\varphi$ is an unknown scalar potential.

Using this expression of $\mathbf{w}$, equation (5.87) simplifies into the Poisson equation

$$\nabla^2\varphi(\mathbf{x}) = -D\nabla^2\bar{\rho}^F(\mathbf{x}) \tag{5.88}$$

which is fulfilled choosing $\varphi = -D\bar{\rho}^F$. With this definition of $\mathbf{w}$ and $\varphi$, we obtain

$$\bar{\mathbf{v}}^{FL}(\mathbf{x}) = D\frac{\nabla\bar{\rho}^F(\mathbf{x})}{\bar{\rho}^F(\mathbf{x})}, \tag{5.89}$$

which is the $d$-dimensional extension of (5.14). With the additional irrotationality constraint of the flux $\mathbf{w}$, the higher-dimensional formulation is analogous to the one-dimensional one.

Recalling that $\bar{\mathbf{v}}^{FL} = \mathbf{f} * \bar{\rho}^L$, we derive $\bar{\rho}^L$ by deconvolution,

$$\bar{\rho}^L(\mathbf{x}) = H(\mathbf{x}) + A, \tag{5.90}$$

where $A$ is an arbitrary constant. This deconvolution of $\bar{\rho}^L$ is defined up to an arbitrary constant due to the linearity of the convolution operator and the assumption that the kernel is odd. Unlike the one-dimensional case, where $\mathbf{f}$ has a closed form, $H$ can only be computed numerically [179]. Consequently, the feasibility problem is reformulated in terms of the constant $A$.

**Proposition 5.1.** *The problem outlined by* (5.84a), (5.84b)*, and* (5.9) *admits a feasible solution if there exists a value of $A$ in* (5.90) *such that*

$$\bar{\rho}^L(\mathbf{x}) \geq 0, \tag{5.91a}$$

$$\int_\Omega \bar{\rho}^L(\mathbf{x})\,\mathrm{d}\mathbf{x} = M^L. \tag{5.91b}$$

Proposition 5.1 can be evaluated numerically in straightforward steps. One can set $A = a_1 + a_2$ in (5.90), with $a_1$ chosen to minimize its integral, that is, $a_1 = -\min_{\mathbf{x}} H$. Then, assuming $a_2 \geq 0$, (5.91a) is automatically fulfilled, and, if there exists some $a_2$ fulfilling (5.91b), feasibility is guaranteed.

### 5.9.2 Control design

Assuming that the feasibility condition is met, we now extend the reference-governor scheme, which includes the feed-forward strategy, to higher dimensions. We detail the controller for the leaders in higher dimensions, and, subsequently, we examine the governor loop.

### *Leaders control*

The leaders' control is tasked with guiding $\rho^L$ toward some desired time-varying leaders' density $\hat{\rho}^L$. This control can be straightforwardly derived following the method outlined in Section 5.5.1. Specifically, one can choose

$$\nabla \cdot \left[\rho^L(\mathbf{x},t)\mathbf{u}(\mathbf{x},t)\right] = -\hat{\rho}^L_t(\mathbf{x},t) - K_L e^L(\mathbf{x},t). \tag{5.92}$$

This formulation ensures that

$$e^L_t(\mathbf{x},t) = -K_L e^L(\mathbf{x},t), \tag{5.93}$$

thereby proving point-wise exponential convergence. To explicitly recover $\mathbf{u}$, the curl condition can be added

$$\nabla \times \left[\rho^L(\mathbf{x},t)\mathbf{u}(\mathbf{x},t)\right] = 0, \tag{5.94}$$

and the problem can then be treated similarly to the approach in [31], where it is recast as a Poisson equation and solved using Fourier series. The periodicity of $\mathbf{u}$, and consequently the conservation of the leaders' mass, is ensured by the same argument used in Section 5.5.1, namely,

$$\int_\Omega \left[-\hat{\rho}^L_t(\mathbf{x},t) - K_L e^L(\mathbf{x},t)\right] \,\mathrm{d}\mathbf{x} = 0. \tag{5.95}$$

### *Governor design*

Under the control action (5.92), the leaders' behavior obeys to

$$\rho^L(\mathbf{x},t) = \hat{\rho}^L(x,t) + \Phi(\mathbf{x},t), \tag{5.96}$$

where $\hat{\rho}^L$ is some desired time-varying density and $\Phi$ represents the transient behavior, given by

$$\Phi(\mathbf{x},t) = -\left[\hat{\rho}^L(\mathbf{x},0) + \rho^L_0(\mathbf{x})\right]\exp(-K_L t). \tag{5.97}$$

Hence $\mathbf{v}^{FL}$ in (5.85) can be decomposed as

$$\mathbf{v}^{FL}(\mathbf{x},t) = \hat{\mathbf{v}}^{FL}(\mathbf{x},t) + (\mathbf{f} * \Phi)(\mathbf{x},t), \tag{5.98}$$

where $\hat{\mathbf{v}}^{FL} = \mathbf{f} * \hat{\rho}^L$. In what follows, we recover an expression for $\hat{\mathbf{v}}^{FL}$ that can be proved to asymptotically achieve the control problem. Such an expression will be finally deconvolved to recover $\hat{\rho}^L$ for the leaders to track.

We set the following expression for the velocity field:

$$\hat{\mathbf{v}}^{FL}(\mathbf{x}, t) = \bar{\mathbf{v}}^{FL}(\mathbf{x}) + \alpha(t)\mathbf{w}(\mathbf{x}, t), \tag{5.99}$$

where $\bar{\mathbf{v}}^{FL}$ is derived from (5.89). Here, $\alpha(t) \in [0, 1]$ is a control function to be determined, and

$$\mathbf{w}(\mathbf{x}, t) = \frac{D\nabla\bar{\rho}^F(\mathbf{x})e^F(\mathbf{x}, t)}{\bar{\rho}^F(\mathbf{x})(\bar{\rho}^F(\mathbf{x}) - e^F(\mathbf{x}, t))}. \tag{5.100}$$

defines the additional feedback term adjusted by $\alpha(t)$.

Substituting (5.98) into (5.84b) (accounting for (5.99) and (5.100)) and expressing the equation in terms of the error $e^F$, we derive

$$\begin{aligned} e^F_t(\mathbf{x}, t) = D\nabla^2 e^F(\mathbf{x}, t) - D\left[1 - \exp(-K_L t) - \alpha(t)\right] \nabla \cdot \left[e^F(\mathbf{x}, t)\frac{\nabla\bar{\rho}^F(\mathbf{x}, t)}{\bar{\rho}^F(\mathbf{x}, t)}\right] \\ + \exp(-K_L t)\nabla \cdot \left[\left(\bar{\rho}^F(\mathbf{x}, t) - e^F(\mathbf{x}, t)\right)(\mathbf{f} * \rho^L_0)(\mathbf{x}) - D\nabla\bar{\rho}^F(\mathbf{x})\right]. \end{aligned} \tag{5.101}$$

**Theorem 5.5.** *In a feasible scenario according to Proposition 5.1, (5.101) converges to 0 in $\mathcal{L}^2$, if*

$$K^{rgh} = -2D + D\|G_1(\cdot)\|_\infty + \|H_1(\cdot)\|_\infty < 0 \tag{5.102}$$

*with*

$$G_1(\mathbf{x}) = \nabla \cdot \left[\frac{\nabla\bar{\rho}^F(\mathbf{x})}{\bar{\rho}^F(\mathbf{x})}\right], \tag{5.103}$$

$$H_1(\mathbf{x}) = \nabla \cdot \left[(\mathbf{f} * \rho^L_0)(\mathbf{x})\right]. \tag{5.104}$$

*If $K_L \gg |K^{rgh}|$, the rate of convergence of the error is upper bounded by $K^{rgh}$.*

*Proof.* Choosing $\|e^F\|_2^2$ as a Lyapunov functional for (5.101), we obtain

$$\begin{aligned} \left(\|e^F(\cdot, t)\|_2^2\right)_t = 2D\int_\Omega e^F(\mathbf{x}, t)\nabla^2 e^F(\mathbf{x}, t)\,\mathrm{d}\mathbf{x} \\ - 2D\left[1 - \exp(-K_L t) - \alpha(t)\right]\int_\Omega e^F(\mathbf{x}, t)\nabla \cdot \left[e^F(\mathbf{x}, t)\frac{\nabla\bar{\rho}^F(\mathbf{x})}{\bar{\rho}^F(\mathbf{x})}\right]\mathrm{d}\mathbf{x} \end{aligned}$$

$$+ 2\exp(-K_L t) \int_\Omega e^F(\mathbf{x},t)\nabla \cdot \left[\left(\bar{\rho}^F(\mathbf{x},t) - e^F(\mathbf{x},t)\right)(\mathbf{f} * \rho_0^L)(\mathbf{x}) - D\nabla\bar{\rho}^F(\mathbf{x})\right] \mathrm{d}\mathbf{x}. \tag{5.105}$$

Utilizing vectorial identities and the divergence theorem, this can be simplified to

$$\begin{aligned}\left(\|e^F(\cdot,t)\|_2^2\right)_t &= -2D\|\nabla e^F(\cdot,t)\|_2^2 - D\left[1-\exp(-K_L t)-\alpha(t)\right]\int_\Omega (e^F(\mathbf{x},t))^2 G_1(\mathbf{x})\,\mathrm{d}\mathbf{x}\\ &- \exp(-K_L t)\int_\Omega (e^F(\mathbf{x},t))^2 H_1(\mathbf{x})\,\mathrm{d}\mathbf{x} + 2\exp(-K_L t)\int_\Omega e^F(\mathbf{x},t)H_2(\mathbf{x})\,\mathrm{d}\mathbf{x},\end{aligned} \tag{5.106}$$

where $H_2 = \nabla \cdot (\bar{\rho}^F(\mathbf{f} * \rho_0^L) - D\nabla\bar{\rho}^F)$. By exploiting bounds similar to those derived for Theorem 3 and 4, we can establish

$$\begin{aligned}\left(\|e^F(\cdot,t)\|_2^2\right)_t \le \left[-2D + D\|G_1(\cdot)\|_\infty + \|H_1(\cdot)\|_\infty\right]\|e^F(\cdot,t)\|_2^2&\\ + 2\|H_2(\cdot)\|_2 \exp(-K_L t)\|e^F(\cdot,t)\|_2.&\end{aligned} \tag{5.107}$$

Under the theorem hypothesis, the bounding system is in the form discussed in Lemma 1.6, making the theorem proved. ■

Convergence is ensured for any $\alpha \in [0,1]$. The case where $\alpha = 0$ for all $t \geq 0$ coincides with the feed-forward scheme proposed in the one-dimensional case. By performing a deconvolution of $\mathbf{v}^{FL}$, we derive

$$\hat{\rho}^L(\mathbf{x},t) = \bar{\rho}^L(\mathbf{x}) + \alpha(t)W(\mathbf{x},t), \tag{5.108}$$

where $\bar{\rho}^L$ comes from (5.90) and $W$ represents the deconvolution of (5.100), expressed as:

$$W(\mathbf{x},t) = Q(\mathbf{x}) + \beta(t), \tag{5.109}$$

with $\beta(t)$ being an arbitrary time-dependent function.

Note that the deconvolution $W$ is defined up to an arbitrary function of time due to the linearity of the convolution operator and the assumption that the kernel is odd. Consequently, the computation of $Q$ must be performed numerically, as no closed form for the periodic kernel in higher dimensions has been established. Similarly, to the

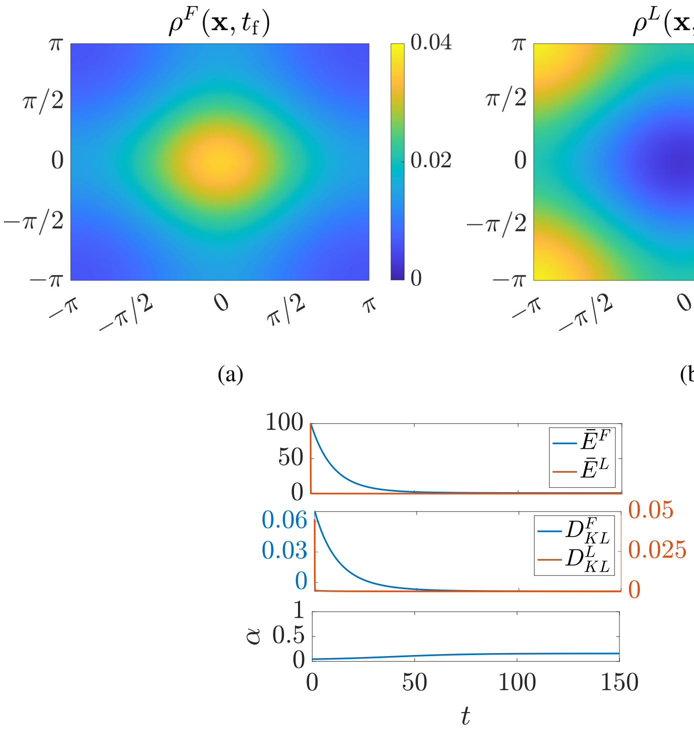

(a)

(b)

(c)

Figure 5.8: Monomodal trial in 2D: (a) followers' density at the end of the trial; (b) leaders' density at the end of the trial; and (c) time evolution of the percentage error (top panel), KL divergences (middle panel), and $\alpha$ (bottom panel).

one-dimensional case, $\alpha$ and $\beta$ can be selected such that

$$\int_\Omega W(\mathbf{x}, t)\, \mathrm{d}\mathbf{x} = 0, \quad \forall t \geq 0 \tag{5.110a}$$

$$\bar{\rho}^L(\mathbf{x}) + \alpha(t) W(\mathbf{x}, t) \geq 0, \quad \forall t \geq 0. \tag{5.110b}$$

For choosing $\alpha$, the same rationale used in Section 5.6.1 can be applied.

### 5.9.3 Numerical validation

For validation, we extended the trial depicted in Fig. 5.4 from one to two dimensions. Specifically, we set $D = 0.05$, $M^F = 0.6$, and $K_L = 10$. For the desired followers' density, we adopted the two-dimensional version of (5.28) – see Equation (25) in [31] for an explicit formula – with the concentration coefficients in each direction set at $k_1 = k_2 = 0.5$. This configuration satisfied the feasibility condition.

Using the reference-governor scheme and selecting $\alpha$ as outlined in Section 5.6.1, we numerically integrated (5.84b) and (5.84a) using a central finite difference scheme on a 50×50 mesh. The forward Euler method was employed to estimate time derivatives, with a time step of $\mathrm{d}t = 0.01$. Starting from a constant initial density for both populations, we observed the results shown in Fig. 5.8. Both the percentage errors and KL divergences converged to zero within approximately 50 time units, and the weighting factor $\alpha$, which adjusts the amplitude of the feedback correction, stabilized at about 0.2.

## 5.10 Discussion

We developed a continuum framework to address the leader-follower density control problem within large-scale multi-agent systems. We assumed followers to be random walkers at the microscopic scale, based on a number of studies supporting such a microscopic model for engineering applications.

We established criteria for assessing the problem's feasibility, leveraging information about the number of reactive leaders in the group, the desired followers' density, the interaction kernel scale, and the followers' dynamics. Both the proposed control architectures ensure global exponential stability towards a desired spatial organization, for one and multi-dimensional domains. Differently from relevant literature [60, 130], we provided closed forms for the macroscopic control actions and useful bounds for the rate of convergence.

Although convergence is ensured in the limiting scenario of infinite populations, we demonstrated a straightforward methodology to apply our macroscopic control action to swarm of finite size, taking inspiration from [29, 30, 31]. We emphasize that analytical guarantees of convergence when such a discretization of the continuum control action is performed, are still missing. Such guarantees could be explored using classical works about two-scale convergence [181] and asymptotic formal analysis [182].

This is not the only limitation of the study that calls for future research. In fact, future work should aim at (*i*) overcoming the kinematic assumption that is used to model the populations' motion as mass conservation laws; (*ii*) accounting for topological and networked interactions, through, for example, the use of graphons [100]; (*iii*) introducing in the model interactions taking place between followers; (*iv*) analytically study the different robustness properties of the two control schemes we propose, which here were only numerically addressed; and (*v*) proposing an experimental, localized and distributed validation of the strategies within the mixed-reality framework described in [31] – in so doing, local density estimation methods need to be exploited [183].

Despite these limitations, the proposed work makes contributions to the theory of density-control of large ensembles that are expected to find application in critical engineering areas such as traffic control and swarm robotics, and opens the door to mathematical treatment of control problems in continuum models describing heterogeneous teams.

# 6 Reacting Mixtures of Leaders and Followers

In this Chapter, we expand the theoretical framework we developed in Chapter 5 to reacting mixtures of leaders and followers. In particular, we consider a scenario where agents can switch between being leaders or followers while solving a density control problem. This set-up is framed within the biological mechanism of behavioral plasticity, that is, the tendency of individuals to modify their behavior when appropriately stimulated. This leads to a more profound comprehension of plasticity phenomena and shows a possible direction to inspire new, more robust and flexible, control solution for swarms of agents.

## 6.1 Introduction

Leadership is the capability to foster and speed-up the emergence of *distributed intelligence* [184]. Through the lenses of complex systems theory, this behavior is perceived through the actions of *special* individuals (i.e., agents), who are willing to create conditions enabling productive future states [185].

Leadership emergence is largely observed across different animal species. Pigeons' homing maneuvers are driven by those individuals exhibiting better flight characteristics [186]. Fish schooling, which has often been considered as caused by egalitarian self-organization [187], is a prototypical example where the role of leaders is crucial to perform predators avoidance and energy saving [188]. Moreover, it is observed in human networks performing motor coordination tasks [10].

Sometimes, the tendency to become a leader is DNA-encoded. This is, for example, the case of clown-fish, in which the school organization is delegated to the only female specimen in the group. Females are larger than males, and, when a leader dies, the strongest male in the school transforms itself into a female and become the new leader [189].

In many other cases, individuals can become leaders because of some specific state they experience while being followers [190]. For example, fish exiting the follower state to become leaders, may be due to knowledge about food's or predators' location [191, 192]. Similarly, in pedestrian groups, becoming the individual driving the crowd coincides with being on the border of the formation at the right time [115]. Moreover, we point out that leading a group during a collective task is necessarily associated with a higher energetic expenditure and exposes to possible risks (as that of predators). This points at the necessity for individuals of alternating between being a leader and a follower.

Under this perspective, being leaders or followers is not an irreversible condition, and roles' switching is a crucial mechanism to increase performance and reduce the cost and risk associated with leading roles. The biological mechanism underlying this switching is typically referred as *behavioral plasticity* [193], that is a possible declination of phenotypic plasticity [194]. It refers to changes in an organism behavior resulting from exposure to external and internal stimuli.

We point out that many papers in the existing Literature have been devoted to designing solutions for control applications and swarm robotics driving inspiration from this leader-follower paradigm [195]. Interestingly, within this context, the amount of work accounting for behavioral plasticity mechanisms is consistently less [196]. In the perspective work [197], it is pointed out that implementing plasticity in robots' swarms may be a viable option to face the high unpredictability of real world applications and embed agents with the necessary flexibility to accomplish a wide spectrum of tasks.

In this Chapter, we develop a simple continuum model for a large population of agents solving a density control problem, while undergoing a behavioral plasticity mechanism. Our model takes inspiration from the Literature about reacting mixtures [176], as we decided to model plasticity as a chemical reaction taking place between two fluids. In particular, we expand the model we presented in Chapter 5 to describe three subgroups of agents, that are, leaders, followers and non-reactive followers. All the agents interact between themselves, and (*i*) leaders can be directly controlled and eventually transform into followers, (*ii*) followers can eventually transform into leaders, and (*iii*) non-reactive followers remain followers being subject only to the interactions with the rest of the group. This spectrum of roles let us distinguish between agents which are willing to take leadership and those which only passively follow the group behavior.

We derive a necessary and sufficient condition for the density control problem to admit a solution, and we link it to important quantities needed to achieve the desired goal.

These include the amount of non-reactive followers, the interaction kernel parameters, the desired density, and the diffusivity of the agents. After formulating the problem, we prove local convergence of the proposed control strategy towards the desired behavior. We also provide some preliminary results about robustness properties at for different levels of plasticity.

The rest of the Chapter is organized as follows. In Section 6.2 we study the problem over one-dimensional periodic domains. In particular, in Section 6.2.1 we present our model, in Section 6.2.2 we pose the problem statement, and in Section 6.2.3 we present our solution and run the stability analysis. The theoretical framework is then expanded to higher-dimensional periodic domains in Section 6.2.4. All the results are complemented by numerical examples. Moreover, in Sec. 6.4, we give some preliminary numerical results about robustness to parametric uncertainty for different levels of plasticity.

## 6.2 One-dimensional setting

We start by considering a one-dimensional setting.

### 6.2.1 The model

We model a population of behaviorally plastic agents using the mathematical framework of reacting mixtures [176]. Specifically, we consider three convection diffusion equations on $\mathcal{S}$, that are

$$\rho_t^L(x,t) + \left[\rho^L(x,t)u(x,t)\right]_x + \left[\rho^L(x,t)(f*\rho)(x,t)\right]_x = D\rho_{xx}^L(x,t) + q(x,t) \quad (6.1a)$$

$$\rho_t^F(x,t) + \left[\rho^F(x,t)(f*\rho)(x,t)\right]_x = D\rho_{xx}^F(x,t) - q(x,t), \quad (6.1b)$$

$$\eta_t^F(x,t) + \left[\eta^F(x,t)(f*\rho)(x,t)\right]_x = D\eta_{xx}^F(x,t). \quad (6.1c)$$

These equations model the spatio-temporal dynamics of the density of three subsets of agents. Respectively:

- *leaders* (whose density is $\rho^L : \mathcal{S} \times \mathbb{R}_{\geq 0} \to \mathbb{R}_{\geq 0}$): they (*i*) react to the rest of the group, (*ii*) can be controlled through the velocity field $u : \mathcal{S} \times \mathbb{R}_{\geq 0} \to \mathbb{R}$, and (*iii*) can eventually become followers thanks to the reacting mechanism $q : \mathcal{S} \times \mathbb{R}_{\geq 0} \to \mathbb{R}$;

- *followers* (whose density is $\rho^F : \mathcal{S} \times \mathbb{R}_{\geq 0} \to \mathbb{R}_{\geq 0}$): they (*i*) react to the rest of the population, and (*ii*) can become leaders thanks to the reacting mechanism $q$;

- *non-reactive followers* (whose density is $\eta^F : \mathcal{S} \times \mathbb{R}_{\geq 0} \to \mathbb{R}_{\geq 0}$): they only react to the rest of the population.

We consider all the agents interact among themselves through a periodic interaction kernel $f$ (fulfilling the same constraints we considered in the previous chapters), and we model it through the cross convectional term involving $\rho = \rho^L + \rho^F + \eta^F$. We also consider all the populations are influenced by a diffusion term, weighted by the diffusion coefficient $D$, modeling noise taking place at the microscopic scale.

By summing (6.1a), (6.1b) and (6.1c), we find the dynamics of the density of the whole population, that is

$$\rho_t(x,t) + \left[\rho^L(x,t)u(x,t)\right]_x + [\rho(x,t)(f * \rho)(x,t)]_x = D\rho_{xx}(x,t), \tag{6.2}$$

which, we remark, is independent from the reacting term $q$. By fixing periodic boundary conditions for (6.1a), (6.1b) and (6.1c), that is

$$\rho^L(-\pi,t) = \rho^L(\pi,t), \ \forall t \in \mathbb{R}_{\geq 0}, \tag{6.3a}$$

$$\rho^F(-\pi,t) = \rho^F(\pi,t), \ \forall t \in \mathbb{R}_{\geq 0}, \tag{6.3b}$$

$$\eta^F(-\pi,t) = \eta^F(\pi,t), \ \forall t \in \mathbb{R}_{\geq 0}, \tag{6.3c}$$

we can ensure the total population mass is conserved. In particular, we have

$$\left(\int_{\mathcal{S}} \rho(x,t)\,\mathrm{d}x\right)_t = -\left[\rho^L(x,t)u(x,t)\right]_{-\pi}^{\pi} - [\rho(x,t)(f * \rho)(x,t)]_{-\pi}^{\pi} + D\,[\rho_x]_{-\pi}^{\pi} = 0, \tag{6.4}$$

because of periodicity. Notice that (6.1c) is also conservative on its own with respect to the mass, but the same does not hold for (6.1a) and (6.1b), which are affected by the reacting term $q$. We remark that if $\int_{\mathcal{S}} q\,\mathrm{d}x$ is equal to 0, there is no net mass transfer between leaders and followers.

For simplicity we normalize the total mass to unity by setting

$$\int_{\mathcal{S}} \rho(x,t)\,\mathrm{d}x = M = M^L(t) + M^F(t) + \Phi^F = 1, \tag{6.5}$$

where $M$ is the total mass of the group, $M^L$ is the leaders' mass, $M^F$ is the followers' mass, and $\Phi^F$ is the mass of non-reactive followers (it is time-invariant as the dynamics of $\eta^F$ is not affected by the reacting term). We define

$$p = 1 - \Phi^F, \tag{6.6}$$

as the *degree of plasticity* of the system, quantifying the ratio of the whole population that can be engaged in the reaction mechanism.

Equations (6.1) are also complemented by the following initial conditions

$$\rho^L(x,0) = \rho_0^L(x), \tag{6.7a}$$
$$\rho^F(x,0) = \rho_0^F(x), \tag{6.7b}$$
$$\eta^F(x,0) = \eta_0^F(x). \tag{6.7c}$$

## 6.2.2 Problem statement

We consider the problem of choosing $u$ and $q$ in (6.1) so that the population's density asymptotically converges towards a desired time-invariant density profile, say $\bar{\rho}$, that is

$$\lim_{t\to\infty} \|\bar{\rho}(x) - \rho(x,t)\|_2 = 0. \tag{6.8}$$

As an additional specification, we assume we want to reduce the steady-state mass of leaders, so as to reduce the computational effort devoted to their control.

## 6.2.3 Control design

### *Velocity field*

Let us define the error function

$$e(x,t) = \bar{\rho}(x) - \rho(x,t). \tag{6.9}$$

Using (6.2), we find that the error dynamics is given by

$$e_t(x,t) = \left[\rho^L(x,t)u(x,t)\right]_x + [\rho(x,t)(f*\rho)(x,t)]_x - D\rho_{xx}(x,t), \tag{6.10}$$

with periodic boundary conditions and initial conditions which can be derived from those of (6.1a), (6.1b), (6.1c).

**Theorem 6.1** (Global exponential convergence)**.** *If $\rho^L > 0$ for any $x \in \mathcal{S}$ and $t \in \mathbb{R}_{\geq 0}$,* *choosing u in* (6.1a) *from*

$$\left[\rho^L(x,t)u(x,t)\right]_x = -Ke(x,t) - [\rho(x,t)(f*\rho)(x,t)]_x + D\rho_{xx}(x,t), \tag{6.11}$$

*where $K > 0$ is a control gain, makes the error dynamics globally, exponentially convergent to 0 point-wisely in $\mathcal{S}$, that is*

$$e(x,t) = e(x,0)\exp\{-Kt\}. \tag{6.12}$$

*Proof.* Substituting (6.11) in (6.10), it results

$$e_t(x,t) = -Ke(x,t), \tag{6.13}$$

which is linear and not involving spatial derivatives. Its analytical solution yields to (6.12). ■

**Remark 6.1.** *We remark that u can be found by the spatial integration of* (6.11)*, as*

$$u(x,t) = \frac{1}{\rho^L(x,t)}\left[-K\int e(x,t)\,\mathrm{d}x - \rho(x,t)(f*\rho)(x,t) + D\rho_x\right], \tag{6.14}$$

*thus making it well-defined only if $\rho^L > 0$. We also remark that, via arguments similar to those in Corollary 5.1, u can be proved to be periodic.*

**Remark 6.2.** *Under the hypothesis of theorem 6.1, and from* (6.12)*, it results*

$$\rho(x,t) = \bar{\rho}(x)\,[1-\exp\{-Kt\}] + \rho_0(x)\exp\{-Kt\}, \tag{6.15}$$

*where $\rho_0 = \rho^L_0 + \rho^F_0 + \eta^F_0$.*

**Remark 6.3.** *The hypothesis about the strict positivity of $\rho^L$ in Theorem 6.1 can be easily fulfilled in microscopic scenarios, where densities are estimated from the agents' positions using kernel estimation methods that can be chosen by the designer. For the hypothesis to hold in the macroscopic framework we are considering, we can design the reacting term q accordingly.*

### *Reacting term*

Here, we design the reacting term $q$ in (6.1a) and (6.1b). Our design is driven by two main reasons, ($i$) to ensure the hypothesis about the strict positivity of $\rho^L$ in Theorem 6.1 holds and ($ii$) to achieve a desired leaders-to-followers' mass ratio.

We choose the reacting term $q$ in (6.1a) and (6.1b) as

$$q(x,t) = \frac{1}{2}\left[\rho^L(x,t)u(x,t)\right]_x + \frac{1}{2}\left[\rho^*(x,t)(f*\rho)(x,t)\right]_x - \frac{D}{2}\rho^*_{xx}(x,t) + g(x,t), \tag{6.16}$$

where

$$\rho^*(x,t) = \rho^L(x,t) - \rho^F(x,t), \tag{6.17}$$

and $g$ obeys to the mass action law

$$g(x,t) = K_{FL}\rho^F(x,t) - K_{LF}\rho^L(x,t), \tag{6.18}$$

with $K_{LF}, K_{FL} > 0$ being the rates of the reaction.

**Theorem 6.2** (Strict positivity of $\rho^L$ and $\rho^F$ at steady-state)**.** *Choosing $u$ as in* (6.11) *and $q$ as in* (6.16)*, there exists a steady-state solution for* (6.1) *with $\bar{\rho}^L, \bar{\rho}^F > 0$ and $\bar{\eta}^F \geq 0$ for any $x \in \mathcal{S}$, if and only if*

$$\Phi^F < \min_x \left\{ \bar{\rho}(x) \frac{\int_{\mathcal{S}} h(x)\,\mathrm{d}x}{h(x)} \right\}, \tag{6.19}$$

*with*

$$h(x) = \exp\left\{ \frac{1}{D} \int (f*\bar{\rho})(x)\,\mathrm{d}x \right\}. \tag{6.20}$$

*Proof.* ( $\Longleftarrow$ )The spatio-temporal dynamics of $\rho^*$ (see (6.17)) obeys to the equation

$$\rho^*_t(x,t) = 2q(x,t) - \left[\rho^L(x,t)u(x,t)\right]_x - \left[\rho^*(x,t)(f*\rho)(x,t)\right]_x + D\rho^*_{xx}(x,t). \tag{6.21}$$

We recall that, $\rho^L$ and $\rho^F$ can be recovered from $\rho$, $\rho^*$ and $\eta^F$ by the change of variables

$$\rho^L(x,t) = \frac{1}{2}\left[\rho(x,t) + \rho^*(x,t) - \eta^F(x,t)\right], \tag{6.22a}$$

$$\rho^F(x,t) = \frac{1}{2}\left[\rho(x,t) - \rho^*(x,t) - \eta^F(x,t)\right]. \tag{6.22b}$$

Substituting (6.16) into (6.21), and being aware of the change of variables (6.22), yields

$$\rho^*_t(x,t) = -a\,\rho^*(x,t) + b\,\rho(x,t) - b\,\eta^F(x,t), \tag{6.23}$$

where

$$a := K_{FL} + K_{LF}, \tag{6.24a}$$

$$b := K_{FL} - K_{LF}. \tag{6.24b}$$

Knowing that, under the control action discussed in Theorem 6.1, $\bar{\rho}$ is a steady-state solution for (6.2), we look for steady-state solutions of (6.23) and (6.1c). We start by considering (6.1c) fixing $\eta^F_t = 0$, $\eta^F(x,t) = \bar{\eta}^F(x)$, and $\rho(x,t) = \bar{\rho}(x)$, yielding to

$$D\bar{\eta}^F_{xx}(x) - \left[\bar{\eta}^F(x)(f * \bar{\rho})(x)\right]_x = 0. \tag{6.25}$$

Integrating (6.25) twice in space (see Appendix E.2 for more details) yields

$$\bar{\eta}^F(x) = \frac{\Phi^F}{\int_S h(x)\,\mathrm{d}x} h(x). \tag{6.26}$$

We remark that $\bar{\eta}^F$ is positive, periodic, and summing to $\Phi^F$ by construction (we refer the reader to Appendix E.2 for more details). We can now seek for the steady-state of $\rho^*$ setting $\rho^*_t = 0$, $\rho(x,t) = \bar{\rho}(x)$, $\rho^*(x,t) = \bar{\rho}^*(x)$, $\eta^F(x,t) = \bar{\eta}^F(x)$ in (6.23). This results in

$$\bar{\rho}^*(x) = \frac{b}{a}\left[\bar{\rho}(x) - \bar{\eta}^F(x)\right]. \tag{6.27}$$

Hence, using the change of variables (6.22), at steady-state it results

$$\bar{\rho}^L(x) = \frac{1}{2}\left[\bar{\rho}(x)\left(1 + \frac{b}{a}\right) - \bar{\eta}^F(x)\left(1 + \frac{b}{a}\right)\right], \tag{6.28a}$$

$$\bar{\rho}^F(x) = \frac{1}{2}\left[\bar{\rho}(x)\left(1 - \frac{b}{a}\right) - \bar{\eta}^F(x)\left(1 - \frac{b}{a}\right)\right]. \tag{6.28b}$$

Being $|b/a| < 1$ by construction, $\bar{\rho}^L$ and $\bar{\rho}^F$ are strictly positive if

$$\bar{\rho}(x) > \bar{\eta}^F, \ \forall x \in \mathcal{S}, \tag{6.29}$$

which is satisfied under condition (6.19) (substituting (6.26) into (6.29)).

( $\Longrightarrow$ ) The existence of a steady-state solution for (6.1) with $\rho^L, \rho^F > 0$ and $\bar{\eta}^F$ implies that

$$\bar{\rho}^L(x) + \bar{\rho}^F(x) > 0, \ \forall x \in \mathcal{S}. \tag{6.30}$$

By adding and subtracting $\bar{\eta}^F$, we obtain

$$\bar{\rho}^L(x) + \bar{\rho}^F(x) + \bar{\eta}^F(x) > \bar{\eta}^F(x), \ \forall x \in \mathcal{S}, \tag{6.31}$$

which is equivalent to

$$\bar{\rho}(x) > \bar{\eta}^F(x), \ \forall x \in \mathcal{S} \tag{6.32}$$

Substituting (6.26) into (6.32) makes the claim proved. ■

**Remark 6.4.** *The result of Theorem 6.2 regards feasibility, as it proves, under which conditions, there exist a meaningful steady-state solution for (6.1) satisfying the problem statement described in Section 6.2.2. Nothing about the stability of this steady-state solution has been said so far.*

**Remark 6.5.** *The condition in Theorem 6.2, can be equivalently given in terms of plasticity (see (6.6)). This result in the condition*

$$p > 1 - \min_x \left\{ \bar{\rho}(x) \frac{\int_{\mathcal{S}} h(x)\,\mathrm{d}x}{h(x)} \right\}, \tag{6.33}$$

*telling the minimum degree of plasticity that is needed to solve the density control problem.*

### *Stability analysis*

In this section, we assess the stability properties of the control solution given by the control velocity field $u$ and the reactive term $q$ as discussed in Theorem 6.1 and 6.2, respectively. From the theorems, we know that, ($i$) under the effect of $u$, $\rho$ approaches $\bar{\rho}$ asymptotically, if $\rho^L$ remains strictly positive, and ($ii$) under the effect of $q$, and if condition (6.19) is fulfilled, there exists a steady-state solution making the problem statement in Section 6.2.2 fulfilled, with $\bar{\rho}^L > 0$.

Next, we prove local stability of the solution whose existence is proved in Theorem 6.2. Let us recall the function $e = \bar{\rho} - \rho$, and let us define the error functions

$$e^*(x,t) = \bar{\rho}^*(x) - \rho^*(x,t), \tag{6.34a}$$

$$e^\eta(x,t) = \bar{\eta}^F(x) - \eta^F(x,t), \tag{6.34b}$$

with $\bar{\rho}^*$ coming from (6.27), and $\bar{\eta}^F(x)$ coming from (6.26).

**Theorem 6.3** (Local stability)**.** *Assuming Theorem 6.2 is fulfilled, the error functions* (6.9)*,* (6.34a) *and* (6.34b) *locally converge to 0 almost everywhere if*

$$\|\bar{\rho}_x(\cdot)\|_2 < \frac{2D}{\|f(\cdot)\|_2} \tag{6.35}$$

*Proof.* The error dynamics under the effect of $u$ and $q$ is given by

$$e_t(x,t) = -K\,e(x,t), \tag{6.36a}$$

$$e^*_t(x,t) = -a\,e^*(x,t) + b\,e(x,t) - b\,e^\eta(x,t), \tag{6.36b}$$

$$\begin{aligned} e^\eta_t(x,t) + [e^\eta(x,t)(f*\bar{\rho})(x)]_x - [e^\eta(x,t)(f*e)(x,t)]_x = \\ = De^\eta_{xx}(x,t) - \left[\bar{\eta}^F(x)(f*e)(x,t)\right]_x. \end{aligned} \tag{6.36c}$$

The first two equations of the error system are linear and not involving spatial derivatives. The third equation, instead is nonlinear and involving spatial derivatives.

By linearizing the last equation, we can rephrase the error system as

$$e_t(x,t) = -K\,e(x,t), \tag{6.37a}$$

$$e^*_t(x,t) = -a\,e^*(x,t) + b\,e(x,t) - b\,e^\eta(x,t), \tag{6.37b}$$

$$e^\eta_t(x,t) + [e^\eta(x,t)(f*\bar{\rho})(x)]_x = De^\eta_{xx}(x,t) - \left[\bar{\eta}^F(x)(f*e)(x,t)\right]_x. \tag{6.37c}$$

Being (6.37a) independent from the other equations and point-wisely convergent to 0, we study the system fixing $e = 0$. In particular, the linearized dynamics of $e^\eta$ becomes

$$e^\eta_t(x,t) + [e^\eta(x,t)(f * \bar{\rho})(x)]_x = De^\eta_{xx}(x,t). \tag{6.38}$$

Let us introduce the Lyapunov functional

$$V(t) = \|e^\eta(\cdot,t)\|_2^2. \tag{6.39}$$

The time derivative of $V$ can be expressed as

$$V_t(t) = 2\int_{\mathcal{S}} e^\eta(x,t)e^\eta_t(x,t)\,\mathrm{d}x, \tag{6.40}$$

and by substituting (6.38), we get

$$V_t(t) = 2D\int_{\mathcal{S}} e^\eta(x,t)e^\eta_{xx}(x,t)\,\mathrm{d}x - 2\int_{\mathcal{S}} e^\eta(x,t)\,[e^\eta(x,t)(f * \bar{\rho})(x)]_x\,\mathrm{d}x. \tag{6.41}$$

We can expand the fist term at second member of (6.41) as

$$2D\int_{\mathcal{S}} e^\eta(x,t)e^\eta_{xx}(x,t)\,\mathrm{d}x = -2D\int_{\mathcal{S}} \left(e^\eta_x(x,t)\right)^2\,\mathrm{d}x = -2D\|e^\eta_x(\cdot,t)\|_2^2, \tag{6.42}$$

where we applied integration by parts (recalling the periodicity of the functions) and the definition of $\mathcal{L}^2$-norm. We can similarly expand the second term at second member of (6.41) as

$$\begin{aligned} -2\int_{\mathcal{S}} e^\eta(x,t)\,[e^\eta(x,t)(f * \bar{\rho})(x)]_x\,\mathrm{d}x &= 2\int_{\mathcal{S}} e^\eta_x(x,t)e^\eta(x,t)(f * \bar{\rho})(x)\,\mathrm{d}x = \\ = \int_{\mathcal{S}} \left[(e^\eta(x,t))^2\right]_x (f * \bar{\rho})(x)\,\mathrm{d}x &= -\int_{\mathcal{S}} (e^\eta(x,t))^2\,(f * \bar{\rho})_x(x)\,\mathrm{d}x, \end{aligned} \tag{6.43}$$

where we used integration by parts (twice), and exploited the identity $\left[(e^\eta)^2\right]_x = 2e^\eta e^\eta_x$. Substituting (6.42) and (6.43) into (6.41), we obtain

$$V_t(t) = -2D\|e^\eta_x(\cdot,t)\|_2^2 - \int_{\mathcal{S}} (e^\eta(x,t))^2\,(f * \bar{\rho})_x(x)\,\mathrm{d}x. \tag{6.44}$$

By using the Poincaré-Wirtinger inequality (see Lemma 1.4 in Chapter 1) we can perform the bound

$$V_t(t) \leq -2D\|e^\eta(\cdot,t)\|_2^2 - \int_{\mathcal{S}} (e^\eta(x,t))^2\,(f * \bar{\rho})_x(x)\,\mathrm{d}x. \tag{6.45}$$

Regarding the second term at the right-hand side of (6.45), we can say

$$\left|\int_{\mathcal{S}} (e^{\eta}(x,t))^2 \, (f * \bar{\rho})_x(x) \, \mathrm{d}x\right| \leq \int_{\mathcal{S}} \left|(e^{\eta}(x,t))^2 \, (f * \bar{\rho})_x(x)\right| \, \mathrm{d}x =$$
$$= \|e^{\eta}(\cdot,t)e^{\eta}(\cdot,t)(f * \bar{\rho})_x(\cdot)\|_1 \leq \|e^{\eta}(\cdot,t)\|_2\|e^{\eta}(\cdot,t)\|_2\|(f * \bar{\rho})_x(\cdot)\|_\infty \leq$$
$$\leq \|e^{\eta}(\cdot,t)\|_2^2\|f(\cdot)\|_2\|\bar{\rho}_x(\cdot)\|_2, \quad (6.46)$$

where we combined the Hölders' inequality (see Lemma 1.1), the definition of derivative of a convolution, and the Young's inequality (see Lemma 1.3). By using the bound (6.46) into (6.45), we finally get

$$V_t(t) \leq (-2D + \|f(\cdot)\|_2\|\bar{\rho}_x(\cdot)\|_2) \, V(t). \quad (6.47)$$

Assuming $\|\bar{\rho}\|_2 < 2D/\|f\|_2$, by comparison (see Lemma 1.5), we know $\|e^{\eta}\|_2^2$ (locally) converges to 0.

Hence, being (6.36a) point-wisely convergent, and (6.36c) locally convergent in $\mathcal{L}^2(\mathcal{S})$, we can study (6.36b) assuming (6.36a) and (6.36c) already converged to 0. This let us conclude about the local stability of (6.36c) almost everywhere ($\mathcal{L}^2$ convergence implies point-wise convergence almost everywhere), making the theorem proved. ∎

**Remark 6.6.** *The error e, whose dynamics is in (6.36a), monotonically goes to 0 as it is linear and stable (recalling $K > 0$). In Theorem 6.3, we prove $e^{\eta}$ locally converges to 0 almost everywhere, as we know it goes to 0 in $\mathcal{L}^2(\mathcal{S})$. Hence, when $e^{\eta}$ converged to 0, the dynamics of $e^*$ is governed by a linear (spatially distributed) and stable ODE almost everywhere. This suggests that e and $e^*$ monotonically decrease to 0 (point-wisely, and almost everywhere), and hence, it is ensured that, starting from a positive leaders' density, $\rho_0^L > 0$, the system locally converge to the desired solution preserving the strict positivity of $\rho^L$.*

**Remark 6.7.** *When $p = 1$ (full plasticity), or, equivalently $\Phi^F = 0$, the problem simplifies, and we can find parameters' regions for which global stability of the solution can be ensured. We refer the reader to Appendix E.1.*

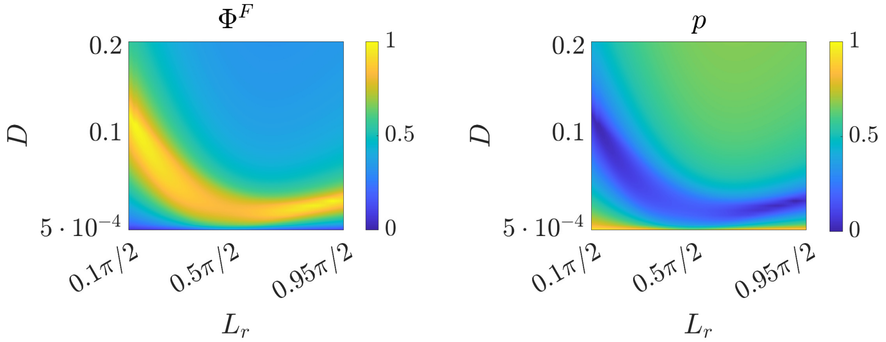

(a) (b)

Figure 6.1: Feasibility plots for a von Mises desired density ($\mu = 0$, $k = 1$), Morse interaction kernel (fixed $L_a$, varying $L_r$), and varying diffusion coefficient $D$: (a) maximum admissible $\Phi^F$, and (b) minimum possible $p$, making the problem feasible (existence of the desired steady-state solution). Parameters: $L_a = \pi$, $\alpha = 2$, $K_{FL} = 1$, $K_{LF} = 2$.

### 6.2.4 Numerical validation

#### *Feasibility plots*

We considered a population of agents interacting through a Morse interaction kernel (long-range attraction, short-range repulsion, see (A.7)) with $L_a = \pi$, $\alpha = 2$, and we considered $L^r \in [0.1\pi/2, 0.95\pi/2]$. We also varied the diffusion coefficient $D \in [5 \cdot 10^{-4}, 0.2]$. We fixed the desired density for the group to be a von Mises distribution with zero mean and $k = 1$ (see (3.25)).

In this set-up, we graphically represented the maximum admissible $\Phi^F$, and, equivalently, the minimum plasticity to ensure feasibility (i.e., Theorem 6.2 holds). Results are given in Fig. 6.1a and 6.1b, respectively. The regions where the larger $\Phi^F$ (minimum $p$) can be considered are the ones in yellow (blue). It is interesting to notice that, as the diffusion coefficient tend to 0, feasibility is more difficult to be granted (it is associated to large plasticity values). This can be explained analysing the problem for $D = 0$ (see App. E.3)

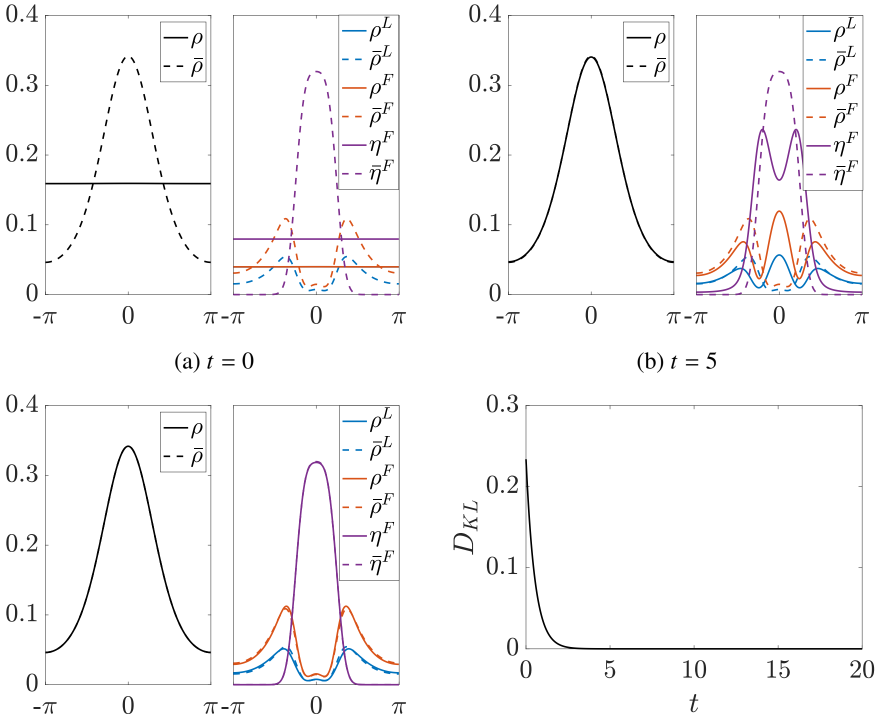

(a) $t = 0$

(b) $t = 5$

(c) $t = 20$

(d)

Figure 6.2: Mono-modal regulation: (a), (b), (c) three snapshot of the simulation trial (respectively, $t = 0$, $t = 5$, $t = 20$), in solid lines the current density, in dashed lines the steady-state prediction we derived; (d) time evolution of the KL divergence between $\rho$ and $\bar{\rho}$.

### *Monomodal regulation*

Here, we consider a monomodal regulation trial. Specifically, we consider the desired density to be a von Mises distribution with $\mu = 0$ and $k = 1$. We assume agents to interact through a periodic Morse interaction kernel with $L_a = \pi$, $L_r = \pi/4$ and $\alpha = 2$, and $D = 0.05$. We fix $\Phi^F = 0.5$ ($p = 0.5$), and $M_0^L = M_0^F = 0.25$, and we assume initial densities to be constant. As control parameters, we choose $K = 1$, $K_{FL} = 1$, and $K_{LF} = 2$.

Results of the simulation trial are reported in Fig. 6.2. Specifically, three snapshot of the simulation are presented, together with the time evolution of the KL divergence between $\rho$ and $\bar{\rho}$ (see (3.23)). Steady-state results are in good accordance with our prediction (represented in dashed lines). Moreover, convergence of $\rho$ to $\bar{\rho}$ is achieved in about 5 time units in accordance with the result of Theorem 6.1 – see (6.12) (we recall that for this specific trial $K = 1$). We remark that the steady-state value of the leaders' and followers' mass are $M^L \approx 0.16$ and $M^F \approx 0.33$, meaning that for each leader there are two followers; this was predictable, as, at steady-state, the mass ratio of two species competing in a mass action law is regulated by the ration of the reaction rates $K_{FL}/K_{LF}$, which, in this trial, was $1/2$.

## 6.3 Higher-dimensional extension

In this Section, we extend the theoretical framework to periodic domains in higher-dimensions, $\Omega = [-\pi, \pi]^d$ ($d = 2, 3$).

The model in (6.1) becomes

$$\rho_t^L(\mathbf{x},t) + \nabla \cdot \left[\rho^L(\mathbf{x},t)\mathbf{u}(\mathbf{x},t) + \rho^L(\mathbf{x},t)(\mathbf{f} * \rho)(\mathbf{x},t)\right] = D\nabla^2\rho^L(\mathbf{x},t) + q(\mathbf{x},t), \tag{6.48a}$$

$$\rho_t^F(\mathbf{x},t) + \nabla \cdot \left[\rho^F(\mathbf{x},t)(\mathbf{f} * \rho)(\mathbf{x},t)\right] = D\nabla^2\rho^F(\mathbf{x},t) - q(\mathbf{x},t), \tag{6.48b}$$

$$\eta_t^F(\mathbf{x},t) + \nabla \cdot \left[\eta^F(\mathbf{x},t)(\mathbf{f} * \rho)(\mathbf{x},t)\right] = D\nabla^2\eta^F(\mathbf{x},t), \tag{6.48c}$$

where $\mathbf{f}$ is a $d$-dimensional periodic kernel, and $\rho = \rho^L + \rho^F + \eta^F$. The system is complemented with periodic boundary conditions and initial conditions similar to those of (6.1).

Theorem 6.1 holds analogously, fixing

$$\nabla \cdot \left[\rho^L(\mathbf{x},t)\mathbf{u}(\mathbf{x},t)\right] = -Ke(\mathbf{x},t) - \nabla \cdot [\rho(\mathbf{x},t)(\mathbf{f} * \rho)(\mathbf{x},t)] - D\nabla^2\rho(\mathbf{x},t), \tag{6.49}$$

as this choice ensure the error system takes the form

$$e_t(\mathbf{x},t) = -K\, e(\mathbf{x},t). \tag{6.50}$$

To uniquely recover $\mathbf{u}$, a vector field, from the scalar relation (6.49), some extra constraints needs to be fixed as also done in Chapter 3. Specifically, following the steps given in Section 3.4.3, we fix $\mathbf{w} := \rho^L\mathbf{U}$, and

$$Y(\mathbf{x},t) = -Ke(\mathbf{x},t) - \nabla \cdot [\rho(\mathbf{x},t)(\mathbf{f} * \rho)(\mathbf{x},t)] - D\nabla^2\rho(\mathbf{x},t), \tag{6.51}$$

so that we can pose the problem

$$\begin{cases} \nabla \cdot \mathbf{w}(\mathbf{x},t) = Y(\mathbf{x},t), \\ \nabla \times \mathbf{w}(\mathbf{x},t) = 0, \end{cases} \tag{6.52}$$

where we added a zero-curl condition to (6.49). Such a problem is analogous to the Poisson equation $\nabla^2\varphi = -Y$, where we assume $\mathbf{w} = -\nabla\varphi$. The Poisson problem can be solved using the Fourier series expansion (see from (3.16) to (3.19) in Chapter 3) so that $\varphi$, and consequently $\mathbf{w}$ are recovered. Finally $\mathbf{U} = \mathbf{w}/\rho^L$. Analogously to the one-dimensional case, the resulting controlled velocity field $\mathbf{u}$ is well defined only if $\rho^L$ is strictly positive.

Such a constraint can be ensured by appropriately choosing the reacting function $q$. In particular, extending (6.16) to higher dimensions, we get

$$q(\mathbf{x},t) = \frac{1}{2}\nabla \cdot \left[\rho^L(\mathbf{x},t)(\mathbf{x},t)\right] + \frac{1}{2}\nabla \cdot \left[\rho^*(\mathbf{x},t)(\mathbf{f} * \rho)(\mathbf{x},t)\right] - \frac{D}{2}\nabla^2\rho^*(\mathbf{x},t) + g(\mathbf{x},t), \tag{6.53}$$

where $\rho^* = \rho^L - \rho^F$ and $g$ is the mass action law

$$g(\mathbf{x},t) = K_{FL}\rho^F(\mathbf{x},t) - K_{LF}\rho^L(\mathbf{x},t). \tag{6.54}$$

When extending Theorem 6.2 to higher dimensions, no modifications are needed until we need to compute the steady-state of $\eta^F$ (see (6.26)). Specifically, fixing $\eta^F_t = 0$ and $\rho = \bar{\rho}$ in (6.48c), we get

$$\nabla \cdot \left[\bar{\eta}^F(\mathbf{x})(\mathbf{f} * \bar{\rho})(\mathbf{x})\right] = D\nabla^2\bar{\eta}^F(\mathbf{x}), \tag{6.55}$$

which can be rewritten as

$$\nabla \cdot \left[\bar{\eta}^F(\mathbf{x})(\mathbf{f} * \bar{\rho})(\mathbf{x})\right] = D\nabla \cdot \left[\nabla\bar{\eta}^F(\mathbf{x})\right]. \tag{6.56}$$

Equation (6.56) is fulfilled if[1]

$$\nabla\bar{\eta}^F(\mathbf{x}) = \frac{1}{D}\bar{\eta}^F(\mathbf{x})(\mathbf{f} * \bar{\rho})(\mathbf{x}). \tag{6.57}$$

---

[1] This passage becomes a necessary and sufficient condition if we assume to look for solutions such that $\nabla \times \left[\eta^F(\mathbf{f} * \bar{\rho})\right] = 0$, and $\nabla(\phi - \psi) = 0$, where $\phi = \nabla\left[\bar{\eta}^F(\mathbf{f}\bar{\rho})\right]$, and $\psi = \nabla\left[\nabla\bar{\eta}^F\right]$.

Equation (6.57) is a vectorial differential relation involving the partial derivatives of the scalar unknown $\bar{\eta}^F$, thus resulting in an ill-posed problem, which can be expanded as

$$\begin{cases} \bar{\eta}^F_{x_1}(x_1,x_2) = \frac{1}{D}\bar{\eta}^F(x_1,x_2)(f_1 * \bar{\rho})(x_1,x_2), \\ \bar{\eta}^F_{x_2}(x_1,x_2) = \frac{1}{D}\bar{\eta}^F(x_1,x_2)(f_2 * \bar{\rho})(x_1,x_2). \end{cases} \tag{6.58}$$

where, without any loss of generality, we fixed $d = 2$, $\mathbf{f} = [f_1, f_2]$, $\mathbf{x} = [x_1, x_2]$[2]. By solving the first component of (6.58), we get

$$\bar{\eta}^F(x_1,x_2) = C(x_2)h(x_1,x_2), \tag{6.59}$$

where $C$ is a function of $x_2$ coming from the spatial integration with respect to $x_1$, and

$$h(x_1,x_2) = \exp\left\{\frac{1}{D}\int (f_1 * \bar{\rho})(x_1,x_2)\,\mathrm{d}x_1\right\}. \tag{6.60}$$

We can now check under which conditions the second component of (6.58) is fulfilled under the choice of $\bar{\eta}^F$ in (6.59). In so doing, we impose the partial derivative of (6.59) with respect to $x_2$ to fulfill the second component of (6.58), that is

$$C_{x_2}(x_2)h(x_1,x_2) + C(x_2)h_{x_2}(x_1,x_2) = C(x_2)h(x_1,x_2)\frac{(f_2 * \bar{\rho})(x_1,x_2)}{D}, \tag{6.61}$$

which represents a linear ODE for $C$. If we fix

$$C(x_2) = C = \text{const.}, \tag{6.62}$$

and we further assume to have an isotropic interaction kernel, that is

$$\int (f_1 * \psi)(x_1,x_2)\,\mathrm{d}x_1 = \int (f_2 * \psi)(x_1,x_2)\,\mathrm{d}x_2, \tag{6.63}$$

for any periodic $\psi$, equation (6.61) remains satisfied[3]. The value of $C$ can be finally

---

[2] The case $d = 3$ is a trivial extension.

[3] By fixing $C$ to be constant in (6.61) and computing $h_{x_2}$

$$\frac{h(x_1,x_2)}{D}\left[\int (f_1 * \bar{\rho})(x_1,x_2)\,\mathrm{d}x_1\right]_{x_2} = \frac{h(x_1,x_2)}{D}(f_2 * \bar{\rho})(x_1,x_2),$$

$$\left[\int (f_1 * \bar{\rho})(x_1,x_2)\,\mathrm{d}x_1\right]_{x_2} = (f_2 * \bar{\rho})(x_1,x_2),$$

that is fulfilled under the isotropic assumption for the kernel (6.63).

chosen to let $\bar{\eta}^F$ sums to $\Phi^F$.

The local stability analysis carried out in Theorem 6.3 can be straightforwardly extended to higher dimensions[4]. The Theorem condition in higher dimensions takes the form

$$\sum_{i=1}^{d} \|\bar{\rho}_{x_i}(\cdot)\|_2 \|f_i(\cdot)\|_2 < 2D, \tag{6.64}$$

linking the interaction kernel, the diffusivity and the desired density to achieve.

**Remark 6.8.** *Our framework smoothly scales to higher-dimensional domains under the hypothesis of isotropic interaction kernel, which for* $d = 3$ *reads*

$$\int (f_1 * \psi)(x_1, x_2, x_3)\,\mathrm{d}x_1 = \int (f_2 * \psi)(x_1, x_2 x_3)\,\mathrm{d}x_2 = \int (f_3 * \psi)(x_1, x_2, x_3)\,\mathrm{d}x_3, \tag{6.65}$$

*for any periodic* $\psi$*. We remark that, all the interaction kernels that have been used throughout this theses satisfy condition* (6.63)*. Also, the steady-state solution for* $\eta^F$ *is not uniquely defined in higher dimensions. To ensure its uniqueness, we need to add extra conditions, that are*

$$\nabla \times \left[\bar{\eta}^F(\mathbf{x})(\mathbf{f} * \rho)(\mathbf{x})\right] = 0, \tag{6.66a}$$

$$\nabla\left[\phi(\mathbf{x}) - \psi(\mathbf{x})\right] = 0, \tag{6.66b}$$

---

[4] The whole theorem follows the same structure of its one-dimensional counterpart. The time derivative of the Lyapunov functional in (6.41) can be rewritten as (dropping dependencies for simplicity)

$$V_t = -2D\|\nabla e^{\eta}\|_2^2 - \int_{\Omega} (e^{\eta})^2\, \nabla \cdot (f * \bar{\rho})\,\mathrm{d}\mathbf{x},$$

using the divergence theorem and vectorial identities. The first term at second member can be bounded using the Poincaré-Wirtinger inequality (see Remark 1.2), while, for the second one the following bound holds

$$\left|\int_{\Omega} (e^{\eta})^2\, \nabla \cdot (f * \bar{\rho})\,\mathrm{d}\mathbf{x}\right| \leq \int_{\Omega} \left|(e^{\eta})^2\, \nabla \cdot (f * \bar{\rho})\right| \mathrm{d}\mathbf{x} = \|e^{\eta} e^{\eta} \nabla \cdot (f * \bar{\rho})\|_1 \leq$$
$$\leq \|e^{\eta}\|_2^2 \|\nabla \cdot (f * \bar{\rho})\|_{\infty} \leq \|e^{\eta}\|_2^2 \sum_{i=1}^{d} \|(f_i * \bar{\rho}_{x_i})\|_{\infty} \leq \|e^{\eta}\|_2^2 \sum_{i=1}^{d} \|f_i\|_2 \|\bar{\rho}_{x_i}\|_2,$$

where we used the Hölder's, Minkowsky's and Young's inequality. This lead us to the following bound on the time derivative of the Lyapunov functional

$$V_t \leq \left(-2D + \sum_{i=1}^{d} \|f_i\|_2 \|\bar{\rho}_{x_i}\|_2\right) V.$$

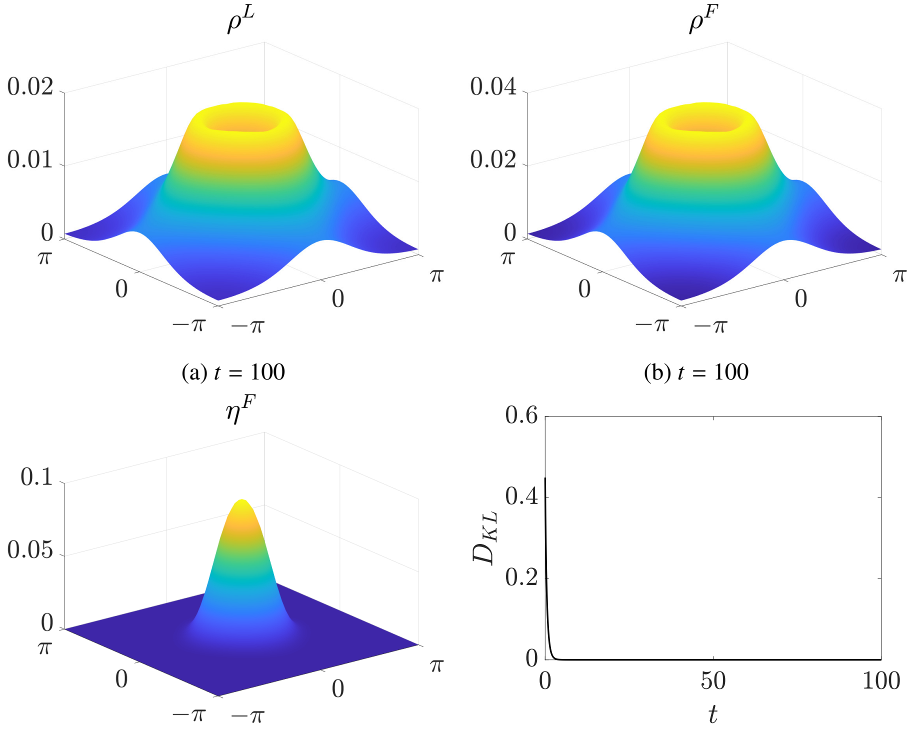

(a) $t = 100$ (b) $t = 100$

(c) $t = 100$ (d)

Figure 6.3: 2D Mono-modal regulation: (a) leaders', (b) reactive followers', (c) non-reactive followers' density at $t = 100$; (d) time evolution of the KL divergence between $\rho$ and $\bar{\rho}$.

*where* $\phi = \nabla\left[\bar{\eta}^F(\mathbf{f}\bar{\rho})\right]$, *and* $\psi = \nabla\left[\nabla\bar{\eta}^F\right]$.

### 6.3.1 Numerical validation

Here we consider a mono-modal regulation scenario similar to the one we consider for the one-dimensional numerical validation. Specifically, we considered as desired density a bivariate von Mises distribution with 0 means and unit concentration coefficients – see (3.26). We assume agents to be characterized by the diffusion coefficient $D = 0.05$, and to interact through a 2D periodic Morse kernel with parameters $L_a = \pi$, $L_r = \pi/4$, $\alpha = 3.2$ (no closed form for such a kernel was found – we refer the reader to Appendix A for more details about its approximation). We fixed $\Phi^F = 0.2$ ($p = 0.8$), $M_0^L = M_0^F = 0.4$, and, initial densities to be constant. As control parameters, we choose $K = 1$, $K_{FL} = 1$, and $K_{LF} = 2$.

Results of the simulation trial are reported in Fig. 6.3. In particular, we show the density profiles of all the populations at the end of the trial, that is $t = 100$, and the time evolution of the KL divergence. We observe good qualitative accordance between the one- and two-dimensional trials, both in terms of agents displacement and approach of $\rho$ with respect to $\bar{\rho}$. As for the one-dimensional trial, we remark that convergence of $\rho$ to $\bar{\rho}$ is achieved in almost 5 time units, being $K = 1$ and because of (6.12) – see Fig. 6.3d. Note that convergence of $\rho^L$, $\rho^F$ and $\eta^F$ to their steady-states profiles is instead slower. We point out that, at the end of the trial, it results $M^L \approx 0.26$, and $M^F \approx 0.53$. This is in accordance with the choice of the reaction rates, which predicts the leaders and followers' mass to be in a $1/2$ ratio.

## 6.4 Preliminary results about robustness

In this section, we give some preliminary numerical results about how robustness varies with different levels of plasticity. Our aim is to show that, in accordance with biological systems, larger levels of plasticity are associated with increased robustness properties.

We considered a one-dimensional set-up similar to that discussed in Section 6.2.4. In particular, we fixed the desired population density to be the normal von Mises distribution ((3.25), with $\kappa = 1$ and $\mu = 0$, normalized to 1); interactions among the agents are set via a periodic Morse interaction with $L_a = \pi$, $L_r = \pi/4$ and $\alpha = 2$; furthermore, we set $K = 10$. In such a set-up we introduce a perturbation on the followers behavior, both for reactive and non-reactive ones. In particular, we assumed a nominal diffusion coefficient $D = 0.02$, while the dynamics of followers has been perturbed using the diffusion $\widehat{D} = 2D$ – see (6.1). In this framework, we considered the initial populations' densities to be the equilibrium configurations computed in Section 6.2.3, and, starting from that condition, we assessed how different choices for the degree of plasticity $p$ influence the degradation of the performance[5]. Notice that, we fixed the reacting rates $K_{LF}$ and $K_{FL}$ so that the steady-state mass of leaders is constant (and equal to 0.2) for different values of $p$. In such a way, the amplitude of the perturbation that we introduce is constant for each $p$.

---

[5] For values of $p$ that are below the minimum plasticity threshold prescribed by Theorem 6.2 – see remark 6.5 – the steady-state configurations $\bar{\rho}^L$ and $\bar{\rho}^F$ are not feasible (that is, they are negative in some regions of the domain). For these cases, we considered as initial configuration of the robustness analysis trial a modification of those unfeasible densities. Specifically, we translate them upwards until they are non-negative, and we re-normalize them to a predefined mass.

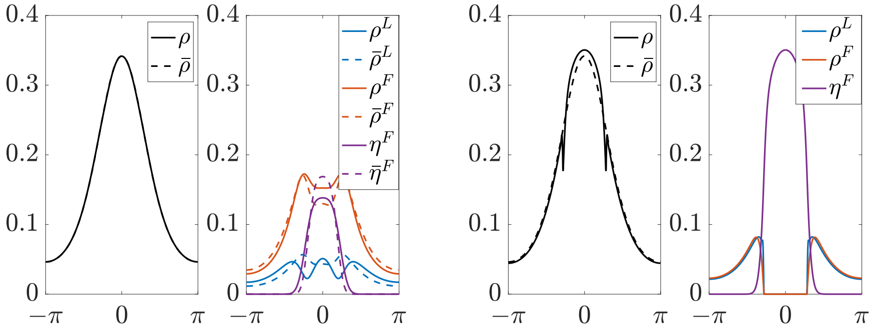

(a) $p = 0.8$

(b) $p = 0.4$

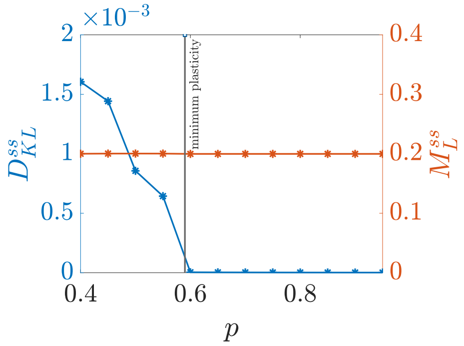

(c)

Figure 6.4: Robustness to parametric uncertainty with different degree of plasticity. (a) Final configuration of the swarm with $p = 0.8$; (b) Final configuration of the swarm with $p = 0.4$; (c) KL divergence (blue) and leaders' mass (orange) at steady-state (in solid gray the predicted minimum plasticity ensuring feasibility).

Results of such a robustness analysis are reported in Fig. 6.4 (assuming the steady-state leaders' mass is 0.2). In particular, in Fig. 6.4b and 6.4a we show the populations' densities after 10 time units from the beginning of the numerical trial for the case $p = 0.8$ and $p = 0.4$, respectively. For the case $p = 0.8$, agents are able to find a configuration in which the control goal remains satisfied, that is $\rho = \rho^{\mathrm{d}}$. Such a tendency is consistent with values of the degree of plasticity such that $p \geq 0.6$, as it can be noticed from the aggregated results in Fig. 6.4c. Notice that, for the specific scenario we are considering the minimum plasticity ensuring feasibility is slightly below 0.6 (solid gray vertical line in Fig. 6.4c). When $p$ goes below the minimum plasticity threshold, we observe a degradation of the steady-state performance, that decreases as $p$ decreases. Note that, when below the minimum plasticity threshold, as per Theorem 6.2 we are not able to recover positive steady-state densities for leaders and followers (resulting in the absence of dashed lines in the right panel of Fig. 6.4a).

The aggregated results in Fig. 6.4c show that when above the minimum plasticity threshold prescribed by Theorem 6.2, performance are independent from the specific degree of plasticity, as the control goal remains always satisfied. Conversely, performance start degrading when below the minimum plasticity threshold, proportionally with the degree of plasticity (the lower, the worse performance become).

## 6.5 Discussion

We developed a mathematical framework for modeling and understanding behavioral plasticity. This set-up consists of three PDEs, each one describing the density dynamics of the different agents' species we considered, namely, leaders, followers and non-reactive followers. We considered a density control task, a paradigmatic scenario into which many real application falls. For such a problem, we considered $(i)$ leaders can be actively controlled, and, eventually, transformed into followers, $(ii)$ followers can be transformed into leaders, and $(iii)$ non-reactive followers only react to the actions of the other agents.

We phrased the problem at the macroscopic scale, in order to compactly catch large-scale problems avoiding the curse of dimensionality, and to easily derive analytical guarantees regarding the solution. Our first main result regards feasibility: we derived a necessary and sufficient condition for the problem to admits a desirable solution. The existence of such a solution depends on important parameters of the system, such as the desired density, the interaction kernel parameters, the diffusivity of the agents, and the amount of each species in the collective. The second main result consists of a control algorithm for the leaders, and a reactive mechanism between leaders and followers solving the density control problem with analytical guarantees of local convergence. We also remark that our solution lets the designer choose the steady-state leaders-to-followers ratio.

The goal of our work is two-fold. Firstly, it proposes a simple and effective model for behavioral plasticity (in domains of arbitrary dimensions), a biological mechanism underlying many natural phenomena. Then, formulating the problem through the lenses of a (density) control problem, we offer a viable way to drive new solutions for control tasks and swarm robotics applications. In particular, we demonstrated behavioral plasticity is unveiling interesting and useful robustness and flexibility properties. Specifically, we numerically assessed how increased plasticity is associated with increased robustness with respect to parametric uncertainty.

In the next Chapter, we consider the problem of experimentally validating techniques for the control of large-scale multi-agent systems, as, for example the ones that are discussed so far in the Thesis (developed in the limit of infinite number of agents). We remark that these kind of experiments are remarkably critical because of their inherent high resources and time cost. For this reason agile platforms that mitigate this kind of costs are especially needed in this field. We decided to tackle this problem by developing a mixed reality platform, where part of the swarm is implemented as differential drive robots, and the rest is virtualized via software. In such a way, swarms of arbitrary size can be tested in this hybrid experimental platform.

# 7 Mixed Reality Environment for Agile Swarm Robotics Experiments

In this Chapter we cover part of the material documented in [31]. Many new methodologies for the control of large-scale multi-agent systems are based on macroscopic representations of the emerging system dynamics, in the form of continuum approximations of large ensembles. These techniques, that are developed in the limit case of an infinite number of agents, are usually validated only through numerical simulations. In this paper, we introduce a mixed reality set-up for testing swarm robotics techniques, focusing on the macroscopic collective motion of robotic swarms. This hybrid apparatus combines both real differential drive robots and virtual agents to create a heterogeneous swarm of tunable size. We also assess experimentally the validity of the continuification control procedure that is developed in Chapter 3. Our study demonstrates the effectiveness of the platform for conducting large-scale swarm robotics experiments, and it contributes new experimental insights into control algorithms exploiting continuification approaches.

## 7.1 Introduction

Several new techniques for the analysis and control of large-scale multi-agent systems rely on the assumption that the interacting dynamical systems of the ensemble (*agents*) are numerous enough to be described in a continuuum framework[26, 29, 30, 66, 67]. Such an assumption paves the way for recasting many traditional *microscopic* agent-based formulations, based on large sets of ordinary differential equations (ODEs), into smaller sets of partial differential equations (PDEs) for a *macroscopic* representation of their collective behavior. For instance, it can be advantageous to study the spatio-temporal dynamics of a large group of mobile agents in terms of their density, rather than keeping track of the motion of each of the agents [26, 29, 30, 53, 125]. In so doing, one can address the curse of dimensionality of microscopic representations by formulating control algorithms at the scale where the collective behavior emerges [153]. Suitable applications include, but are not limited to, multi-robot systems [125, 126, 172], traffic control [198, 199], cell populations [173], and human networks [10].

Recasting these systems into continuum formulations offers new opportunities in the analysis and design of novel control approaches to tame collective dynamics. A pressing open challenges is to find agile methods to inform and experimentally validate the synthesis of control algorithms developed in a continuum framework. Full-scale experiments about the control of large-scale multi-agent systems have been recently carried out [137, 138, 139, 140]. However, the majority of the existing control solutions have been tested only using computer simulations due to practical limitations. In this paper, we present a novel mixed reality environment where some real mobile robots interact among themselves and with other virtual agents. We bring settings as that in [147] and other recent mixed reality platforms [148, 149], to large-scale scenarios. In so doing, we integrate insights from disability studies [141, 142] and animal behavior research [143, 144, 145, 146] where digital twins of patients or animals are often utilized for testing new strategies in virtual reality settings. Our set-up let the user choose the size of the ensemble to study, avoiding the bottleneck of extreme time cost and resources of experiments of large-scale systems. Moreover, in our setting, the specific model for the virtual agents can be chosen by the designer and is not constrained to a specific commercial robot. The whole apparatus is easy to implement and can be realized, for example, by adapting other existing facilities such as the Robotarium at GeorgiaTech [152]. Relevant previous work in the field of swarm robotics includes the use of augmented reality for providing simple testbed agents, like kilobots, with augmented sensing capabilities [150, 151].

The rest of the Chapter is organized as follows. In Section 7.2, we describe the experimental platform. Specifically, in Section 7.2.1 we focus on the mobile robots we designed, and then, in Section 7.2.2 on the platform itself. In Section 7.3 to demonstrate the use of the platform. We discuss results and conclusions in Section 7.3.2 and 7.5, respectively.

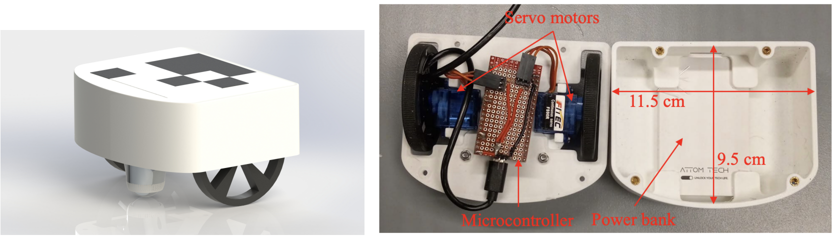

(a) (b)

Figure 7.1: (a) Render of a differential drive robot, and (b) inner view of the robot.

## 7.2 Experimental mixed reality environment

Here, we detail our experimental apparatus for the design of experiments about the coordination of hybrid large swarms of real robots and virtual agents. We first present the mobile robotic agents and their kinematics. Then, we describe the integration of these robots with the virtual agents in the overall mixed reality platform.

### 7.2.1 Differential drive robots

We built four differential drive robots, as the one rendered in Fig. 7.1a. These robots featured a 3D-printed PLA frame (Polylite, Polymaker) printed on a Bambu Lab X1C (CAD model available on `github`). The sizes of the robot are such that it can be schematized as a rectangle 11.5 cm × 9.5 cm. Each robot was equipped with an ESP32 microcontroller, operating two continuous rotation servo motors (FS90R, Feetech) directly connected to 56 mm wheels. Additionally, an omni-directional wheel was attached at the front-bottom of the robot. Power was supplied to each robot through an off-the-shelf power bank (Attom, Ultra Slim 3000mAh). We show the real robot, with sizes and hardware in Fig. 7.1b. In the absence of a load, the motors are able to rotate at approximately 14 rad/s and provide a torque of 1.5 kg·cm. Taking into account the wheel radius, the maximum linear speed that can be achieved by the robot is approximately 0.8 m/s (when both wheels are rotating in the same direction at full speed).

The $i$-th differential drive robots is characterized by the following non-holonomic kinematic behavior:

$$\dot{\mathbf{z}}_i^{\mathrm{R}} = \mathbf{R}(\theta_i)\,\mathbf{u}_i^{\mathrm{R}}, \tag{7.1}$$

for $i = 1, \ldots, 4$. In particular, $\mathbf{z}_i^{\mathrm{R}} = [\mathbf{x}_i^{\mathrm{R}}, \theta_i]^T$ is the state of the $i$-th differential drive

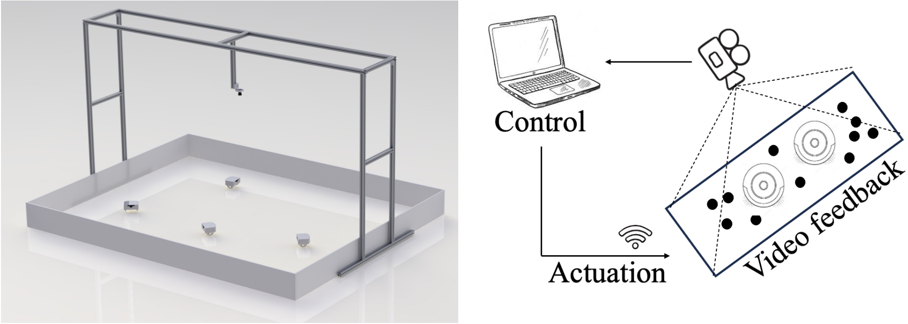

(a) (b)

Figure 7.2: Experimental platform. (a) A render of the real set-up, with 4 robots moving in the arena, and (b) a sketch of the platform, assuming virtual agents to be the black dots and real robots to be concentric circles.

robot, where $\mathbf{x}_i^{\mathrm{R}} = [x_{i,1}^{\mathrm{R}}, x_{i,2}^{\mathrm{R}}]^T$ is its position in a Cartesian coordinate framework and $\theta_i \in [-\pi, \pi]$ its orientation. Moreover,

$$\mathbf{R}(\theta) = \begin{bmatrix} \cos\theta_i & 0 \\ \sin\theta_i & 0 \\ 0 & 1 \end{bmatrix}, \tag{7.2}$$

and $\mathbf{u}_i^R = [V_i, \omega_i]^T$ is the vector of the control variables, with $V_i$ being the instantaneous velocity of the mid-point between the robots' wheels, and with $\omega_i$ being its angular velocity.

### 7.2.2 Mixed reality environment

We built the set-up shown in Fig. 7.2a, comprising a set of differential drive robots moving on the ground and an overhead camera (16MP wide-angle camera – Arducam, placed at 1m height). The camera was placed so that the robots could move in an area of approximately 2 m × 2 m. Aruco markers were attached to the robots, so that they could be easily tracked by the camera and perform their pose estimation. A Python program using OpenCV was developed to estimate the robots' pose in each frame. The video feed, with all the estimated robots' positions, was given to the central station of the platform, a Dell Aurora (13th Gen Intel® i9 13900KF, 64GB of DDR5 RAM NVIDIA® GeForce RTX™ 4090). Such a machine was also provided with the positions (and eventually velocities) of a user-defined number of virtual agents. In principle, one can choose the

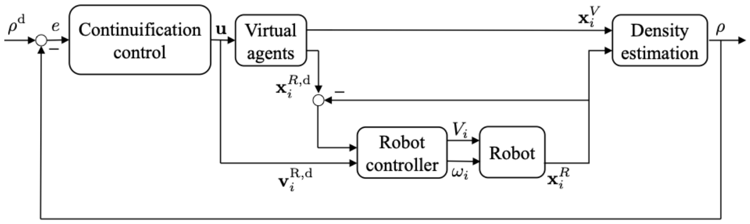

Figure 7.3: Control scheme for robot $i$. By measuring the overall density of the swarm, the continuification control inputs can be used to give the robots a desired position and velocity to track.

specific mathematical model for the virtual agents. Based on the literature about the control of large-scale mobile agents, a reasonable choice is to select their dynamics as that of single or double integrator without any kinematic constraint [53, 166]. Using the available information (robots' positions and virtual agents' positions, at least), the central station was in charge of controlling the hybrid swarm of real and virtual agents, according to some user-definable algorithm. Such a control algorithm should be chosen so that the needed information could be estimated by tracking the real robots with a camera, since robots were not equipped with any specific sensor.

The application of any control strategy consists of (*i*) updating the positions of the virtual agents, based on the specific dynamical model that is assumed for them, and (*ii*) computing the control inputs for the real robots and sending them through a TCP client/server communication protocol on the local Wi-Fi. The idea is sketched in Fig. 7.2b. Since collective motion techniques are typically developed for kinematically unconstrained agents, a low-level trajectory tracking control is needed for the robots. We used the input/output feedback linearization technique that is proposed in [200] (Chapter 11.6).

We remark that the set-up we propose is versatile, as it could account for various constraints that can be chosen by the user, like, for instance, limited sensing and obstacles.

## 7.3 Validation of the continuification control strategy of Chapter 3 via the new experimental platform

Next, we experimentally validate the higher-dimensional continuification control strategy proposed in Section 3.4 to steer the collective behavior of a swarm of robots in the plane.

In so doing, we also demonstrate the use of our experimental platform for evaluating the performance of control algorithms. To this aim, we fix $d = 2$, making $\Omega$ the periodic square. For modeling pairwise interactions between the agents, we choose a periodic soft-core repulsive kernel, based on its non-periodic version

$$\mathbf{f}(\mathbf{x}) = \begin{cases} \frac{\mathbf{x}}{\|\mathbf{x}\|} \mathrm{e}^{-\frac{\|\mathbf{x}\|}{L}} & \text{if } \|\mathbf{x}\| \neq 0 \\ 0 & \text{otherwise.} \end{cases} \tag{7.3}$$

The periodization of the kernel consists in an infinite series extending the non-periodic kernel in every direction. Since no closed form was found, we approximate it by truncating the series (see Appendix A for more details). Moreover, we fix $L = 1$.

In what follows, we always refer to a Cartesian coordinate system, like the one considered for the individual kinematics. For each experimental trial we consider that agents start on a perfect square lattice, meaning that the initial density is constant and, in particular, $\rho(\mathbf{x}, 0) = N/(2\pi)^2$. As for the desired density to achieve, we choose the 2D Von-Mises function in (3.26), which we report here for convenience

$$\rho^{\mathrm{d}}(\mathbf{x}) = Z \exp\{\mathbf{k}^T \, \mathbf{c}_1(\mathbf{x}, \mu, \nu) + c_2(\mathbf{x}, \mu, \mu) \, \mathbf{I}_2 \, c_2^T(\mathbf{x}, \nu, \nu)\}$$

where $\mathbf{k} = [k_1, k_2]^T$ is the vector of the concentration coefficients, $\mu$ and $\nu$ are the means along the two directions, $\mathbf{c_1}(\mathbf{x}, a, b) = [\cos(x_1 - a), \cos(x_2 - b)]$ and $\mathbf{c_2}(\mathbf{x}, a, b) = [\cos(x_1 - a), \sin(x_2 - b)]$ (with $a, b \in \Omega$), where $x_1$ and $x_2$ are the components of $\mathbf{x}$ in the Cartesian coordinate system, and $\mathbf{I}_2$ is the second order identity matrix. $Z$ is a normalization coefficient, to allow $\rho^{\mathrm{d}}$ to sum to the total number of agents $N$. To assess the performance in different scenarios, we also take into account the case where the desired density is multimodal, that is the combination of several densities like (3.26). To address tracking scenarios as well, we study the case where the means, $\mu$ and $\nu$, in (3.26) are time varying. We remark that the scenarios we consider mimic more classical microscopic problems of spatial organization. For instance, density regulation to Gaussian-like profiles can be seen as rendez-vous problems [201], while tracking cases as formation control ones [202].

The overall control scheme for the hybrid swarm is shown in Fig. 7.3. Specifically, while virtual agents' positions can be updated purely using the technique described in Section 3.4, for the differential drive robots, that are kinematically constrained (see Section 7.2.1), such a method needs to be integrated with an ad-hoc controller for tracking problems. As previously mentioned, we used the input/output feedback linearization

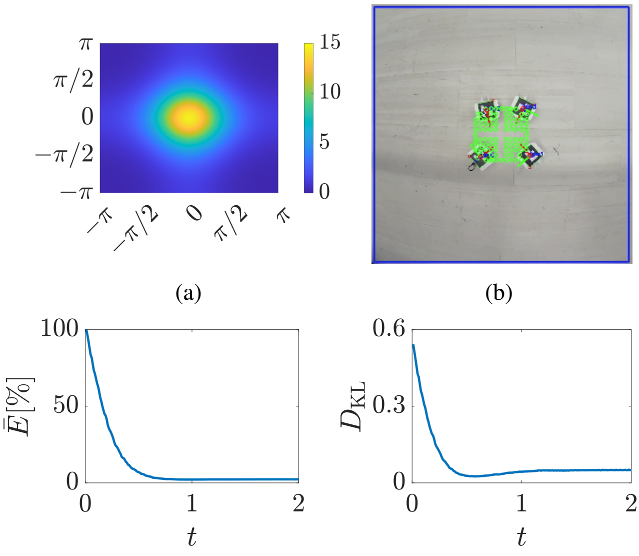

(a) (b)

(c) (d)

Figure 7.4: Monomodal regulation. (a) Desired density, (b) steady-state configuration of the swarm, (c) percentage error in time, (d) KL divergence in time.

technique in [200] (Chapter 11.6). The integration is performed by using the continuification method to compute the desired position and velocity of the robot, that is then tracked with its embedded controller. In the case where only real robots are present, the blocks regarding virtual agents in the scheme in Fig. 7.3 shall be omitted. To adapt the assumption on the periodicity of the domain to the experiments and avoid real robots to try to cross the domain's boundaries, we defined a fictitious periodic extended domain (double sized with respect to the effective arena where robots move). The arena where agents move is the inner part of such an extended domain. To avoid agents going out of the arena (that is the inner part of the domain), the desired density is set as the actual one in the inner part of the domain, and is then extended to be almost zero elsewhere (i.e., in the arena fictitious extension).

We characterize the experiments recording $||e||^2$ in time. Specifically, the performance of each trial is assessed in terms of the percentage error in (3.22) Trials are also characterized using the Kullback-Leibler (KL) divergence (see (3.23)), as often done for density control problems [170].

For each trial, we considered a sample of $N = 100$ agents (96 virtual agents and 4 real robots), and we discretized (3.1) (modeling the motion of the virtual agents and the

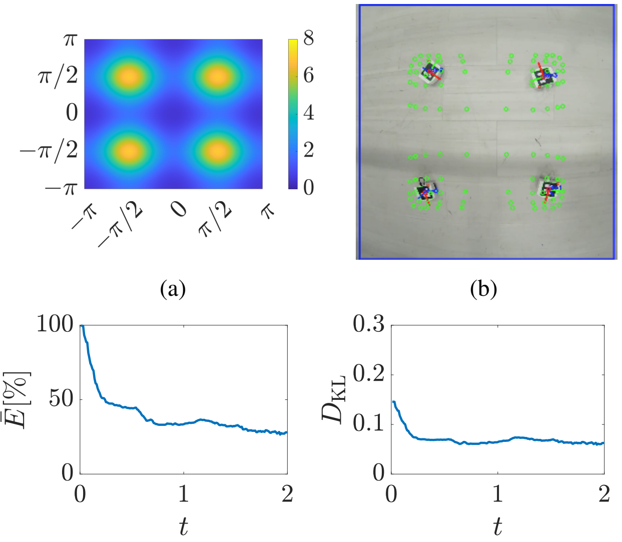

(a) (b)

(c) (d)

Figure 7.5: Multimodal regulation. (a) Desired density, (b) steady-state configuration of the swarm, (c) percentage error in time, (d) KL divergence in time.

desired positions for the robots) using forward Euler with a non-dimensional time step $\Delta t = 0.01$. This corresponds to the camera frame rate of 20 frames per second (FPS) in the experiments, at which the control algorithm is running. Thus, the unit non-dimensional time in any of our graphs corresponds to 5 s. The spatial domain is discretized into a regular mesh of $200 \times 200$ cells. We remark that virtual agents are indeed not constrained to move on such a mesh, and that it is only used for defining functions such as the desired and effective density of the swarm. We also remark that spatial measures are adapted to consider that the region where robots are moving coincides with the definition of $\Omega$.

### 7.3.1 Experimental trials

Here, we detail our experiments, whose videos are available on github.

**Monomodal regulation** We want the hybrid swarm to start from an initial constant density and aggregate towards the von Mises function that is depicted in Fig. 7.4a, which is characterized by $\mu = \nu = 0$, and $\kappa_1 = \kappa_2 = 1.5$ (see (3.26)). Such a desired configuration consists in a clustered formation about the origin of $\Omega$. The final formation that is achieved by the swarm is reported in Fig. 7.4b, while the time evolution of $\bar{E}$ is shown in Fig. 7.4c. We record a steady-state value of $\bar{E}$, that is the residual percentage $\mathcal{L}^2$ error, of approximately 2%. In Fig. 7.4d, we report the time evolution of the KL divergece.

**Multimodal regulation** We consider the swarm to start from an initial constant density and aggregate towards the combination of four von Mises functions as the one in (3.26) (see Fig. 7.5a for a graphical representation). The concentration coefficients of all the modes is set to 2, and the mean values are $\mu_1 = \mu_2 = -\pi/2$, $\mu_3 = \mu_4 = \pi/2$, $\nu_1 = \nu_2 = \pi/2$, and $\nu_3 = \nu_4 = \pi/2$. This desired density consists of four clusters of agents symmetrically displaced around the origin. The final formation is reported in Fig. 7.5b, while the time evolution of $\bar{E}$ is shown in Fig. 7.5c. The final value of $\bar{E}$ is below 30%. In Fig. 7.5d we show the time evolution of the KL divergence.

**Monomodal tracking** Here, we focus on a monomodal tracking scenario, where the desired density is a 2D von Mises function, whose means are time varying, see (3.26). Specifically, we consider $\mu(t)$ and $\nu(t)$ behaving as in Fig. 7.6a, while the concentration coefficients are kept constant and equal to 1. Such a desired density is centered at the origin for $t \leq 1$. Then, it starts moving at constant velocity towards a side of the domain and then on the circle of radius $\pi/2$. We report the results of the trial in Fig. 7.6b, where the evolution of $\bar{E}$ is shown. Specifically, its steady-state value is below 50%. For brevity, we do not report the KL divergence in time, which remains below 0.25.

**Multimodal tracking** Here, we consider a multimodal tracking case, where two von Mises functions with constant concentration coefficients of 2.2 orbitate on the circle of radius $2\pi/3$, after remaining still at two sides of the domain for $t \leq 1$. Specifically, $\mu_1(t)$, $\nu_1(t)$ and $\mu_2(t)$, $\nu_2(t)$, the means of the two von Mises functions, evolve as in Fig. 7.6c. Such a desired behavior consists of two clusters of agents orbiting on a circle. Results are reported in Fig. 7.6d, where the time evolution $\bar{E}$ is also shown. After an initial transient, $\bar{E}$ settles to approximately 50%. For brevity, we omit the KL divergence in time, which remains below 0.3.

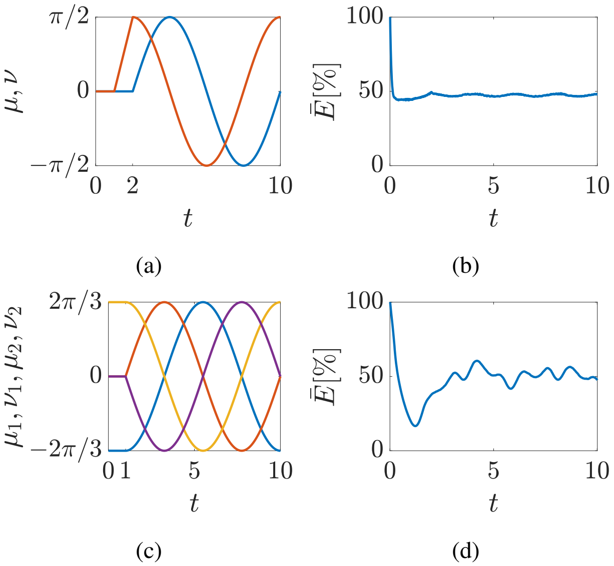

Figure 7.6: Tracking experiments. (a) Time evolution of the means of the monomodal time variant desired density to track, (b) percentage error in time during the monomodal tracking trial, (c) time evolution of the means of the two modes of the desired von Mises functions in the multimodal tracking trial (first mode blue and orange, second mode yellow and purple), and (d) percentage error in time during the multimodal tracking trial.

### 7.3.2 Results and Discussion

We considered a hybrid swarm of 4 differential drive robots and 96 virtual agents, interacting through a repulsive kernel. Assuming the group to start on a perfect square lattice (intial constant density), we tasked the swarm to aggregate according to four different desired densities, under a new 2D continuification control action. Specifically, we presented a monomodal and multimodal regulation case, where the means of the von Mises functions to achieve are time invariant, and a monomodal and multimodal tracking case, where, instead, the means of the von Mises functions to achieve are time variant.

We characterized the performance of each trial using the time evolution of the normalized $\mathcal{L}^2$ error, namely $\bar{E}$. Although the correct formation has been attained in each of the trials, we obtained our best results in the regulations scenarios (monomodal and multimodal), where the steady-state residual percentage error went below 10% and 30% respectively (Fig.s 7.4 and 7.5). Concerning the tracking cases, instead, performance was less remarkable, with $\bar{E}$ being around 50%, in both the monomodal and multimodal case (see Fig. 7.6).

Although the prescribed formation was always attained (see Figs. 7.4 and 7.5 and available videos for the tracking cases), the asymptotic convergence that is prescribed by the theory (see Section 3.4) was not accomplished. This is due to two main factors. First, we adapted the theoretical framework to experiments to cope with the periodicity assumption about the domain and with the constrained kinematic of the differential robots. Second, the inherent uncertainties and noise of the experimental set-up need also to be considered. Note that, another source of performance degradation is the finite size of the swarm. Specifically, our convergence guarantees hold in the limiting case of infinite agents. Indeed, should we numerically integrate (3.3), assuming an infinite number of agents, we would be able to reduce $\|e^F\|_2^2$ to 0.

## 7.4 Preliminary results about the experimental validation of the leader-follower framework of Chapter 5

In this section, we show some preliminary results about the experimental validation of the leader-follower density control problem that is discussed in Chapter 5.

We decided to perform such an experimental validation exploiting the Robotarium facilities [152, 203]. This choice is driven by two main factors: (*i*) the Robotarium provides up to 20 differential drive robots, which is consistently more than the ones we have in our in-house platform; (*ii*) in this way, we can demonstrate the versatility of the mixed-reality platform we propose, as it can be easily implemented in open-source facility as Robotarium.

Within the Robotarium, 20 differential drive robots with a radius of around 10 cm (GRITSBot) are able to move in a 3.2×2 m arena. Robots have a maximum linear speed of 20 cm/s, and a maximum rotational speed of 3.6 rad/s. The whole set-up in equivalent to that depicted in Fig. 7.2, and, as in our set-up, robots have an embedded controller so that they can be treated as single/double integrators.

We considered a discrete scenario similar to that discussed in Section 5.8, but assuming the domain is two-dimensional. We chose to have $N^L = 20$ differential drive robots as leaders, and $N^F = 80$ virtual followers. Followers are two-dimensional random walkers that are repelled by leaders; leaders are single integrators whose control action is computed as in Section 5.9, and then discretized via a spatial sampling, that is $\mathbf{u}_i(t) = \mathbf{U}(\mathbf{x}_i, t)$ – the system dynamics is that in (5.82), but extended to two-dimensional domains. To adapt the assumption on the periodicity of the domain to Robotarium experiments, we defined a smaller domain inside of the arena and scaled robots' positions

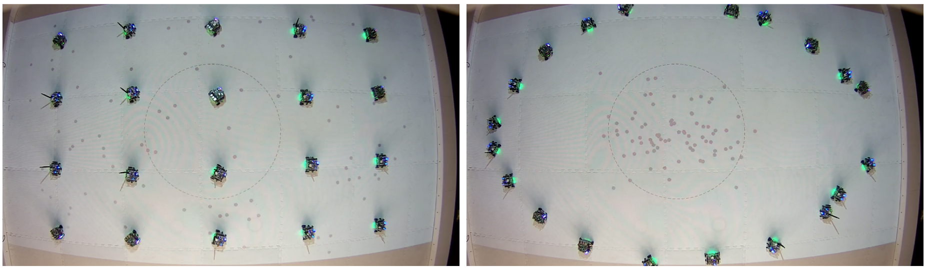

(a) $t = 0$ (b) $t = t_\mathrm{f}$

Figure 7.7: A mixed reality implementation in Robotarium of the leader-follower problem discussed in Section 5: (a) initial and (b) final condition. Virtual followers are represented as black dots. The black circle highlight the region where the desired density reaches almost 0.

with respect to this fictitious domain. As for the followers, they are allowed to cross the boundaries, being them virtual simulated agents. Leaders start equally spaced on a lattice, while followers' initial positions are randomly drawn from the uniform distribution. Densities are estimated from leaders and followers position with an ad-hoc kernel estimation method. As desired followers' distribution, we chose the Von Mises density in (3.26) with $k_1 = k_2 = 0.3$.

Results of the experimental trial are reported in Fig. 7.7, where the initial and final snapshot of the experiment are shown. It is possible to notice that virtual followers are almost all contained in the circular region at the origin of the domain (the desired density is almost 0 outside otf that region)

## 7.5 Discussion

We developed a new mixed reality, flexible, experimental environment for large-scale swarm robotics experiments with relatively small time and resources demand, and we presented the extension to higher dimensions of the continuification-based control strategy proposed in [29]. Our approach leveraged hybrid swarms of differential drive robots and virtual agents, making the size of the swarm easily scalable by the user. We demonstrated the applicability and effectiveness of our set-up for the experimental validation of the continuification-based control of swarming robots in the plane.

When experimentally implementing a macroscopic control technique with the assumption of an infinite number of agents, we reported a performance degradation, even if convergence is theoretically ensured. This is due to both implementation problems and theoretical drawbacks of the strategy. In particular, performance degradation is due to ($i$) the experimental set-up, ($ii$) the necessary adaptation of the control strategy to the kinematic constraints of the real robots and the periodicity of the domain, and ($iii$) the inherent approximation introduced by the continuum hypothesis. Current work seeks to build more differential drive robots to asses how the ratio between real robots and virtual agents influence the effectiveness of the platform, and rephrase the theoretical framework to reduce the number of adaptations to go from theory and simulations to reality.

# 8 Conclusions

Finding scalable control strategies for large-scale multi-agent systems is crucial to tackle many open problems coming from contemporary applications. Large swarms of simple robots collaboratively solving a complex task, autonomous vehicles smoothing traffic waves, and regulating the concentrations of engineered microbial consortia in synthetic biology are just a few relevant examples. All these applications live at different descriptions scales for what concerns control problems. In fact, control goals are typically defined at the level of the emerging collective behavior, but control inputs can solely be exerted at the microscopic individual level. In this Thesis, we propose a novel control framework which naturally exploits the multi-scale nature of this kind of systems.

In Chapter 2, we analyzed what, to the best of our knowledge, represents the relevant Literature regarding the subjects related to this Thesis. In particular, our overview highlighted some relevant gaps, which this Thesis aims to fill. Specifically, we remark that: ($i$) the applicability of the vast majority of existing techniques performing control design at the macroscopic level is strongly limited by the absence of methods to link macroscopic control actions and deployable control inputs; ($ii$) contributions regarding the analytical treatment of leader-follower scenarios at the macroscopic level are scarce, and it may be crucial to delve into this field so to guide the control design process in this context, for instance, understanding the needed leaders-to-followers ratio and leaders' minimal sensing and actuation capabilities; ($iii$) we are currently missing platforms for the agile experimental testing of control techniques for large-scale complex systems, hence making numerical simulations the only viable options for validation.

In Chapter 3, we developed a systematic continuification pipeline to solve density control problems regarding interacting nonlinear agents moving in periodic domains of arbitrary size. Such a control paradigm consists of three subsequent steps. After deriving a macroscopic continuum formulation for the group behavior, a macroscopic control action is developed and analytically proved to be effective. Such a control action is finally discretized onto the agents dynamics in the form of deployable control inputs. Performing control design at the macroscopic level has several advantages. Mainly, it allows to recast the system dynamics into a more compact formulation under the hypothesis of having a collective of infinite size, and, thus, effectively facing the curse of dimensionality of large-scale problems. Relying on this more amenable formulation allows to prove the convergence of the developed strategy more easily

The effectiveness of control solutions exploiting macroscopic descriptions of the ensemble dynamics typically relies on unrealistic assumptions such as unlimited sensing capabilities and absence of perturbations. In Chapter 4, we analyzed how relaxing such hypotheses affects the stability properties of our control methodology. We discovered local and bounded convergence can still be granted, demonstrating the robustness of our continuification strategy.

In Chapter 5, we extended our control framework to scenarios in which control can only be exerted through a subset of the agents in the group. Within this leader-follower scenario, we derived necessary and sufficient conditions assessing the feasibility of the problem. Such a result allows to quantify the leaders-to-followers ratio, the leaders' sensing capabilities, and the followers noisiness that makes a density control problem solvable. Then, two possible control strategies are presented, a feed-forward scheme and a reference-governor, both proved to ensure global convergence under suitable hypotheses.

This leader-follower paradigm has been readily expanded to model behavioral plasticity phenomena in Chapter 6. This biological mechanism assumes to have a subset of the agents in the group to be able to switch roles while solving a task in a collaborative manner. Our model and control solution demonstrate that the biological idea of plasticity can inform and inspire the development of future control techniques with enhanced flexibility and robustness properties.

Finally, in Chapter 7, we discussed a robotic platform we developed for the agile experimental testing of control solutions for large-scale problems and swarm robotics. This platform lives in a mixed reality context, leveraging some real differential drive robots and an arbitrary number of virtual robotic agents. This set-up allows to create swarms of arbitrary size avoiding the bottleneck of the extreme time and resources' costs of full scale experiments. The usability of our platform has been assessed by performing several experiments regarding our continuification control strategies.

## 8.1 Limitations and Future Work

The work in this Thesis does not come without limitations. Our theoretical results and proofs of convergence hold at the macroscopic scale, where the assumption of having groups of infinite size is made. As demonstrated in numerical and experimental trials, when implemented on swarms of finite size, our control methodologies still work in a satisfactory way. Nevertheless, the extent to which performance degrades in these discrete and microscopic scenarios has not been assessed. We acknowledge that analytical guarantees of convergence from the macroscopic setting to its microscopic counterpart are still missing. Such guarantees could be explored using classical works about two-scale convergence [181] and asymptotic formal analysis [182]

Also, we always rely on the kinematic assumption for modeling the behavior of the agents, resulting in first order dynamical models and, moreover, agents' interactions are always assumed to take place in an all-to-all fashion. Although the intensity of the interactions decays with the distance between the agents as in proximity networks, the possibility of topological interactions taking place through a complex network structure has not been assessed. The extension of the proposed mathematical framework to second order models accounting for conservation of momentum and energy are the subject of ongoing research, together with the inclusion of graphons to account for topological interactions.

Finally, our mixed reality platform for swarm robotics experiments offers an intermediate level of abstraction between simulations and full-scale experiments, whose importance cannot be overlooked.

## 8.2 List of publications

### Journal Papers

1. A. Giusti†, **G.C. Maffettone**†, D. Fiore, M. Coraggio, M. di Bernardo, “Distributed control for geometric pattern formation of large-scale multirobot systems", Frontiers in Robotics and Artificial Intelligence, 2023

2. **G.C. Maffettone**, M. Porfiri, M. di Bernardo, “Continuification control of large-scale multiagent systems under limited sensing and structural perturbations", IEEE Control Systems Letters, vol. 7, pp 2425-2430, 2023

3. **G.C. Maffettone**, A. Boldini, M. di Bernardo, M. Porfiri, “Continuification control of large-scale multiagent systems in a ring", IEEE Control Systems Letters, vol. 7, pp. 841-846, 2023

4. **G.C. Maffettone**, L. Liguori, E. Palermo, M. di Bernardo, M. Porfiri, “Mixed Reality Environment and High-Dimensional Continuification Control For Swarm Robotics", accepted for pubblication on IEEE Transactions on Control Systems Technology

† authors contributed equally

### Refereed Conference Papers

1. **G.C. Maffettone**, M. di Bernardo, M. Porfiri, “High-dimensional continuification control of large-scale multi-agent systems under limited sensing and perturbations", Accepted for pubblication in the proceedings of, and presentation at, the 63rd Conference on Decision and Control (Milan, December 2024), arxiv.

### Preprints

1. **G.C. Maffettone**, A. Boldini, M. di Bernardo, M. Porfiri, “Leader-Follower Density Control of Spatial Dynamics in Large-Scale Multi-Agent Systems", under review in IEEE Transactions on Automatic Control, 2024, arxiv

2. B. di Lorenzo, **G.C. Maffettone**, M. di Bernardo, “A continuification-based solution for the shepherding control problem", submitted to be published in the

proceedings of, and presentation at, the 2025 European Control Conference. arxiv

## In preparation

We are currently preparing the manuscript

1. G.C. Maffettone, A. Boldini, M. Porfiri, M. di Bernardo, “A continuum mixture of leaders and followers: enhanced flexibility and robustness under behavioral plasticity regimes" (this details the subjects in Chapter 6).

## Appendix A

# Interaction kernel periodization

Periodic interaction kernels $\mathbf{f}$ are obtained from the periodization of standard non-periodic kernels $\hat{\mathbf{f}}$,

$$\mathbf{f}(\mathbf{x}) = \sum_{\Bbbk \in \mathbb{Z}^d} \hat{\mathbf{f}}(\mathbf{x} + 2\mathbf{k}\pi) \tag{A.1}$$

where $\Bbbk$ is a multi-index and $\mathbf{k}$ is its related row vector.

## One dimensional kernel periodization

When $d = 1$, some closed form for the periodic kernels can be found. Here we provide examples for the repuslive and Morse kernels.

**Repulsive kernel** The non-periodic repulsive kernel is in the form

$$\hat{f}(x) = \operatorname{sgn}(x) e^{-\frac{|x|}{L}}. \tag{A.2}$$

Note that we utilize a length-scale $L$ while fixing the domain to $[-\pi, \pi]$. Periodization leads to

$$f(x) = \sum_{k=-\infty}^{\infty} \operatorname{sgn}(x + 2k\pi) e^{-\frac{|x+2k\pi|}{L}}. \tag{A.3}$$

By separating the infinite series into two other infinite series based on the sign of $x + 2k\pi$ and computing each of these series individually leads to

$$f(x) = \frac{1}{e^{\frac{2\pi}{L}} - 1} \operatorname{sgn}(x) \left[ e^{\frac{2\pi - |x|}{L}} - e^{\frac{|x|}{L}} \right]. \tag{A.4}$$

**Morse kernel** The non periodic Morse kernel is an attractive-repulsive kernel in the form

$$\hat{f}(x) = \operatorname{sgn}(x)\left[\frac{1}{L_r}\mathrm{e}^{-\frac{|x|}{L_r}} - \alpha\frac{1}{L_a}\mathrm{e}^{-\frac{|x|}{L_a}}\right] = \frac{1}{L_r}\hat{f}_r(z) - \frac{\alpha}{L_a}\hat{f}_a(z), \tag{A.5}$$

where we fixed

$$\hat{f}_i(z) = \operatorname{sgn}(x)\mathrm{e}^{-\frac{|x|}{L_i}}. \tag{A.6}$$

Following the same steps proposed for the repulsive kernel, we recover the periodic Morse kernel

$$f(x) = \frac{1}{L_r}f_r(z) - \frac{\alpha}{L_a}f_a(z), \tag{A.7}$$

with

$$f_i(z) = \frac{1}{\mathrm{e}^{\frac{2\pi}{L_i}} - 1}\operatorname{sgn}(z)\left[\mathrm{e}^{\frac{2\pi-|z|}{L_i}} - \mathrm{e}^{\frac{|z|}{L_i}}\right]. \tag{A.8}$$

## Higher dimensional kernel periodization

When $d > 1$ no closed forms for the periodc kernels has been found. Hence, when needed, they are approximated truncating the infinite series in (A.1). For instance, if $d = 2$, and $\mathbf{x} = [x_1, x_2]$, we have

$$\mathbf{f}(x_1, x_1) \approx \sum_{k_1,k_2=-M}^{M} \hat{\mathbf{f}}(x_1 + 2k_1\pi, x_2 + 2k_2\pi), \tag{A.9}$$

where $k_1$ and $k_2$ are the components of $\mathbf{k}$, and $M$ is the truncation order.

# Appendix B

# Deconvolution

**Repulsive kernel** Given the repulsive kernel (5.3) and a density function $\rho : \mathcal{S} \to \mathbb{R}_{\geq 0}$

$$\begin{aligned} \phi(x) = (f * \rho)(x) = \frac{1}{\mathrm{e}^{\frac{2\pi}{L}} - 1} \Bigg[ & \mathrm{e}^{\frac{2\pi - x}{L}} \int_{-\pi}^{x} \mathrm{e}^{\frac{y}{L}} \rho(y)\,\mathrm{d}y - \mathrm{e}^{\frac{x}{L}} \int_{-\pi}^{x} \mathrm{e}^{-\frac{y}{L}} \rho(y)\,\mathrm{d}y \\ & - \mathrm{e}^{\frac{2\pi + x}{L}} \int_{x}^{\pi} \mathrm{e}^{-\frac{y}{L}} \rho(y)\,\mathrm{d}y + \mathrm{e}^{-\frac{x}{L}} \int_{x}^{\pi} \mathrm{e}^{\frac{y}{L}} \rho(y)\,\mathrm{d}y \Bigg]. \end{aligned} \tag{B.1}$$

Differentiating twice with respect to the space variable yields

$$\phi_{xx} = \frac{\phi}{L^2} + 2\rho_x. \tag{B.2}$$

Thus, by integration, we can retrieve $\rho$ as follows:

$$\rho(x) = \frac{1}{2} \int \left( \phi_{xx} - \frac{\phi}{L^2} \right) \mathrm{d}x + B, \tag{B.3}$$

where $B$ is an arbitrary constant.

Notice that the deconvolution operation can be performed also for more complex periodic interaction kernels, which are not considered in this work. For instance, we refer the reader to [98] for the case of Morse interactions.

## Appendix C

# Some more theoretical results regarding Chapter 5

## C.1 Feasibility analysis with followers-followers interactions

Assume the system dynamics can be described by (5.1a) and the modified followers equation given by

$$\rho_t^F(x,t) + \left[\rho^F(x,t)\left(v^{FF}(x,t) + v^{FL}(x,t)\right)\right]_x = D\rho_{xx}^F(x,t), \tag{C.1}$$

with $v^{FF}(x,t) = (f^F * \rho^F)(x,t)$ modeling follower-follower interactions through the odd periodic kernel $f^F$. Notice that $f^F$ can model spatial behaviors that are also different from the one embedded in $f$. In particular, it can describe pure repulsion or attraction, and repulsion (attraction) at long range and attraction (repulsion) at short range. The procedure described in Section 5.4 can be easily adapted to this modified scenario. In particular, given a desired followers' density $\bar{\rho}^F(x)$ (such that $\bar{\rho}^F(x) \neq 0$ for all $x \in \mathcal{S}$), we can compute the velocity field $\bar{v}^{LF}(x)$ ensuring $\bar{\rho}^F(x)$ is a solution of (C.1), that is,

$$\bar{v}^{LF}(x) = \frac{D\bar{\rho}_x^F(x) - \bar{\rho}^F(x)\bar{v}^{FF}(x) + A}{\bar{\rho}^F(x)}, \tag{C.2}$$

with $\bar{v}^{FF} = (f^F * \bar{\rho}^F)$ and $A$ being an integration constant. The integration constant $A$ is not free to choose, as similarly to (5.12), the Fubini's theorem for convolutions needs

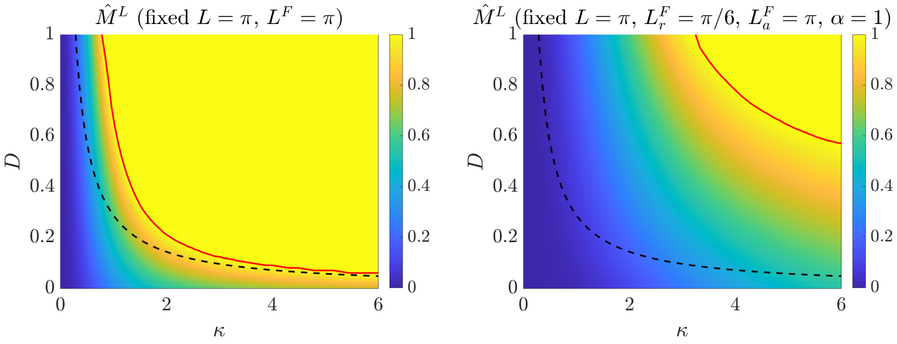

(a)

(b)

Figure C.1: Feasibility plots: $\widehat{M}^L$ for fixed $L$ and (a) repulsive follower-follower interaction, (b) Morse follower-follower interaction. In red we show the curve indicating when $\widehat{M}^L$ becomes greater than 1. In dashed black, we report the feasibility threshold for the analogous case in Fig. 5.1a (no follower-follower interaction).

to be satisfied. Specifically, exploiting that

$$\int_S \bar{v}^{FF}(x)\,\mathrm{d}x = 0 \tag{C.3}$$

by construction (because of the Fubini's theorem for convolutions with an odd kernel), it needs to be $A = 0$, making

$$\bar{v}^{LF}(x) = \frac{D\bar{\rho}_x^F(x)}{\bar{\rho}^F(x)} - \bar{v}^{FF}(x). \tag{C.4}$$

Then, by decovolution, we recover $\bar{\rho}^L$ as in (5.15). Then, Theorem (5.1) still holds, but with a modified $h(x)$, that is

$$h(x) = \frac{-\frac{D}{2}g_1(x) + \frac{D}{2L^2}g_2(x) - \frac{DC}{4\pi L^2} + \frac{\hat{v}_x^{FF}(x)}{2} - \frac{H(x)}{2L^2} + \frac{F}{4\pi L^2}}{\frac{1}{2\pi} + \frac{\hat{v}_x^{FF}(x)}{2} - \frac{H(x)}{2L^2} + \frac{F}{4\pi L^2}}, \tag{C.5}$$

with $g_1$, $g_2$ and $C$ defined as in Section 5.4 and

$$\hat{v}^{FF}(x) = (f^F * \hat{\rho}^F)(x) \tag{C.6}$$

$$H(x) = \int \hat{v}^{FF}(x)\,\mathrm{d}x \tag{C.7}$$

$$F = \int_S H(x)\,\mathrm{d}x. \tag{C.8}$$

### Example

Using the same set-up of Section 5.4.1, we consider the case of having follower-follower interactions. Specifically we fix $L = \pi$ for $v^{FL}$ and we consider the follower-followers kernel to be $(i)$ the repulsive one in (3.24) with characteristic length $L^F = \pi$, and $(ii)$ the periodic Morse kernel in (A.7) with $L_a = L_a^F = \pi$, $L_r = L_r^F = \pi/6$ and $\alpha = 1$ (modelling long-range attraction and short range repulsion). We report the feasibility plots in Fig. C.1. For the sake of comparison, in both the scenarios we see an increase in the area of the feasibility region ($\widehat{M}^L < 1$), with respect to the analogous scenario with non interacting followers (see Fig. 5.1a). Such an increase is remarkably bigger when followers interact through a Morse kernel, underlying a flocking mechanism.

## C.2 Leader-follower density control with unfeasible desired densities

When the followers' desired density $\bar{\rho}^F$, together with the the characteristic parameters $(L, D)$, are such that the problem is unfeasible, it means there is not a leaders' desired density $\bar{\rho}^L$ fulfilling Definition 5.1. In such a scenario, we can choose $B$ in (5.15) according to

$$\begin{aligned} B = \arg\min_{B} \int_S \bar{\rho}^L(x)\,\mathrm{d}x \\ \text{s.t. } \bar{\rho}^L(x) \geq 0. \end{aligned} \tag{C.9}$$

Such a choice of $B$ consists in a leaders' desired density that is positive, sums to the smallest possible mass $M > M^L$, and implies $\min[\bar{\rho}^L] = 0$. Then, we can normalize $\bar{\rho}^L$ so that it sums to $M^L$, that is

$$\tilde{\rho}^L(x) = Z\,\bar{\rho}^L(x), \tag{C.10}$$

with

$$Z = \frac{M^L}{\int_S \bar{\rho}^L(x)\,\mathrm{d}x} \in (0, 1). \tag{C.11}$$

The resulting velocity field that can be exerted by $\tilde{\rho}^L$ is a scaled version of $\bar{v}^{FL}$, that is

$$\tilde{v}^{FL}(x) = (f * \tilde{\rho}^L)(x) = Z\,(f * \bar{\rho}^L)(x) = Z\,\bar{v}^{FL}(x). \tag{C.12}$$

We can still use the control scheme proposed in Chapter 5, assuming leaders can only displace such that $\tilde{v}^{FL}$ is exerted, proving bounded convergence.

**Remark C.1.** *In such a scenario, the reference-governor scheme described in Chapter 5 cannot be implemented as the choice of* $\alpha$ *in (5.76) will always return 0 because* $\min[\bar{\rho}^L] = 0$.

**Theorem C.1** (Bounded convergence for non-feasible scenarios)**.** *When the feasibility condition is not fulfilled, and if* $\|g_1\|_\infty \leq 2/Z$ *and* $\bar{\rho}^F_{xx} \in L^2$, $\rho^F$ *converges towards* $\bar{\rho}$ *with a bounded error.*

*Proof.* When we plug (C.12) into (5.1b), we obtain the following error dynamics:

$$e^F_t(x,t) = De^F_{xx}(x,t) - ZD\left[e^F(x,t)\frac{\bar{\rho}^F_x(x)}{\bar{\rho}^F(x)}\right]_x + D(Z-1)\bar{\rho}^F_{xx}(x), \tag{C.13}$$

with its own initial and periodic boundary conditions. Let us consider the Lyapunov functional $\|e^F\|_2^2$. We get

$$\begin{aligned}\left(\|e^F(x,t)\|_2^2\right)_t &= 2\int_S e^F(x,t)e^F_t(x,t)\,\mathrm{d}x = 2D\int_S e^F(x,t)e^F_{xx}(x,t)\,\mathrm{d}x\\ &- 2ZD\int_S e^F(x,t)\left[e^F(x,t)\frac{\bar{\rho}^F_x(x,t)}{\bar{\rho}^F(x)}\right]_x\,\mathrm{d}x + 2D(Z-1)\int_S e^F(x,t)\bar{\rho}^F_{xx}(x)\,\mathrm{d}x,\end{aligned} \tag{C.14}$$

that, by several integration by parts can be rewritten as

$$\begin{aligned}\left(\|e^F(x,t)\|_2^2\right)_t = -2D\|e^F_x(\cdot,t)\|_2^2 - ZD\int_S \left(e^F(x,t)\right)^2 g_1(x)\,\mathrm{d}x&\\ + 2D(Z-1)\int_S e^F(x,t)\bar{\rho}^F_{xx}(x)\,\mathrm{d}x,&\end{aligned} \tag{C.15}$$

Because of the Hölder's inequality, we can establish the bound

$$\begin{aligned}\left|\int_S e^F(x,t)\bar{\rho}^F_{xx}(x)\,\mathrm{d}x\right| \leq \int_S \left|e^F(x,t)\bar{\rho}^F_{xx}(x)\right|\,\mathrm{d}x = \left\|e^F(\cdot,t)\bar{\rho}^F_{xx}(x)\right\|_1 \leq&\\ \leq \left\|e^F(\cdot,t)\right\|_2\left\|\bar{\rho}^F_{xx}(x)\right\|_2.&\end{aligned} \tag{C.16}$$

Using (C.16), the Poincaré-Wirtinger's inequality (see Lemma 1.4) and the Hölder's inequality (see Lemma 1.1), we get

$$\left(\|e^F(x,t)\|_2^2\right)_t \leq D\left(-2+Z\|g_1(x)\|_\infty\right)\|e^F(\cdot,t)\|_2^2 + 2D|Z-1|\|\bar{\rho}_{xx}^F(x)\|_2\|e^F(\cdot,t)\|\|_2. \tag{C.17}$$

Imposing $\eta = \|e^F\|_2^2$, we can equivalently rewrite

$$\eta_t \leq -a\eta + b\sqrt{\eta}, \tag{C.18}$$

where

$$a = D\left(-2+Z\|g_1(x)\|_\infty\right), \tag{C.19}$$

$$b = 2D|Z-1|\|\bar{\rho}_{xx}^F(x)\|_2. \tag{C.20}$$

Under the theorem hypothesis, we know that $a \geq 0$. Then, using the comparison lemma (see Lemma 1.5), bounded convergence is proved, as the bounding system has a globally asymptotically stable equilibrium point in $b^2/a^2$. ■

## Appendix D

# Numerical scheme for the integration of continuified problems

To integrate (3.12), representing the controlled model in the limit of infinite agents, we use a finite volume scheme, which naturally accounts for conservation laws [204]. We divide the domain $\Omega$ into $N_C$ cells $C_i$ $(i = 1, \ldots, N_C)$ of uniform volume $\Delta\mathrm{x}$, and consider the average value of the density at time $t_n$

$$Q_i^n = \frac{1}{\Delta\mathrm{x}} \int_{C_i} \rho(\mathbf{x}, t_n)\,\mathrm{d}\mathbf{x}. \tag{D.1}$$

The discrete time evolution of this quantity is given by

$$Q_i^{n+1} = Q_i^n - \frac{\Delta t}{\Delta\mathrm{x}} \sum_{j=1}^{d} (F_{j,i+1/2}^n - F_{j,i-1/2}^n) \tag{D.2}$$

where $\Delta t$ is the time integration step and $F_{j,i+1/2}^n$ and $F_{j,i-1/2}^n$ are the numerical fluxes on the interfaces of cell $C_i$ in the $j$ dimension. We computed the numerical fluxes using the Lax-Friedrichs method.

## Appendix E

# Some more theoretical results regarding Chapter 6

In this Appendix, we give some theoretical result that are used throughout Chapter 6.

## E.1 Global stability with full plasticity

In the absence of non-reactive followers (that is, $p = 1$, or, equivalently $\Phi^F = 0$), the control solution we propose ensure global stability in some regions of of the parameters' space.

Specifically, the results of Theorem 6.2 can be rephrased so to ensure the strict positivity of $\rho^L$ and $\rho^F$ for any $x \in \mathcal{S}$ and $t \in \mathbb{R}_{\geq 0}$.

**Theorem E.1** (Analytical solution of for $\rho^L$ and $\rho^F$ when $p = 1$)**.** *When $p = 1$ and $q$ and $u$ are chosen as in Section 6.2.3 it results*

$$\begin{aligned} 2\rho^L(x,t) = \bar{\rho}(x)(1-\mathrm{e}^{-Kt}) + \rho_0(x)\mathrm{e}^{-Kt} + \rho_0^*(x)\mathrm{e}^{-at} + \bar{\rho}(x)\frac{b}{a}(1-\mathrm{e}^{-at}) \\ + \frac{b}{a-K}\left[\rho_0(x) - \bar{\rho}(x)\right]\left(\mathrm{e}^{-Kt} - \mathrm{e}^{-at}\right), \end{aligned} \tag{E.1a}$$

$$\begin{aligned} 2\rho^F(x,t) = \bar{\rho}(x)(1-\mathrm{e}^{-Kt}) + \rho_0(x)\mathrm{e}^{-Kt} - \rho_0^*(x)\mathrm{e}^{-at} - \bar{\rho}(x)\frac{b}{a}(1-\mathrm{e}^{-at}) \\ - \frac{b}{a-K}\left[\rho_0(x) - \bar{\rho}(x)\right]\left(\mathrm{e}^{-Kt} - \mathrm{e}^{-at}\right), \end{aligned} \tag{E.1b}$$

*where* $\rho_0^* = \rho_0^L - \rho_0^F$, $a = K_{FL} + K_{LF}$, *and* $b = K_{FL} - K_{LF}$.

*Proof.* For full plasticity, that is $p = 1$, the model (6.1) simplifies to

$$\rho_t^L(x,t) + \left[\rho^L(x,t)u(x,t)\right]_x + \left[\rho^L(x,t)(f*\rho)(x,t)\right]_x = D\rho_{xx}^L(x,t) + q(x,t) \tag{E.2a}$$
$$\rho_t^F(x,t) + \left[\rho^F(x,t)(f*\rho)(x,t)\right]_x = D\rho_{xx}^F(x,t) - q(x,t), \tag{E.2b}$$

with $\rho = \rho^L + \rho^F$. This problem can be equivalently studied in terms of $\rho$ and $\rho^* = \rho^L - \rho^F$, thanks to the change of variables

$$\rho^L(x,t) = \frac{\rho(x,t) + \rho^*(x,t)}{2} \tag{E.3a}$$
$$\rho^F(x,t) = \frac{\rho(x,t) - \rho^*(x,t)}{2}. \tag{E.3b}$$

Fixing $u$ and $q$ as detailed in Section 6.2.3, it results

$$\rho_t(x,t) = -K\,\rho(x,t) + K\,\bar{\rho}(x) \tag{E.4}$$
$$\rho_t^*(x,t) = -a\,\rho^*(x,t) + b\,\rho(x,t). \tag{E.5}$$

The dynamics of $\rho$ is linear and independent from that of $\rho^*$, hence it can be analytically solved as in (6.15). Thus, it results that the dynamics of $\rho^*$ is linear and influenced by $\rho$ that is known at any $x$ and $t$. The solution for (E.5) is then

$$\rho^*(x,t) = \rho_0^*(x)\exp(-at) + \int_0^t \exp[-a(t-\tau)]b\rho(x,\tau)\,\mathrm{d}\tau. \tag{E.6}$$

Substituting (6.15) and (E.6) into (E.3), we can recover the Theorem's thesis. ■

**Theorem E.2.** *Assuming* $\rho_0^L > 0$ *for any* $x \in \mathcal{S}$, $b < 0$, $a < K$ *and* $|b/(a-K)| < 1$, $\rho^L, \rho^F > 0$ *for any* $x \in \mathcal{S}$ *and* $t \in \mathbb{R}_{\geq 0}$.

*Proof.* The leaders density in (E.1a) can be rewritten as

$$2\rho^L(x,t) = \bar{\rho}(x)H_1(t) + H_2(x,t), \tag{E.7}$$

with

$$H_1(t) = 1 + \frac{b}{a} - \exp(-Kt)\left(\frac{b}{a-K} + 1\right) + \exp(-at)\left(\frac{b}{a-K} - \frac{b}{a}\right), \tag{E.8}$$

$$H_2(x,t) = \rho_0^*(x)\exp(-at) + \rho_0(x)\left[\exp(-Kt) + \frac{b}{a-K}\left(\exp(-Kt) - \exp(-at)\right)\right]. \tag{E.9}$$

Regarding $H_1(t)$, choosing $|b/(a-K)| < 1$ guarantees that $1 + b/a$ is strictly positive (notice also that, by construction, $|b/a| < 1$). The last two summands of (E.8) are negative and monotonically decrease in absolute value to 0. Hence, they attain their maximum absolute value for $t = 0$. Since we also have $H_1(0) = 0$, we know that $H_1(t) \geq 0 \; \forall \, t \in \mathbb{R}_{\geq 0}$.

Regarding $H_2(x,t)$, it can be rewritten as

$$\begin{aligned} H_2(x,t) = \rho_0^L(x)\exp(-Kt)\left(1 + \frac{b}{a-K}\right) + \rho_0^L(x)\exp(-at)\left(1 - \frac{b}{a-K}\right) \\ + \rho_0^F(x)\left(1 + \frac{b}{a-K}\right)\left[\exp(-Kt) - \exp(-at)\right]. \end{aligned} \tag{E.10}$$

Choosing $|b/(a-K)| < 1$, and recalling $\rho_0^L(x) > 0 \; \forall \, x \in \mathcal{S}$ by assumption, ensures the first two summands are strictly positive. The last summand is non-negative if $a > K$.

Under the mild assumptions of choosing $b < 0$, $a > K$, $|b/(a-K)| < 1$, and $\rho_0^L(x) > 0$ makes $H_1 \geq 0 \; \forall \, t \in \mathbb{R}_{\geq 0}$ , and $H_2(x,t) > 0 \; \forall \, x \in \mathcal{S}$ and $t \in \mathbb{R}_{\geq 0}$, showing the leaders' density always remains strictly positive.

We remark that, under the additional assumption of $\rho_0^F > 0$, $\rho^F$ remains strictly positive as well. We can rewrite (E.1b) as

$$\rho^F(x,t) = \bar{\rho}(x) Y_1(t) + Y_2(x,t), \tag{E.11}$$

with

$$Y_1(t) = 1 - \frac{b}{a} - \exp(-Kt)\left(1 - \frac{b}{a-K}\right) + \exp(-at)\left(\frac{b}{a} - \frac{b}{a-K}\right), \tag{E.12}$$

$$Y_2(x,t) = -\rho_0^*(x)\exp(-at) + \rho_0(x)\left[\exp(-Kt) - \frac{b}{a-K}\left(\exp(-Kt) - \exp(-at)\right)\right]. \tag{E.13}$$

$Y_1$ is always non-negative, as all its summands are positive except for the third one, which is negative, attains its maximum value at $t = 0$ and then monotonically decreases in absolute value to 0. Since $Y_1(0) = 0$, then $Y_1 \geq 0 \; \forall \, t \in \mathbb{R}_{\geq 0}$. Equation (E.13) can be rewritten as

$$Y_2(x,t) = \rho_0^L(x)\left(1-\frac{b}{a-K}\right)[\exp(-Kt)-\exp(-at)] \\ + \rho_0^F(x)\exp(-at)\left(1+\frac{b}{a-K}\right)\rho_0^F(x)\exp(-Kt)\left(1-\frac{b}{a-K}\right), \quad \text{(E.14)}$$

resulting in only strictly positive summands if $\rho_0^F > 0$. Being $Y_1$ always non-negative and $Y_2$ always positive, $\rho^F$ always remains strictly positive. ■

**Remark E.1.** *The cases $a = b = 0$, and $K \to a$ can be analytically studied, but are out of the scope of the Thesis.*

By letting the time go to infinity in (E.1a) and (E.1b), we recover the steady-state expressions for the leaders' and followers' densities, that is

$$\rho_{ss}^L(x) = \frac{\bar{\rho}(x)}{2}\left(1+\frac{b}{a}\right), \quad \text{(E.15a)}$$

$$\rho_{ss}^F(x) = \frac{\bar{\rho}(x)}{2}\left(1-\frac{b}{a}\right). \quad \text{(E.15b)}$$

We remark that $|b/a| < 1$ by construction. By integrating such expression over $\mathcal{S}$, we recover the steady-state leaders and followers mass, that is

$$M_{ss}^L = \frac{1}{2}\left(1+\frac{b}{a}\right), \quad \text{(E.16a)}$$

$$M_{ss}^F = \frac{1}{2}\left(1-\frac{b}{a}\right). \quad \text{(E.16b)}$$

Notice that, a negative value of $b$ means the leaders reaction into followers is faster than the one of followers into leaders. This results in having $M_{ss}^L < M_{ss}^F$.

## E.2 Steady-state solution for non-reactive followers

**Theorem E.3.** *If $\rho(x,t) = \bar{\rho}(x)$, (6.1c) admits only the steady-state solution*

$$\bar{\eta}^F(x) = \frac{\Phi^F}{\int_{\mathcal{S}} h(x)\,\mathrm{d}x}h(x), \quad \text{(E.17)}$$

*with $h$ defined as in (6.20).*

*Proof.* Substituting $\eta_t^F = 0$, $\eta^F(x,t) = \bar{\eta}^F(x)$, and $\rho(x,t) = \bar{\rho}(x)$ into (6.1c) leads us to

$$D\bar{\eta}_{xx}^F(x) - \left[\bar{\eta}^F(x)(f * \bar{\rho})(x)\right]_x = 0. \tag{E.18}$$

Integrating this in space and isolating $\bar{\eta}^F$ at first member, yields to

$$\bar{\eta}_x^F(x) = \frac{\bar{\eta}^F(x)(f * \bar{\rho})(x)}{D} + A, \tag{E.19}$$

where $A$ is the integration constant. Equation (E.19) is a linear one-dimensional ODE with non-constant coefficients. Its solution ca be written as

$$\begin{aligned}\bar{\eta}^F(x) = B\exp\left\{\frac{1}{D}\int (f * \bar{\rho})(x)\,\mathrm{d}x\right\} + \\ + A\exp\left\{\frac{1}{D}\int (f * \bar{\rho})(x)\,\mathrm{d}x\right\}\int \exp\left\{\frac{1}{D}\int (f * \bar{\rho})(y)\,\mathrm{d}y\right\}\mathrm{d}x.\end{aligned} \tag{E.20}$$

where $B$ is an integration constant.

The first term at second member of (E.20) is positive, and it is also periodic (it is the exponential of a periodic function). Notice that $f * \bar{\rho}$ is periodic as the result of a circular convolution, and it sums to 0 when integrated over $\mathcal{S}$ for the Fubini's theorem for convolutions. Hence the integral of $f * \bar{\rho}$ is itself periodic. The second term at second member of (E.20), instead, cannot be periodic unless $A = 0$, since

$$\exp\left\{\frac{1}{D}\int (f * \bar{\rho})(y)\,\mathrm{d}y\right\}$$

is periodic, but it cannot sum to 0 (as an exponential, it is always positive). It follows that it needs to be $A = 0$.

For (E.20) (with $A = 0$) to sum to the non-reactive followers' mass $\Phi^F$, it must be $B = \Phi_F / \int_S h(x)\,\mathrm{d}x$, yielding the theorem's claim. ■

**Remark E.2.** *We remark that* (E.17) *is positive by construction, as h is an exponential (see* (6.20)*), and*

$$\frac{\Phi_F}{\int_S h(x)\,\mathrm{d}x} > 0$$

*by construction.*

## E.3 No diffusivity affecting the population's dynamics

Here we study problem (6.1) fixing $D = 0$, that is, no diffusion is affecting the agents' dynamics. For the control problem in Section 6.2.2 to be solvable, (6.1c) (with $D = 0$) should have a steady-state solution, $\bar{\eta}^F$, for $\rho = \bar{\rho}$, that is

$$\left[\bar{\eta}^F(x)(f * \bar{\rho})(x)\right]_x = 0. \tag{E.21}$$

By a spatial integration, it must be

$$\bar{\eta}^F(x)(f * \bar{\rho})(x) = A, \tag{E.22}$$

where $A$ is an integration constant. For Fubini's theorem for convolutions, we know that, being $f$ odd by construction, it should be

$$\int_{\mathcal{S}} (f * \bar{\rho})(x)\,\mathrm{d}x = \int_{\mathcal{S}} f(x)\,\mathrm{d}x \int_{\mathcal{S}} \bar{\rho}(x)\,\mathrm{d}x = 0. \tag{E.23}$$

Thus, either $(i)$ $f * \bar{\rho} = 0\ \forall x \in \mathcal{S}$, or $(ii)$ $f * \bar{\rho}$ switches sign in $\mathcal{S}$, and it is 0 on a set of finite points. The case $(i)$ holds only for density profiles which are equilibrium configurations of the system, as, for example, constant profiles. In such scenarios, the control problem becomes trivial. In case $(ii)$, (E.22) can hold only if $A = 0$, as $f * \bar{\rho}$ is 0 on a finite set of points. This means

$$\bar{\eta}^F(x)(f * \bar{\rho})(x) = 0. \tag{E.24}$$

Such a relation can hold, only for $\bar{\eta}^F = 0\ \forall x \in \mathcal{S}$, meaning that, the problem cannot account for non-reactive followers if $D = 0$.

# Bibliography

[1] S. Boccaletti, V. Latora, Y. Moreno, M. Chavez, and D. U. Hwang, “Complex networks: Structure and dynamics,” *Physics Reports*, vol. 424, no. 4-5, pp. 175–308, 2006.

[2] D. Weihs, “Hydromechanics of fish schooling,” *Nature*, vol. 241, no. 5387, pp. 290–291, 1973.

[3] D. Pavlov, A. Kasumyan *et al.*, “Patterns and mechanisms of schooling behavior in fish: a review,” *Journal of Ichthyology*, vol. 40, no. 2, p. S163, 2000.

[4] F. Cucker and S. Smale, “Emergent behavior in flocks,” *IEEE Transactions on Automatic Control*, vol. 52, no. 5, pp. 852–862, 2007.

[5] A. Cavagna, A. Cimarelli, I. Giardina, G. Parisi, R. Santagati, F. Stefanini, and M. Viale, “Scale-free correlations in starling flocks,” *Proceedings of the National Academy of Sciences*, vol. 107, no. 26, pp. 11 865–11 870, 2010.

[6] M. Ballerini, N. Cabibbo, R. Candelier, A. Cavagna, E. Cisbani, I. Giardina, A. Orlandi, G. Parisi, A. Procaccini, M. Viale *et al.*, “Empirical investigation of starling flocks: a benchmark study in collective animal behaviour,” *Animal behaviour*, vol. 76, no. 1, pp. 201–215, 2008.

[7] R. Avinery, K. O. Aina, C. J. Dyson, H.-S. Kuan, M. D. Betterton, M. A. Goodisman, and D. I. Goldman, “Agitated ants: regulation and self-organization of incipient nest excavation via collisional cues,” *Journal of the Royal Society Interface*, vol. 20, no. 202, p. 20220597, 2023.

[8] M. Porfiri, P. De Lellis, E. Aung, S. Meneses, N. Abaid, J. S. Waters, and S. Garnier, “Reverse social contagion as a mechanism for regulating mass behaviors in highly integrated social systems,” *PNAS nexus*, vol. 3, no. 7, 2024.

[9] S. Goss and J.-L. Deneubourg, “Autocatalysis as a source of synchronised rhythmical activity in social insects,” *Insectes Sociaux*, vol. 35, no. 3, pp. 310–315, 1988.

[10] C. Calabrese, M. Lombardi, E. Bollt, P. De Lellis, B. G. Bardy, and M. Di Bernardo, “Spontaneous emergence of leadership patterns drives synchronization in complex human networks,” *Scientific Reports*, vol. 11, no. 1, pp. 1–12, 2021.

[11] S. Shahal, A. Wurzberg, I. Sibony, H. Duadi, E. Shniderman, D. Weymouth, N. Davidson, and M. Fridman, “Synchronization of complex human networks,” *Nature Communications*, vol. 11, no. 1, pp. 1–10, 2020.

[12] W. Mao, Z. Zhao, Z. Chang, G. Min, and W. Gao, “Energy-efficient industrial internet of things: Overview and open issues,” *IEEE transactions on industrial informatics*, vol. 17, no. 11, pp. 7225–7237, 2021.

[13] F. Blaabjerg, R. Teodorescu, M. Liserre, and A. V. Timbus, “Overview of control and grid synchronization for distributed power generation systems,” *IEEE Transactions on industrial electronics*, vol. 53, no. 5, pp. 1398–1409, 2006.

[14] R. M. D’Souza, M. di Bernardo, and Y.-Y. Liu, “Controlling complex networks with complex nodes,” *Nature Reviews Physics*, vol. 5, no. 4, pp. 250–262, 2023.

[15] R. E. Stern, S. Cui, M. L. Delle Monache, R. Bhadani, M. Bunting, M. Churchill, N. Hamilton, H. Pohlmann, F. Wu, B. Piccoli *et al.*, “Dissipation of stop-and-go waves via control of autonomous vehicles: Field experiments,” *Transportation Research Part C: Emerging Technologies*, vol. 89, pp. 205–221, 2018.

[16] C.-H. Shao, P.-C. Shao, and F.-M. Kuo, “Stampede events and strategies for crowd management,” *Journal of Disaster Research*, vol. 14, no. 7, pp. 949–958, 2019.

[17] A. Lama and M. di Bernardo, “Shepherding and herdability in complex multiagent systems,” *Physical Review Research*, vol. 6, no. 3, p. L032012, 2024.

[18] N. Loy, M. Raviola, and A. Tosin, “Opinion polarization in social networks,” *Philosophical Transactions of the Royal Society A*, vol. 380, no. 2224, p. 20210158, 2022.

[19] P. Bolzern, P. Colaneri, and G. De Nicolao, “Opinion dynamics in social networks: The effect of centralized interaction tuning on emerging behaviors,” *IEEE transactions on computational social systems*, vol. 7, no. 2, pp. 362–372, 2020.

[20] N. K. Long, K. Sammut, D. Sgarioto, M. Garratt, and H. A. Abbass, “A comprehensive review of shepherding as a bio-inspired swarm-robotics guidance approach,” *IEEE Transactions on Emerging Topics in Computational Intelligence*, vol. 4, no. 4, pp. 523–537, 2020.

[21] M. Lachowicz, “Microscopic, mesoscopic and macroscopic descriptions of complex systems,” *Probabilistic Engineering Mechanics*, vol. 26, no. 1, pp. 54–60, 2011.

[22] A. Giusti, G. C. Maffettone, D. Fiore, M. Coraggio, and M. di Bernardo, “Distributed control for geometric pattern formation of large-scale multirobot systems,” *arXiv preprint arXiv:2207.14567 (submitted to* Autonomous Robots*)*, 2022.

[23] D. L. Donoho *et al.*, “High-dimensional data analysis: The curses and blessings of dimensionality,” *AMS math challenges lecture*, vol. 1, no. 2000, p. 32, 2000.

[24] H. Ye and G. Sugihara, “Information leverage in interconnected ecosystems: Overcoming the curse of dimensionality,” *Science*, vol. 353, no. 6302, pp. 922–925, 2016.

[25] X. Wang and H. Su, “Pinning control of complex networked systems: A decade after and beyond,” *Annual Reviews in Control*, vol. 38, no. 1, pp. 103–111, 2014.

[26] D. Nikitin, C. Canudas de Wit, and P. Frasca, “A continuation method for large-scale modeling and control: from ODEs to PDE, a round trip,” *IEEE Transactions on Automatic Control*, vol. 67, no. 10, pp. 5118–5133, 2022.

[27] M. Kardar, *Statistical physics of fields*. Cambridge University Press, 2007.

[28] ——, *Statistical physics of particles*. Cambridge University Press, 2007.

[29] G. C. Maffettone, A. Boldini, M. Di Bernardo, and M. Porfiri, “Continuification control of large-scale multiagent systems in a ring,” *IEEE Control Systems Letters*, vol. 7, pp. 841–846, 2023.

[30] G. C. Maffettone, M. Porfiri, and M. Di Bernardo, “Continuification control of large-scale multiagent systems under limited sensing and structural perturbations,” *IEEE Control Systems Letters*, vol. 7, pp. 2425–2430, 2023.

[31] G. C. Maffettone, L. Liguori, E. Palermo, M. di Bernardo, and M. Porfiri, “Mixed reality environment and high-dimensional continuification control for

swarm robotics," *IEEE Transactions on Control Systems Technology (early access)*, 2024.

[32] G. C. Maffettone, M. di Bernardo, and M. Porfiri, "High-dimensional continuification control of large-scale multi-agent systems under limited sensing and perturbations," *arXiv preprint arXiv:2403.17191 (accepted for pubblication in the proceedings of the 63rd IEEE Conference of Decision and Control – Milan, December 2024)*, 2024.

[33] G. C. Maffettone, A. Boldini, M. Porfiri, and M. di Bernardo, "Leader-follower density control of spatial dynamics in large-scale multi-agent systems," *arXiv preprint arXiv:2406.01804*, 2024.

[34] S. Axler, *Measure, integration & real analysis*. Springer Nature, 2020.

[35] M. C. Jeruchim, P. Balaban, and K. S. Shanmugan, *Simulation of communication systems: modeling, methodology and techniques*. Springer Science & Business Media, 2006.

[36] L. C. Evans, *Partial differential equations*. American Mathematical Society, 2022, vol. 19.

[37] J. Heinonen, *Lectures on analysis on metric spaces*. Springer Science & Business Media, 2001.

[38] L. E. Payne and H. F. Weinberger, "An optimal Poincaré inequality for convex domains," *Archive for Rational Mechanics and Analysis*, vol. 5, no. 1, pp. 286–292, 1960.

[39] M. Bebendorf, "A note on the Poincaré inequality for convex domains," *Zeitschrift für Analysis und ihre Anwendungen*, vol. 22, no. 4, pp. 751–756, 2003.

[40] L. Gasinski and N. S. Papageorgiou, *Nonlinear Analysis*. Chapman & Hall/CRC, Boca Raton, FL, 2006.

[41] H. K. Khalil, *Nonlinear systems*. Patience Hall, 2002.

[42] D. J. Griffiths, *Introduction to electrodynamics*. Cambridge University Press, 2023.

[43] M. Rubenstein, A. Cornejo, and R. Nagpal, "Programmable self-assembly in a thousand-robot swarm," *Science*, vol. 345, no. 6198, pp. 795–799, 2014.

[44] G. Gardi, S. Ceron, W. Wang, K. Petersen, and M. Sitti, “Microrobot collectives with reconfigurable morphologies, behaviors, and functions,” *Nature Communications*, vol. 13, no. 1, pp. 1–14, 2022.

[45] A. Guarino, D. Fiore, D. Salzano, and M. di Bernardo, “Balancing cell populations endowed with a synthetic toggle switch via adaptive pulsatile feedback control,” *ACS Synthetic Biology*, vol. 9, no. 4, pp. 793–803, 2020.

[46] D. K. Agrawal, R. Marshall, V. Noireaux, and E. D. Sontag, “In vitro implementation of robust gene regulation in a synthetic biomolecular integral controller,” *Nature Communications*, vol. 10, no. 1, pp. 1–12, 2019.

[47] S. Shahal, A. Wurzberg, I. Sibony, H. Duadi, E. Shniderman, D. Weymouth, N. Davidson, and M. Fridman, “Synchronization of complex human networks,” *Nature Communications*, vol. 11, no. 1, pp. 1–10, 2020.

[48] J. Zhang, R. Vazquez, J. Qi, and M. Krstic, “Multi-agent deployment in 3D via reaction–diffusion system with radially-varying reaction,” *Automatica*, vol. 161, p. 111491, 2024.

[49] M. Rubenstein, C. Ahler, and R. Nagpal, “Kilobot: A low cost scalable robot system for collective behaviors,” in *2012 IEEE international conference on robotics and automation*. IEEE, 2012, pp. 3293–3298.

[50] P. Chadwick, *Continuum mechanics: concise theory and problems*. Courier Corporation, 2012.

[51] D. Nikitin, C. Canudas-de Wit, P. Frasca, and U. Ebels, “Synchronization of spin-torque oscillators via continuation method,” *IEEE Transactions on Automatic Control*, 2023.

[52] D. Nikitin, C. Canudas-de Wit, and P. Frasca, “Boundary control for stabilization of large-scale networks through the continuation method,” in *60th IEEE Conference on Decision and Control (CDC)*. IEEE, 2021, pp. 4792–4797.

[53] A. J. Bernoff and C. M. Topaz, “A primer of swarm equilibria,” *SIAM Journal on Applied Dynamical Systems*, vol. 10, no. 1, pp. 212–250, 2011.

[54] M. Bodnar and J. J. L. Velazquez, “Derivation of macroscopic equations for individual cell-based models: a formal approach,” *Mathematical Methods in the Applied Sciences*, vol. 28, no. 15, pp. 1757–1779, 2005.

[55] Y. Chen, “Density control of interacting agent systems,” *IEEE Transactions on Automatic Control*, vol. 69, no. 1, pp. 246–260, 2023.

[56] R. W. Brockett, “Optimal control of the liouville equation,” *AMS IP Studies in Advanced Mathematics*, vol. 39, p. 23, 2007.

[57] M. Fornasier, B. Piccoli, and F. Rossi, “Mean-field sparse optimal control,” *Philosophical Transactions of the Royal Society A: Mathematical, Physical and Engineering Sciences*, vol. 372, no. 2028, p. 20130400, 2014.

[58] K. Elamvazhuthi and S. Berman, “Mean-field models in swarm robotics: A survey,” *Bioinspiration and Biomimetics*, vol. 15, no. 1, p. ab49a4, 2020.

[59] J. A. Carrillo, Y. P. Choi, and M. Hauray, “The derivation of swarming models: Mean-field limit and Wasserstein distances,” *CISM International Centre for Mechanical Sciences, Courses and Lectures*, vol. 553, pp. 1–46, 2014.

[60] G. Ascione, D. Castorina, and F. Solombrino, “Mean-field sparse optimal control of systems with additive white noise,” *SIAM Journal on Mathematical Analysis*, vol. 55, no. 6, pp. 6965–6990, 2023.

[61] G. Albi, M. Fornasier, and D. Kalise, “A boltzmann approach to mean-field sparse feedback control,” *IFAC-PapersOnLine*, vol. 50, no. 1, pp. 2898–2903, 2017.

[62] M. Fornasier and F. Solombrino, “Mean-Field Optimal Control,” *ESAIM - Control, Optimisation and Calculus of Variations*, vol. 20, no. 4, pp. 1123–1152, 2014.

[63] C. M. Topaz, A. J. Bernoff, S. Logan, and W. Toolson, “A model for rolling swarms of locusts,” *The European Physical Journal Special Topics*, vol. 157, no. 1, pp. 93–109, 2008.

[64] A. J. Leverentz, C. M. Topaz, and A. J. Bernoff, “Asymptotic dynamics of attractive-repulsive swarms,” *SIAM Journal on Applied Dynamical Systems*, vol. 8, no. 3, pp. 880–908, 2009.

[65] C. M. Topaz, A. L. Bertozzi, and M. A. Lewis, “A nonlocal continuum model for biological aggregation,” *Bulletin of Mathematical Biology*, vol. 68, no. 7, pp. 1601–1623, 2006.

[66] S. Gao and P. E. Caines, “Graphon control of large-scale networks of linear systems,” *IEEE Transactions on Automatic Control*, vol. 65, no. 10, pp. 4090–4105, 2019.

[67] S. Gao, P. E. Caines, and M. Huang, “LQG graphon mean field games: Analysis via graphon invariant subspaces,” *IEEE Transactions on Automatic Control*, 2023.

[68] C. Kuehn and S. Throm, “Power network dynamics on graphons,” *SIAM Journal on Applied Mathematics*, vol. 79, no. 4, pp. 1271–1292, 2019.

[69] F. A. Rodrigues, T. K. D. Peron, P. Ji, and J. Kurths, “The kuramoto model in complex networks,” *Physics Reports*, vol. 610, pp. 1–98, 2016.

[70] R. Vizuete, P. Frasca, and F. Garin, “Graphon-based sensitivity analysis of sis epidemics,” *IEEE Control Systems Letters*, vol. 4, no. 3, pp. 542–547, 2020.

[71] G. Ferrari-Trecate, A. Buffa, and M. Gati, *Analysis of coordination in multi-agent systems through partial difference equations. Part I: The Laplacian control*. IFAC, 2005, vol. 16, no. 1.

[72] ——, “Analysis of coordination in multi-agent systems through partial difference equations. Part II: Nonlinear control,” *IFAC Proceedings Volumes (IFAC-PapersOnline)*, vol. 16, no. 6, pp. 209–214, 2005.

[73] ——, “Analysis of coordination in multi-agent systems through partial difference equations,” *IEEE Transactions on Automatic Control*, vol. 51, no. 6, pp. 1058–1063, 2006.

[74] R. Stephany and C. Earls, “Pde-read: Human-readable partial differential equation discovery using deep learning,” *Neural Networks*, vol. 154, pp. 360–382, 2022.

[75] S. H. Rudy, S. L. Brunton, J. L. Proctor, and J. N. Kutz, “Data-driven discovery of partial differential equations,” *Science advances*, vol. 3, no. 4, p. e1602614, 2017.

[76] E. Galaris, G. Fabiani, I. Gallos, I. Kevrekidis, and C. Siettos, “Numerical bifurcation analysis of PDEs from lattice boltzmann model simulations: a parsimonious machine learning approach,” *Journal of Scientific Computing*, vol. 92, no. 2, pp. 1–30, 2022.

[77] D. G. Patsatzis, L. Russo, I. G. Kevrekidis, and C. Siettos, “Data-driven control of agent-based models: An equation/variable-free machine learning approach,” *Journal of Computational Physics*, vol. 478, p. 111953, 2023.

[78] X. Zhang, W. Mao, S. Mowlavi, M. Benosman, and T. Başar, “Controlgym: Large-scale control environments for benchmarking reinforcement learning algorithms,”

in *6th Annual Learning for Dynamics & Control Conference*. PMLR, 2024, pp. 181–196.

[79] L. Bhan, Y. Bian, M. Krstic, and Y. Shi, “Pde control gym: A benchmark for data-driven boundary control of partial differential equations,” *arXiv preprint arXiv:2405.11401*, 2024.

[80] J. Qi, R. Vazquez, and M. Krstic, “Multi-agent deployment in 3-d via pde control,” *IEEE Transactions on Automatic Control*, vol. 60, no. 4, pp. 891–906, 2014.

[81] ——, “Multi-Agent Deployment in 3-D via PDE Control,” *IEEE Transactions on Automatic Control*, vol. 60, no. 4, pp. 891–906, 2015.

[82] M. Fornasier and F. Solombrino, “Mean-Field Optimal Control,” *ESAIM - Control, Optimisation and Calculus of Variations*, vol. 20, no. 4, pp. 1123–1152, 2014.

[83] A. Borzì and L. Grüne, “Towards a solution of mean-field control problems using model predictive control,” *IFAC-PapersOnLine*, vol. 53, no. 2, pp. 4973–4978, 2020.

[84] M. Herty and M. Zanella, “Performance bounds for the mean-field limit of constrained dynamics,” *Discrete and Continuous Dynamical Systems*, vol. 37, no. 4, pp. 2023–2043, 2016.

[85] G. Albi and L. Pareschi, “Modeling of self-organized systems interacting with a few individuals: from microscopic to macroscopic dynamics,” *Applied Mathematics Letters*, vol. 26, no. 4, pp. 397–401, 2013.

[86] G. Albi, E. Cristiani, L. Pareschi, and D. Peri, “Mathematical Models and Methods for Crowd Dynamics Control,” *Modeling and Simulation in Science, Engineering and Technology*, pp. 159–197, 2020.

[87] X. Gong, B. Piccoli, and G. Visconti, “Mean-field of optimal control problems for hybrid model of multilane traffic,” *IEEE Control Systems Letters*, vol. 5, no. 6, pp. 1964–1969, 2020.

[88] C. Lattanzio, A. Maurizi, and B. Piccoli, “Moving bottlenecks in car traffic flow: a pde-ode coupled model,” *SIAM Journal on Mathematical Analysis*, vol. 43, no. 1, pp. 50–67, 2011.

[89] G. Piacentini, P. Goatin, and A. Ferrara, “Traffic control via moving bottleneck of coordinated vehicles,” *IFAC-PapersOnLine*, vol. 51, no. 9, pp. 13–18, 2018.

[90] W. Brockett, “Minimum attention control,” in *Proceedings of the 36th IEEE Conference on Decision and Control*, vol. 3. IEEE, 1997, pp. 2628–2632.

[91] F. Alabau-Boussouira, R. Brockett, O. Glass, J. Le Rousseau, E. Zuazua, and R. Brockett, “Notes on the control of the liouville equation,” *Control of Partial Differential Equations: Cetraro, Italy 2010, Editors: Piermarco Cannarsa, Jean-Michel Coron*, pp. 101–129, 2012.

[92] J. Bartsch, A. Borzì, F. Fanelli, and S. Roy, “A theoretical investigation of brockett’s ensemble optimal control problems,” *Calculus of Variations and Partial Differential Equations*, vol. 58, pp. 1–34, 2019.

[93] Y. Chen, T. T. Georgiou, and M. Pavon, “Optimal transport in systems and control,” *Annual Review of Control, Robotics, and Autonomous Systems*, vol. 4, pp. 89–113, 2021.

[94] É. Garrabé and G. Russo, “Probabilistic design of optimal sequential decision-making algorithms in learning and control,” *Annual Reviews in Control*, vol. 54, pp. 81–102, 2022.

[95] S. Gao and P. E. Caines, “Graphon Control of Large-Scale Networks of Linear Systems,” *IEEE Transactions on Automatic Control*, vol. 65, no. 10, pp. 4090–4105, 2020.

[96] A. Dunyak and P. E. Caines, “Linear stochastic graphon systems with q-space noise,” in *2022 IEEE 61st Conference on Decision and Control (CDC)*. IEEE, 2022, pp. 3926–3932.

[97] R. Foguen-Tchuendom, S. Gao, P. E. Caines, and M. Huang, “Infinite horizon lqg graphon mean field games: Explicit nash values and local minima,” *Systems & Control Letters*, vol. 187, p. 105780, 2024.

[98] A. Boldini, M. Civitella, and M. Porfiri, “Stigmergy: from mathematical modeling to control,” *Royal Society Open Science*, vol. 1, 2024.

[99] D. Glasscock, “What is... a graphon,” *Notices of the AMS*, vol. 62, no. 1, pp. 46–48, 2015.

[100] L. Lovász, *Large networks and graph limits*. American Mathematical Soc., 2012, vol. 60.

[101] P. Frasca, F. Garin, and R. Prisant, “Opinion dynamics on signed graphs and graphons: Beyond the piece-wise constant case,” *accepted for the proceedings of the 63rd Conference on Decicion and Control, arXiv preprint arXiv:2404.08372*, 2024.

[102] C. Kuehn, “Network dynamics on graphops,” *New Journal of Physics*, vol. 22, no. 5, p. 053030, 2020.

[103] M. A. Gkogkas, B. Jüttner, C. Kuehn, and E. A. Martens, “Graphop mean-field limits and synchronization for the stochastic kuramoto model,” *Chaos: An Interdisciplinary Journal of Nonlinear Science*, vol. 32, no. 11, 2022.

[104] A. Bensoussan and J.-L. Menaldi, “Difference equations on weighted graphs,” *Journal of Convex Analysis*, vol. 12, no. 1, pp. 13–44, 2005.

[105] F. P. Kemeth, T. Bertalan, T. Thiem, F. Dietrich, S. J. Moon, C. R. Laing, and I. G. Kevrekidis, “Learning emergent partial differential equations in a learned emergent space,” *Nature communications*, vol. 13, no. 1, p. 3318, 2022.

[106] M. Krstic and A. Smyshlyaev, *Boundary control of PDEs: A course on backstepping designs*. SIAM, 2008.

[107] M. Krstic, P. V. Kokotovic, and I. Kanellakopoulos, *Nonlinear and adaptive control design*. John Wiley & Sons, Inc., 1995.

[108] M. Ji, G. Ferrari-Trecate, M. Egerstedt, and A. Buffa, “Containment control in mobile networks,” *IEEE Transactions on Automatic Control*, vol. 53, no. 8, pp. 1972–1975, 2008.

[109] S. Siri, C. Pasquale, S. Sacone, and A. Ferrara, “Freeway traffic control: A survey,” *Automatica*, vol. 130, p. 109655, 2021.

[110] K. H. Petersen, N. Napp, R. Stuart-Smith, D. Rus, and M. Kovac, “A review of collective robotic construction,” *Science Robotics*, vol. 4, no. 28, p. eaau8479, 2019.

[111] D. Del Vecchio, Y. Qian, R. M. Murray, and E. D. Sontag, “Future systems and control research in synthetic biology,” *Annual Reviews in Control*, vol. 45, pp. 5–17, 2018.

[112] M. Brambilla, E. Ferrante, M. Birattari, and M. Dorigo, "Swarm robotics: A review from the swarm engineering perspective," *Swarm Intelligence*, vol. 7, no. 1, pp. 1–41, 2013.

[113] E. M. H. Zahugi, M. M. Shanta, and T. Prasad, "Oil spill cleaning up using swarm of robots," in *Advances in Computing and Information Technology: Proceedings of the Second International Conference on Advances in Computing and Information Technology (ACITY) July 13-15, 2012, Chennai, India-Volume 3*. Springer, 2013, pp. 215–224.

[114] J. Cruz, "Leader-follower strategies for multilevel systems," *IEEE Transactions on Automatic Control*, vol. 23, no. 2, pp. 244–255, 1978.

[115] M. Lombardi, W. H. Warren, and M. di Bernardo, "Nonverbal leadership emergence in walking groups," *Scientific Reports*, vol. 10, no. 1, p. 18948, 2020.

[116] A. J. King, D. D. Johnson, and M. Van Vugt, "The origins and evolution of leadership," *Current Biology*, vol. 19, no. 19, pp. R911–R916, 2009.

[117] A. Zienkiewicz, D. A. Barton, M. Porfiri, and M. Di Bernardo, "Leadership emergence in a data-driven model of zebrafish shoals with speed modulation," *The European Physical Journal Special Topics*, vol. 224, pp. 3343–3360, 2015.

[118] J. Hindes, V. Edwards, M. A. Hsieh, and I. B. Schwartz, "Critical transition for colliding swarms," *Physical Review E*, vol. 103, no. 6, p. 062602, 2021.

[119] D. Armbruster, S. Martin, and A. Thatcher, "Elastic and inelastic collisions of swarms," *Physica D: Nonlinear Phenomena*, vol. 344, pp. 45–57, 2017.

[120] D. Salzano, B. Shannon, C. Grierson, L. Marucci, N. J. Savery, and M. di Bernardo, "In-vivo distributed multicellular control of gene expression in microbial consortia," *bioRxiv*, pp. 2023–11, 2023.

[121] V. Martinelli, D. Salzano, D. Fiore, and M. di Bernardo, "Multicellular PI control for gene regulation in microbial consortia," *IEEE Control Systems Letters*, vol. 6, pp. 3373–3378, 2022.

[122] D. Ko and E. Zuazua, "Asymptotic behavior and control of a "guidance by repulsion" model," *Mathematical Models and Methods in Applied Sciences*, vol. 30, no. 04, pp. 765–804, 2020.

[123] E. Sebastián, E. Montijano, and C. Sagüés, "Adaptive multirobot implicit control of heterogeneous herds," *IEEE Transactions on Robotics*, vol. 38, no. 6, pp. 3622–3635, 2022.

[124] F. Auletta, D. Fiore, M. J. Richardson, and M. di Bernardo, "Herding stochastic autonomous agents via local control rules and online target selection strategies," *Autonomous Robots*, vol. 46, no. 3, pp. 469–481, 2022.

[125] C. Sinigaglia, A. Manzoni, and F. Braghin, "Density control of large-scale particles swarm through pde-constrained optimization," *IEEE Transactions on Robotics*, vol. 38, no. 6, pp. 3530–3549, 2022.

[126] S. Biswal, K. Elamvazhuthi, and S. Berman, "Decentralized control of multiagent systems using local density feedback," *IEEE Transactions on Automatic Control*, vol. 67, no. 8, pp. 3920–3932, 2021.

[127] C. A. Yates, R. Erban, C. Escudero, I. D. Couzin, J. Buhl, I. G. Kevrekidis, P. K. Maini, and D. J. Sumpter, "Inherent noise can facilitate coherence in collective swarm motion," *PNAS*, vol. 106, no. 14, pp. 5464–5469, 2009.

[128] M. Fornasier and F. Solombrino, "Mean-field optimal control," *ESAIM: Control, Optimisation and Calculus of Variations*, vol. 20, no. 4, pp. 1123–1152, 2014.

[129] M. Bongini and G. Buttazzo, "Optimal control problems in transport dynamics," *Mathematical Models and Methods in Applied Sciences*, vol. 27, no. 03, pp. 427–451, 2017.

[130] S. Almi, M. Morandotti, and F. Solombrino, "Optimal control problems in transport dynamics with additive noise," *Journal of Differential Equations*, vol. 373, pp. 1–47, 2023.

[131] J. Wei, E. Fridman, and K. H. Johansson, "A PDE approach to deployment of mobile agents under leader relative position measurements," *Automatica*, vol. 106, pp. 47–53, 2019.

[132] P. Frihauf and M. Krstic, "Leader-enabled deployment onto planar curves: A PDE-based approach," *IEEE Transactions on Automatic Control*, vol. 56, no. 8, pp. 1791–1806, 2010.

[133] S. Zhang, X. Lei, M. Duan, X. Peng, and J. Pan, "A distributed outmost push approach for multi-robot herding," *IEEE Transactions on Robotics*, 2024.

[134] L. Aguilar, Y. Orlov, and A. Pisano, "Leader-follower synchronization and ISS analysis for a network of boundary-controlled wave PDEs," *IEEE Control Systems Letters*, vol. 5, no. 2, pp. 683–688, 2020.

[135] Q. Fu, P. Yu, G. Xu, and J. Wu, "Containment control for partial differential multi-agent systems," *Physica A: Statistical Mechanics and its Applications*, vol. 529, p. 121549, 2019.

[136] M. Dorigo, G. Theraulaz, and V. Trianni, "Swarm robotics: Past, present, and future [point of view]," *Proceedings of the IEEE*, vol. 109, no. 7, pp. 1152–1165, 2021.

[137] I. Slavkov, D. Carrillo-Zapata, N. Carranza, X. Diego, F. Jansson, J. Kaandorp, S. Hauert, and J. Sharpe, "Morphogenesis in robot swarms," *Science Robotics*, vol. 3, no. 25, p. eaau9178, 2018.

[138] G. Caprari and R. Siegwart, "Mobile micro-robots ready to use: Alice," in *2005 IEEE/RSJ International Conference on Intelligent Robots and Systems*. IEEE, 2005, pp. 3295–3300.

[139] F. Mondada, M. Bonani, X. Raemy, J. Pugh, C. Cianci, A. Klaptocz, S. Magnenat, J.-C. Zufferey, D. Floreano, and A. Martinoli, "The e-puck, a robot designed for education in engineering," in *Proceedings of the 9th conference on autonomous robot systems and competitions*, vol. 1. IPCB: Instituto Politécnico de Castelo Branco, 2009, pp. 59–65.

[140] M. Rubenstein, A. Cabrera, J. Werfel, G. Habibi, J. McLurkin, and R. Nagpal, "Collective transport of complex objects by simple robots: theory and experiments," in *Proceedings of the 2013 international conference on Autonomous agents and multi-agent systems*, 2013, pp. 47–54.

[141] A. Boldini, X. Ma, J.-R. Rizzo, and M. Porfiri, "A virtual reality interface to test wearable electronic travel aids for the visually impaired," in *Nano-, Bio-, Info-Tech Sensors and Wearable Systems*, vol. 11590. SPIE, 2021, pp. 50–56.

[142] F. S. Ricci, A. Boldini, X. Ma, M. Beheshti, D. R. Geruschat, W. H. Seiple, J.-R. Rizzo, and M. Porfiri, "Virtual reality as a means to explore assistive technologies for the visually impaired," *PLOS Digital Health*, vol. 2, no. 6, p. e0000275, 2023.

[143] H. Naik, R. Bastien, N. Navab, and I. D. Couzin, “Animals in virtual environments,” *IEEE Transactions on Visualization and Computer Graphics*, vol. 26, no. 5, pp. 2073–2083, 2020.

[144] J. R. Stowers, M. Hofbauer, R. Bastien, J. Griessner, P. Higgins, S. Farooqui, R. M. Fischer, K. Nowikovsky, W. Haubensak, I. D. Couzin *et al.*, “Virtual reality for freely moving animals,” *Nature methods*, vol. 14, no. 10, pp. 995–1002, 2017.

[145] M. Karakaya, S. Macrì, and M. Porfiri, “Behavioral teleporting of individual ethograms onto inanimate robots: experiments on social interactions in live zebrafish,” *iScience*, vol. 23, no. 8, 2020.

[146] G. Polverino, V. R. Soman, M. Karakaya, C. Gasparini, J. P. Evans, and M. Porfiri, “Ecology of fear in highly invasive fish revealed by robots,” *iScience*, vol. 25, no. 1, 2022.

[147] J. W. Durham, R. Carli, P. Frasca, and F. Bullo, “Discrete partitioning and coverage control for gossiping robots,” *IEEE Transactions on Robotics*, vol. 28, no. 2, pp. 364–378, 2011.

[148] F. J. Mañas-Álvarez, M. Guinaldo, R. Dormido, and S. Dormido-Canto, “Scalability of cyber-physical systems with real and virtual robots in ros 2,” *Sensors*, vol. 23, no. 13, p. 6073, 2023.

[149] D. Karunarathna, N. Jaliyagoda, G. Jayalath, J. Alawatugoda, R. Ragel, and I. Nawinne, “Mixed-reality based multi-agent robotics framework for artificial swarm intelligence experiments,” *IEEE Access*, 2023.

[150] A. Reina, A. J. Cope, E. Nikolaidis, J. A. Marshall, and C. Sabo, “Ark: Augmented reality for kilobots,” *IEEE Robotics and Automation letters*, vol. 2, no. 3, pp. 1755–1761, 2017.

[151] L. Feola, A. Reina, M. S. Talamali, and V. Trianni, “Multi-swarm interaction through augmented reality for kilobots,” *IEEE Robotics and Automation Letters*, 2023.

[152] D. Pickem, P. Glotfelter, L. Wang, M. Mote, A. Ames, E. Feron, and M. Egerstedt, “The robotarium: A remotely accessible swarm robotics research testbed,” in *2017 IEEE International Conference on Robotics and Automation (ICRA)*. IEEE, 2017, pp. 1699–1706.

[153] M. di Bernardo, “Controlling collective behavior in complex systems,” in *Encyclopedia of Systems and Control*, J. Baillieul and T. Samad, Eds. Springer London, 2020.

[154] K. Elamvazhuthi, Z. Kakish, A. Shirsat, and S. Berman, “Controllability and Stabilization for Herding a Robotic Swarm Using a Leader: A Mean-Field Approach,” *IEEE Transactions on Robotics*, vol. 37, no. 2, pp. 418–432, 2021.

[155] A. Borzì and L. Grüne, “Towards a solution of mean-field control problems using model predictive control,” *Proc. 21st IFAC World Congress, Berlin, Germany*, vol. 53, no. 2, pp. 4973–4978, July 2020.

[156] A. Kolpas, J. Moehlis, and I. G. Kevrekidis, “Coarse-grained analysis of stochasticity-induced switching between collective motion states,” *Proceedings of the National Academy of Sciences*, vol. 104, no. 14, pp. 5931–5935, 2007.

[157] H. Gu, X. Guo, X. Wei, and R. Xu, “Mean-field controls with Q-learning for cooperative MARL: convergence and complexity analysis,” *SIAM Journal on Mathematics of Data Science*, vol. 3, no. 4, pp. 1168–1196, 2021.

[158] W. U. Mondal, M. Agarwal, V. Aggarwal, and S. V. Ukkusuri, “On the approximation of cooperative heterogeneous multi-agent reinforcement learning (MARL) using mean field control (MFC),” *Journal of Machine Learning Research*, vol. 23, no. 129, pp. 1–46, 2022.

[159] S. Lee, M. Kooshkbaghi, K. Spiliotis, C. I. Siettos, and I. G. Kevrekidis, “Coarse-scale PDEs from fine-scale observations via machine learning,” *Chaos: An Interdisciplinary Journal of Nonlinear Science*, vol. 30, no. 1, p. 013141, 2020.

[160] D. G. Patsatzis, L. Russo, I. G. Kevrekidis, and C. Siettos, “Data-driven control of agent-based models: an equation/variable-free machine learning approach,” *arXiv preprint arXiv:2207.05779*, 2022.

[161] I. Karafyllis and M. Papageorgiou, “Feedback control of scalar conservation laws with application to density control in freeways by means of variable speed limits,” *Automatica*, vol. 105, pp. 228–236, 2019.

[162] T. Liard, R. Stern, and M. L. D. Monache, “A pde-ode model for traffic control with autonomous vehicles,” *Networks and Heterogeneous Media*, vol. 18, no. 3, pp. 1190–1206, 2023.

[163] A. K. Zienkiewicz, F. Ladu, D. A. Barton, M. Porfiri, and M. D. Bernardo, “Data-driven modelling of social forces and collective behaviour in zebrafish,” *Journal of Theoretical Biology*, vol. 443, pp. 39–51, 2018.

[164] N. Abaid and M. Porfiri, “Fish in a ring: Spatio-temporal pattern formation in one-dimensional animal groups,” *Journal of the Royal Society Interface*, vol. 7, no. 51, pp. 1441–1453, 2010.

[165] P. De Lellis, E. Cadolini, A. Croce, Y. Yang, M. Di Bernardo, and M. Porfiri, “Model-based feedback control of live zebrafish behavior via interaction with a robotic replica,” *IEEE Transactions on Robotics*, vol. 36, no. 1, pp. 28–41, 2020.

[166] T. Viscek, A. Czirȍk, E. Ben-Jacob, I. Cohen, and O. Shochet, “Novel Type of Phase Transition in a System of Self-Driven Particles,” *Physical Review Letters*, vol. 75, no. 6, pp. 1226–1229, 1995.

[167] M. R. D’Orsogna, Y. L. Chuang, A. L. Bertozzi, and L. S. Chayes, “Self-propelled particles with soft-core interactions: Patterns, stability, and collapse,” *Physical Review Letters*, vol. 96, no. 10, 2006.

[168] B. W. Silverman, *Density estimation for statistics and data analysis*. Routledge, 2018.

[169] S. Kullback and R. A. Leibler, “On information and sufficiency,” *The Annals of Mathematical Statistics*, vol. 22, no. 1, pp. 79–86, 1951.

[170] D. Gagliardi and G. Russo, “On a probabilistic approach to synthesize control policies from example datasets,” *Automatica*, vol. 137, p. 110121, 2022.

[171] K. V. Mardia, P. E. Jupp, and K. Mardia, *Directional statistics*. Wiley Online Library, 2000, vol. 2.

[172] G. Freudenthaler and T. Meurer, “Pde-based multi-agent formation control using flatness and backstepping: Analysis, design and robot experiments,” *Automatica*, vol. 115, p. 108897, 2020.

[173] A. Rubio Denniss, T. E. Gorochowski, and S. Hauert, “An open platform for high-resolution light-based control of microscopic collectives,” *Advanced Intelligent Systems*, p. 2200009, 2022.

[174] T. Menara, G. Baggio, D. Bassett, and F. Pasqualetti, “Functional control of oscillator networks,” *Nature Communications*, vol. 13, no. 1, p. 4721, 2022.

[175] R. Noori, D. Park, J. D. Griffiths, S. Bells, P. W. Frankland, D. Mabbott, and J. Lefebvre, “Activity-dependent myelination: A glial mechanism of oscillatory self-organization in large-scale brain networks,” *Proceedings of the National Academy of Sciences*, vol. 117, no. 24, pp. 13 227–13 237, 2020.

[176] N. Mills, “Incompressible mixtures of Newtonian fluids,” *International Journal of Engineering Science*, vol. 4, no. 2, pp. 97–112, 1966.

[177] Z. Yuan, T. Zheng, M. Nayyar, A. R. Wagner, H. Lin, and M. Zhu, “Multi-robot-assisted human crowd control for emergency evacuation: A stabilization approach,” in *2023 American Control Conference (ACC)*. IEEE, 2023, pp. 4051–4056.

[178] H. L. Royden and P. Fitzpatrick, *Real analysis*. Macmillan New York, 1968, vol. 2.

[179] G. M. Wing, *A primer on integral equations of the first kind: the problem of deconvolution and unfolding*. SIAM, 1991.

[180] A. Bemporad, “Reference governor for constrained nonlinear systems,” *IEEE Transactions on Automatic Control*, vol. 43, no. 3, pp. 415–419, 1998.

[181] G. Allaire, “Homogenization and two-scale convergence,” *SIAM Journal on Mathematical Analysis*, vol. 23, no. 6, pp. 1482–1518, 1992.

[182] E. Sánchez-Palencia, “Non-homogeneous media and vibration theory,” *Lecture Note in Physics, Springer-Verlag*, vol. 320, pp. 57–65, 1980.

[183] A. J. Izenman, “Review papers: Recent developments in nonparametric density estimation,” *Journal of the american statistical association*, vol. 86, no. 413, pp. 205–224, 1991.

[184] B. McKelvey, “Microstrategy from macroleadership: Distributed intelligence via new science,” *Mobilizing the self-renewing organization*, p. 18, 2003.

[185] R. Marion and M. Uhl-Bien, “Leadership in complex organizations,” *The leadership quarterly*, vol. 12, no. 4, pp. 389–418, 2001.

[186] B. Pettit, Z. Akos, T. Vicsek, and D. Biro, “Speed determines leadership and leadership determines learning during pigeon flocking,” *Current Biology*, vol. 25, no. 23, pp. 3132–3137, 2015.

[187] D. S. Wilson and E. Sober, “Reviving the superorganism,” *Journal of theoretical Biology*, vol. 136, no. 3, pp. 337–356, 1989.

[188] S. Marras and P. Domenici, “Schooling fish under attack are not all equal: some lead, others follow,” *PLoS One*, vol. 8, no. 6, p. e65784, 2013.

[189] P. Buston, “Size and growth modification in clownfish,” *Nature*, vol. 424, no. 6945, pp. 145–146, 2003.

[190] S. Butail, V. Mwaffo, and M. Porfiri, “Model-free information-theoretic approach to infer leadership in pairs of zebrafish,” *Physical Review E*, vol. 93, no. 4, p. 042411, 2016.

[191] I. D. Couzin, J. Krause, N. R. Franks, and S. A. Levin, “Effective leadership and decision-making in animal groups on the move,” *Nature*, vol. 433, no. 7025, pp. 513–516, 2005.

[192] C. M. Lindeyer and S. M. Reader, “Social learning of escape routes in zebrafish and the stability of behavioural traditions,” *Animal Behaviour*, vol. 79, no. 4, pp. 827–834, 2010.

[193] M. D. Binder, N. Hirokawa, and U. Windhorst, Eds., *Behavioral Plasticity*. Berlin, Heidelberg: Springer Berlin Heidelberg, 2009.

[194] T. D. Price, A. Qvarnström, and D. E. Irwin, “The role of phenotypic plasticity in driving genetic evolution,” *Proceedings of the Royal Society of London. Series B: Biological Sciences*, vol. 270, no. 1523, pp. 1433–1440, 2003.

[195] Y. Q. Chen and Z. Wang, “Formation control: a review and a new consideration,” in *2005 IEEE/RSJ International conference on intelligent robots and systems*. IEEE, 2005, pp. 3181–3186.

[196] S. Mkhatshwa and G. Nitschke, “The impact of morphological diversity in robot swarms,” in *Proceedings of the Genetic and Evolutionary Computation Conference*, 2023, pp. 65–74.

[197] E. R. Hunt, “Phenotypic plasticity provides a bioinspiration framework for minimal field swarm robotics,” *Frontiers in Robotics and AI*, vol. 7, p. 23, 2020.

[198] I. Karafyllis, D. Theodosis, and M. Papageorgiou, “Analysis and control of a nonlocal PDE traffic flow model,” *International Journal of Control*, vol. 95, no. 3, pp. 660–678, 2022.

[199] S. Blandin, D. Work, P. Goatin, B. Piccoli, and A. Bayen, “A general phase transition model for vehicular traffic,” *SIAM journal on Applied Mathematics*, vol. 71, no. 1, pp. 107–127, 2011.

[200] B. Siciliano, L. Sciavicco, L. Villani, and G. Oriolo, *Robotics: Modelling, Planning and Control*. Springer Publishing Company, Incorporated, 2010.

[201] H. Ando, Y. Oasa, I. Suzuki, and M. Yamashita, “Distributed memoryless point convergence algorithm for mobile robots with limited visibility,” *IEEE Transactions on Robotics and Automation*, vol. 15, no. 5, pp. 818–828, 1999.

[202] K.-K. Oh, M.-C. Park, and H.-S. Ahn, “A survey of multi-agent formation control,” *Automatica*, vol. 53, pp. 424–440, 2015.

[203] S. Wilson, P. Glotfelter, L. Wang, S. Mayya, G. Notomista, M. Mote, and M. Egerstedt, “The robotarium: Globally impactful opportunities, challenges, and lessons learned in remote-access, distributed control of multirobot systems,” *IEEE Control Systems Magazine*, vol. 40, no. 1, pp. 26–44, 2020.

[204] R. J. LeVeque, *Finite volume methods for hyperbolic problems*. Cambridge university press, 2002, vol. 31.